Phil. Trans. R. Soc. Lond. A **331**, 245–286 (1990) [245]
Printed in Great Britain

Flow past a circular cylinder in a rotating stratified fluid

By P. A. DAVIES[1], R. G. DAVIS[1] and M. R. FOSTER[2]

[1] *Department of Civil Engineering, The University, Dundee DD1 4HN, U.K.*
[2] *Department of Aeronautical and Astronautical Engineering, The Ohio State University, Columbus, Ohio* 43210-1276, *U.S.A.*

(*Communicated by F. T. Smith, F.R.S. – Received* 11 *September* 1989 – *Revised* 15 *January* 1990)

[Plates 1–18]

Experimental results are presented to show the development of the flow past a cylinder in a rotating stratified fluid. Both transient and fully developed flow states are investigated, for a range of values of Rossby number Ro and Burger number Bu and for full depth and truncated obstacles. The fully developed flows are shown to be of three main types, delineated respectively as attached eddy pairs, transitional, and vortex wakes, with the boundaries between each flow type being determined by the values of the Reynolds number, the Burger number, the aspect ratio and the ratio of the height of the obstacle to the depth of the fluid. For cases of homogeneous fluid flow, the critical Rossby and Reynolds numbers for vortex shedding are significantly lower than the values found by Boyer. The discrepancy is ascribed to aspect ratio effects and differences in the cylinder shear layer structures in the two studies. The weakening effects of density stratification upon characteristic features of rapidly rotating homogeneous flows are seen to be two-fold: firstly, the wake asymmetries associated with the unstratified flows are seen to be destroyed by the stratification, and, secondly, the retention times of starting eddies, the eddy growth times and the isolated eddy formation times are shown to no longer tune with the background rotation timescale but to scale with the advective timescale of the motion and the aspect ratio of the cylinder.

Cross-stream velocity profiles taken at several downstream stations in the wake of the cylinder are used to show a linear increase in the momentum flux coefficient with increasing Re, in the range $55 < Re < 135$.

Velocity profile measurements taken above and downstream of the truncated cylinder are presented. These show that the vertical distance over which the upper level fluid is influenced by the presence of the obstacle depends strongly upon the value of Bu, and is typically one-tenth of the obstacle height at the highest values of Bu.

Finally, flow visualization studies of the motion in the vertical shear layers for $Bu = 0$ are compared and contrasted with other similar observations, and with theoretical understandings of the flow structure. The importance of the upper boundary condition is clarified.

1. Introduction

The flow of an incompressible fluid past an upright circular cylinder is a classical problem in fluid dynamics. Since the pioneering laboratory studies of Prandtl & Tietjens (1934), a vast literature has been established on the numerous experimental and computational investigations in the field. The reader is referred to Tritton (1988) for a thorough review of the changes in

The Royal Society is collaborating with JSTOR to digitize, preserve, and extend access to *Philosophical Transactions of the Royal Society of London. Series A, Mathematical and Physical Sciences.* www.jstor.org

flow which occur at, and downstream of, the cylinder, as the sole controlling dynamical parameter (the Reynolds number) is changed, and to the detailed studies by Morkovin (1964), Mair & Maull (1971), Bearman & Graham (1980), Coutanceau & Bouard (1977*a*, *b*), Bouard & Coutanceau (1980), Gerrard (1978), Honji & Taneda (1969), Collins & Dennis (1973), Imaichi & Ohmi (1983), and Son & Hanratty (1969) for specific laboratory and numerical data regarding flow characteristics relevant to particular Reynolds number ranges.

In recent years, there has been renewed interest in the topic because of its relevance to certain meteorological and oceanic flow phenomena (Baines & Davies 1980; Wolanski *et al.* 1984; Pattiaratchi *et al.* 1986; Davies & Mofor 1990). To further investigate this relevance, it has been necessary to consider the additional, geophysically important effects of background rotation and density stratification upon the above flows. In the present paper, both of these effects are considered, for cylinders which (*a*) extend throughout, and (*b*) occupy a fraction of, the fluid depth. The plan for the paper is the following: after descriptions of the experimental facility and the physical system under consideration (§§2 and 3), laboratory data are presented to show the effects of rotation and stratification upon transient and fully developed flows. Full-cylinder cases are considered in §4, and truncated obstacles in §5. In §6, the theoretical shear layer structure on the cylinder is presented for the limiting case of homogeneous, rotating flow, and its predictions compared with flow visualization results. The exact upper boundary condition in an experimental arrangement is found to be critical in that comparison.

For the full-cylinder geometry, previous experimental studies conducted by Boyer (1970), Boyer & Davies (1982), Boyer & Kmetz (1983), Boyer *et al.* (1984*b*), and Chabert d'Hieres *et al.* (1989, 1990) with homogeneous fluids have established that rapid background rotation causes separation and vortex shedding to occur at a critical values of the Reynolds number significantly higher than those for the corresponding non-rotating cases. Furthermore, for shedding flows the presence of rotation results in the formation of an asymmetrical wake flow in which cyclonic eddies dominate their anticyclonic counterparts. Associated theoretical studies by Merkine & Solan (1979), Merkine (1980), Walker & Stewartson (1972), and Matsuura & Yamagata (1983) offer qualitative support for some of these results.

Taylor (1923), Hide & Ibbetson (1966), Heikes & Maxworthy (1982), and Boyer *et al.* (1984*a*) have studied homogeneous, rotating flows over and around truncated cylinders occupying only a fraction of the fluid depth, and have shown that for these and other isolated solid obstacles the presence of rapid background rotation is associated with strong steering of the upper level flow by the bottom topography (the Taylor column effect). Numerous analytical studies of different aspects of the Taylor column problem have been presented (see, for example, the review by Baines & Davies (1980) and the papers by Walker & Stewartson (1974), James (1980), Page (1985) and Verron & Le Provost (1987)). Studies of rotating stratified flows past solid obstacles are rare, these being confined primarily to laboratory investigations of steering attenuation above, and/or eddy generation downstream of, isolated three-dimensional obstacles (Davies 1972; Davies & Rahm 1982; Boyer *et al.* 1987), and analytical studies (Hogg 1973; Merkine & Kalnay-Rivas 1976; Foster 1989) of stratified Taylor columns. The only existing studies of rotating, stratified flow past a full cylinder are contained in the theoretical analyses of Brevdo & Merkine (1985) and Merkine (1985).

2. Physical system

The physical system under consideration is similar to that studied by Boyer *et al.* (1987) and shown in figure 1. In the cartesian coordinate system (x, y, z), a cylindrical solid obstacle of height h and diameter D interacts with a uniform, steady, horizontal flow $\boldsymbol{u} = (U_0, 0, 0)$ of a linearly stratified fluid of mean density ρ_0, and mean kinematic viscosity ν. The fluid is of depth H, and is contained within a channel of length L and width $2W$ which rotates uniformly about the vertical (z) axis with angular velocity $\boldsymbol{\Omega} = (0, 0, \Omega)$. The following set of dimensionless parameters serve to describe the flow in such a system:

$$Ro = U_0/2\Omega D, \qquad \text{the Rossby number,}$$

$$E = \nu/\Omega H^2, \qquad \text{the Ekman number,}$$

$$Bu = (N/2\Omega)^2/(h/D)^2 \qquad \text{the Burger number}$$

and the geometrical parameters h/H, H/D, L/D, and W/D.

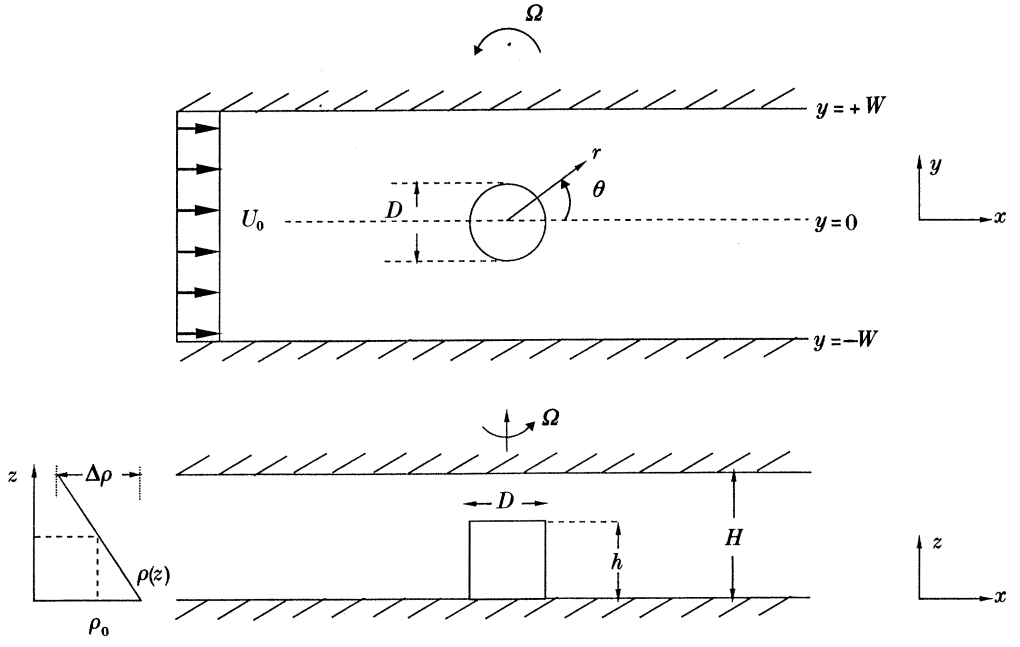

FIGURE 1. Plan and side elevation sketches of the physical system.

In the experiments to be described, E, L/D and W/D were held constant at the values 9.4×10^{-5}, 33.3, and 6.7 respectively, and, for a given cylinder, changes in the flow were caused by changes in Ro and Bu only. (Note that the quantity N is the buoyancy frequency of the stratified fluid, defined by $N^2 = g\Delta\rho/\rho_0 H$, where $\Delta\rho$ is the density difference between the top and bottom of the fluid layer, and $g = (0, 0, -g)$ is the acceleration due to gravity). Full cylinders $(h/H = 1.0)$ having aspect ratios H/D of 2.5 and 6.25, and a truncated cylinder having $h/H = 0.4$ and $h/D = 1.0$, were considered.

3. Laboratory apparatus and experimental procedure

The experiments were conducted using a rotating tow tank facility of the type originally designed and developed by Kmetz (1982) and Boyer *et al.* (1987). It consisted of a Plexiglas channel of dimensions 2.0 m × 0.4 m × 0.3 m, which could be filled by the Oster (1965) technique with a salt-stratified fluid from two large external reservoirs. Only linear density gradients were considered. Relative motion between the fluid and a Plexiglas cylinder mounted on the continuous belt at the base of the tank was generated by the translatory movement of the belt. The speed of the latter could be varied continuously by means of a small motor mounted externally to the tank; the speed of the motor and the rate at which it reached a pre-set uniform velocity from an impulsive start were controlled by computer. The minimum permissible speed at which the obstacle could be driven steadily was found to be 0.4 mm s^{-1}; the maximum value was determined by the reaction time of the cut-off switches which prevented the trolley running off the rails, and this speed was found to be approximately 7.6 cm s^{-1}. The rotation period of the table was measured continuously by an electronic timer triggered by a magnetic switch arrangement.

The working fluid was bounded above by a flat horizontal Plexiglas plate, and for the full cylinder cases a small gap was left between the lid and the top of the cylinder to allow for free movement between the two solid surfaces. A system of slip rings on the rotating table (i) allowed the belt speed and the photographic sequencing to be controlled from a computer in the laboratory frame of reference, and (ii) permitted access to instrumentation onboard the rotating table. The reader is referred to Davis (1989) for a full mechanical description of the tow tank facility.

The vertical density gradient within the working fluid was measured when the stratified fluid had reached solid body rotation by withdrawing samples at different depths and measuring their densities with a refractometer. The fluid container was filled (i.e. stratified) when the turntable was at rest, and then spun up slowly to the required rotation rate. Solid body rotation was achieved within a period of five to six hours of the turntable being activated. The velocity of the obstacle was measured by two methods: firstly, by using sequences of plan photographs of the working section and timing the movement of the front edge of the cylinder between fiducial marks inscribed on the tank lid. In the second method, the belt drive motor was coupled to a rotary potentiometer across which a constant voltage was applied. By measuring the rate of change with time of the voltage output from the potentiometer, the speed of the belt, and hence the speed of the cylinder, could be determined. Flow patterns within the fluid were visualized by four different methods: for cases in which the fluid was stratified, small (*ca.* 1 mm diameter) polystyrene beads suspended throughout the fluid depth were illuminated with an intense, narrow (*ca.* 5 mm) beam of light from a light box source mounted on the rotating table. With this method, horizontal and vertical motions could be visualized at different levels and different transverse locations respectively, by moving the positions of the light sources. The motions of the particles were recorded photographically with several cameras mounted both above and to the side of the main channel. The suspended particle technique only works well within a limited range of density stratifications, so other methods of flow visualization were used with homogeneous and strongly stratified cases. The electrolytic dye precipitation technique (Honji *et al.* 1980; Boyer & Davies 1982) was used for the stratified cases, while, for the homogeneous fluid experiments, either the Baker (1966) thymol blue method was used or the fluid was seeded with Mearle fish scales.

For recording of the horizontal flow patterns, cameras could be mounted on a four wheel overhead trolley which was carried on two overhead rails held in position by four upright posts bolted to the main framework of the tank. The trolley was clamped to a belt which ran over pulleys coupled to one of the conveyor belt drive rollers, so that the cameras and the obstacle traversed the channel at the same speed. For some of the experiments, it was preferable to record the flow with respect to the frame of reference of the tank, rather than that of the moving obstacle. In these cases, the trolley was disconnected from the motion of the belt and the cameras recorded the flow as the obstacle passed across their field of view. Data derived from the latter and former arrangements were designated 'uncoupled' and 'coupled' frame data respectively.

4. Results: full cylinders

Experiments were conducted with two full depth cylinders having different diameters, to investigate effects upon the flow of differences in aspect ratio h/D and blockage ratio D/W. In addition, an initial set of experiments was conducted to determine whether the flow past these cylinders showed any variation with height. Observations were made at levels z/H of 0.25, 0.50 and 0.75 for various values of the non-dimensional parameters, but it was seen that for all of the rotating experiments the overall character of the flow remained two dimensional within the interior of the fluid. For this reason, all remaining full depth cylinder experiments were observed at a single level, $z/H = 0.5$.

In these and the truncated cylinder experiments to be described later (§5), flow patterns were recorded (i) during the transient stages of development following the impulsive start (but after the obstacle had achieved a constant velocity), and (ii) throughout the period in which the final, fully developed flow pattern (steady or unsteady) had been established.

4.1. *Transient flow development*

Figures 2–5, plates 1–4, show a series of four time sequences for approximately the same relatively high Burger number, but for successively higher values of the Rossby number. The development of the flow for the lowest value of *Ro* can be seen in figure 2. In frame (*a*) the obstacle has just been started impulsively into motion, and has moved a distance less than its own diameter. During this interval, the two starting eddies which have formed on either side of the obstacle are circular and symmetrical in form. As time proceeds, particle trajectories in the disturbance field around the cylinder extend further in the cross-stream direction, and the starting eddies elongate in the downstream direction. Both starting eddies appear to have the same strength. The next frames in the sequence show that as time progresses the eddies maintain their elliptical form and eventually reach a steady size and shape. They remain attached to the obstacle until the end of the traverse is reached. In the far-field wake region of the cylinder, a tail of fluid extending far downstream is dragged along by the obstacle. The fully developed flow type typified by the final frame of the sequence in figure 2 is denoted *attached eddy pairs*.

In the next time sequence (figure 3), the value of *Ro* has been increased slightly from that of figure 2. During the transient flow development phase, the starting eddies show a similar spatial development to that described previously, except that in this case the eddies show more elongation than before (see figures 2*d* and 3*d*, for example) at the same dimensionless reference time t_A^*. The principal modification to the flow resulting from the increase in the value of *Ro* is seen to be the appearance of waviness in the tail. Associated with this behaviour is the

initiation of an asymmetrical, periodic process which causes the size of one attached eddy in the pair to grow and contract in anti-phase with that of its partner. For example, note the elongation : contraction cycle of the attached anticyclones from frames (*b*) to (*e*) in figure 4. The widths of the tails in the two cases are both of the same order as the obstacle diameter. (The waviness of the tail is indicative of incipient instability in the flow, though no isolated vortices are formed in the wake.) This type of flow in which the tail in the cylinder wake is wavy, but no shedding of vortices from the cylinder is taking place (figure 3) is denoted *transitional flow*.

However, as the value of *Ro* is increased further (figure 4), the waviness becomes more pronounced and isolated eddies are formed in the fully developed wake flow (figure 4*e*). These eddies are arranged in a Karman vortex street pattern, consisting of a regular, staggered array of counter-rotating vortices in the far wake and an unsteady eddy pair pattern at the rear of the obstacle. The changes which occur in the transient phase preceding the establishment of the fully developed flow, can be followed clearly in figure 4. The starting eddy pair is seen to elongate rapidly with time and to develop asymmetry in the sizes of the component eddies (figure 4*c*, *d*). In addition, when the largest eddy of the two reaches a critical size, it is shed from the cylinder (figure 4*d*) and the other eddy grows. The alternate periodic shedding from the cylinder of vortices of opposite polarity then continues, until the fully developed flow typified by figure 4*e* is established.

As the value of the Rossby number is increased further, the shedding process is initiated at an earlier stage in the flow development and the resulting shed eddies have sizes which increase with increases in the value of the Rossby number (figure 5). For cases such as figures 4 and 5, the fully developed flow types are known as *isolated eddy* or *vortex wakes*. It is of interest to note that in the early stages of development of the latter flows, the starting eddies have the familiar circular forms seen in figure 2. Frames (*b*) and (*c*) in the sequence of figure 5 show that the cyclonic eddy is shed from the obstacle before it can elongate to the same extent as the starting eddy in figure 4 (frames (*c*) and (*d*)). Thus the time at which the shedding of the first eddy occurs is not determined solely by the eddy length.

For the cases shown in figures 4 and 5, it is clear that the transient flow development may be regarded as being terminated when the first isolated starting vortex is formed, since, for such cases, isolated vortices continue to form in the wake in the fully developed flow. Indeed, the criterion adopted for the identification of isolated eddy wake flows was that a shed starting eddy should be succeeded by one or more shed eddies of the same sense. These points assume particular significance when the flow régime diagram summarizing flow types is compiled (§4.2.1).

For the case shown in figure 2, where the flow in the fully developed state is steady, and the sizes of the attached eddies are constant, the only further evolution in the flow is in the growth of the length of the tail of fluid dragged along by the obstacle. Thus, for this attached eddy pair flow, the termination of the transient flow phase can be identified readily by the size of the eddy pair structure reaching a constant value. Transitional flows were deemed to be present when either the wake showed sinuosity, and/or no more than one isolated starting eddy was formed downstream of the cylinder. Both of these criteria were used because it was sometimes not possible to determine how many starting eddies had been formed for flows such as figure 3.

Thus far, all of the flow sequences have been for relatively high values of the Burger number ($Bu > 20$). Experiments with mid-range ($10 < Bu < 20$) and low ($0 < Bu < 10$) values of Bu indicate that variations in Bu have no significant effects upon either the transient developments

or the fully established structures of the above three flow types. The only noticeable effect of decreasing the value of *Bu* is to cause a slight reduction in the length and width of the tail of fluid carried along by the obstacle.

The flow types have been discussed so far with reference to the uncoupled frame fixed in the undisturbed rotating flow. Further information on the flow structure and development in these cases can be gathered from flow visualization data from the coupled frame fixed in the obstacle. Illustrative examples of such data are shown in figures 6–9, plates 5–8. The time development of the overall flow field is shown for two shedding flows in figures 6 and 7. In the first four frames of the sequence of figure 6, a separation bubble is seen to grow symmetrically at the rear of the cylinder; subsequently, the constituent eddies within the bubble are seen to fluctuate with time in size and shape, until the first eddy is shed. Thereafter, eddies of opposite polarity grow in antiphase with each other within the separation bubble, before being shed periodically into the wake. In the frame of reference of the moving obstacle, the fully developed vortex street wake is revealed as a regular series of peaks and troughs separated by distances which depend upon the velocity of the flow (see figures 6 and 7).

The evolution with time of the envelope of the separation bubble can be followed in figures 8 and 9 with the aid of the dye precipitation flow visualization technique. In the cases classified as attached eddy pairs (figure 8*a*), the dye data show clearly the formation of the constituent eddies within the bubble, and the joining of streaklines originating at the cylinder surface to form the closed envelope of the bubble itself. Figure 8*b* shows the form of the streakline trajectories originating at the cylinder surface for a case in which vortex shedding is occurring. Note, in particular, the asymmetrical structure of the constituent eddies in the developing near wake, and the characteristic vortex shedding streakline patterns (Boyer & Davies 1982) in the far wake. Figure 9 is included to illustrate the extreme sensitivity of the flow type to the value of the Rossby number. For example, in figure 9*b* the vortex shedding flow is established, with the form of the wake being identical with that in figure 8*b*. However, when the Rossby number is reduced slightly, the flow is seen to be transitional in nature (figure 9*a*). Note in the latter sequence, that though an anticyclone has been shed at an early stage of the transient flow development, the final fully established pattern consists of an attached eddy pair with slight waviness in the wake. For this reason (see above) the flow is classified as transitional.

Finally, it is noted that the full cylinder experiments confirmed the existence of wake asymmetry for cases in which the fluid was weakly stratified or homogeneous. Specifically, the cyclonic contributions to the wake structures were stronger than those of the anticyclonic counterparts. This property of wake asymmetry for homogeneous and weakly stratified rotating flows has already been established from other studies (Boyer & Davies 1982; Boyer *et al.* 1984*b*; Chabert d'Hieres *et al.* 1989, 1990) and it will not be pursued further here.

4.1.1. *Aspect ratio and blockage factor effects*

The experiments described above were conducted with the largest of the two full cylinders. With the smaller diameter cylinder, no significant aspect ratio or blockage factor effects were observed in either (i) the qualitative characteristics of the three flow types occurring as the value of the Rossby number was varied, or (ii) the lack of dependence of such flow types upon the value of the Burger number. Quantitative data from both full cylinder experiments will be presented below.

4.1.2. *Growth rates of starting eddies*

To quantify the transient processes revealed by the flow visualization data, a number of measurements were made from the latter on the variation with time of characteristic observables of the flow. The first observables to be measured were the sizes of the starting eddies, and their variation with time, as functions of *Ro* and *Bu*. Figure 10*a* and *b* show definition sketches for the eddy lengths $L(t)$ and $B(t)$ in the uncoupled and coupled flow visualization frames respectively. In the former, the length L is defined as the distance from the rear of the cylinder to the furthest point downstream at which the cross-channel velocity component vanishes. The size B of the separation bubble is defined as the distance downstream from the cylinder to where the axial velocity of the fluid is zero with respect to the velocity of the cylinder. Thus, because of the presence of the free stream velocity U_0 in the transformation between the coupled and uncoupled frames, the values of B will be smaller than those of L.

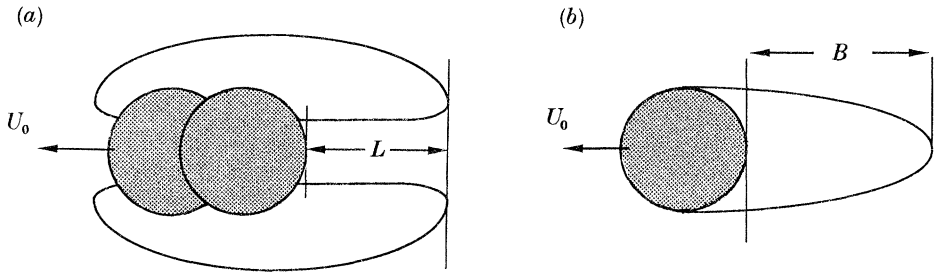

FIGURE 10. Definition sketches of $L(t)$ and $B(t)$ eddy lengths for (*a*) decoupled, and (*b*) coupled frames, respectively.

Figure 11 includes several non-dimensional plots of the temporal growth of both quantities, for values of *Ro* and *Bu* typical of the attached eddy pair régime. In general, the eddy sizes are different for the two senses of eddy circulation, but the lack of any systematic dependence of L or B upon eddy polarity indicates that these differences are probably due to the effects of secondary flows in the channel (Boyer *et al.* 1987). The growth of the eddies with time is shown to be smooth and continuous, with rapid increases in both L and B in the early stages of the transient adjustment phase, followed by more gradual approaches to asymptotic values. A satisfactory empirical representation of the growth process is:

$$[L^*, B^*] = [L_0^*, B_0^*]\,((1-\exp(kt_A^*)), \tag{1}$$

where $L_0^* = (L/D)_0$ is the estimated asymptotic value of $L^* = L/D$, $t_A^* = U_0 t/D$ is the dimensionless time, and $-k(Ro, Bu)$ is an eddy growth factor. By plotting the data in accordance with the rearranged version of (1):

$$\ln[\ln(1-L^*/L_0^*)] = \ln k + \ln t_A^*, \tag{2}$$

the factor k can be determined for different parameter combinations. Such a procedure reveals (Davis 1989) that measurements taken in one of the two frames of reference are consistent with those from the other, and that there is no systematic dependence of k upon either *Bu* or *Ro* indicates that the growth of the eddies is essentially independent of the background rotation and the density stratification. The values of the quantity $1/k$, which is the dimensionless time after the start of the motion at which L^* and B^* are within 1/e of their final values, lie between

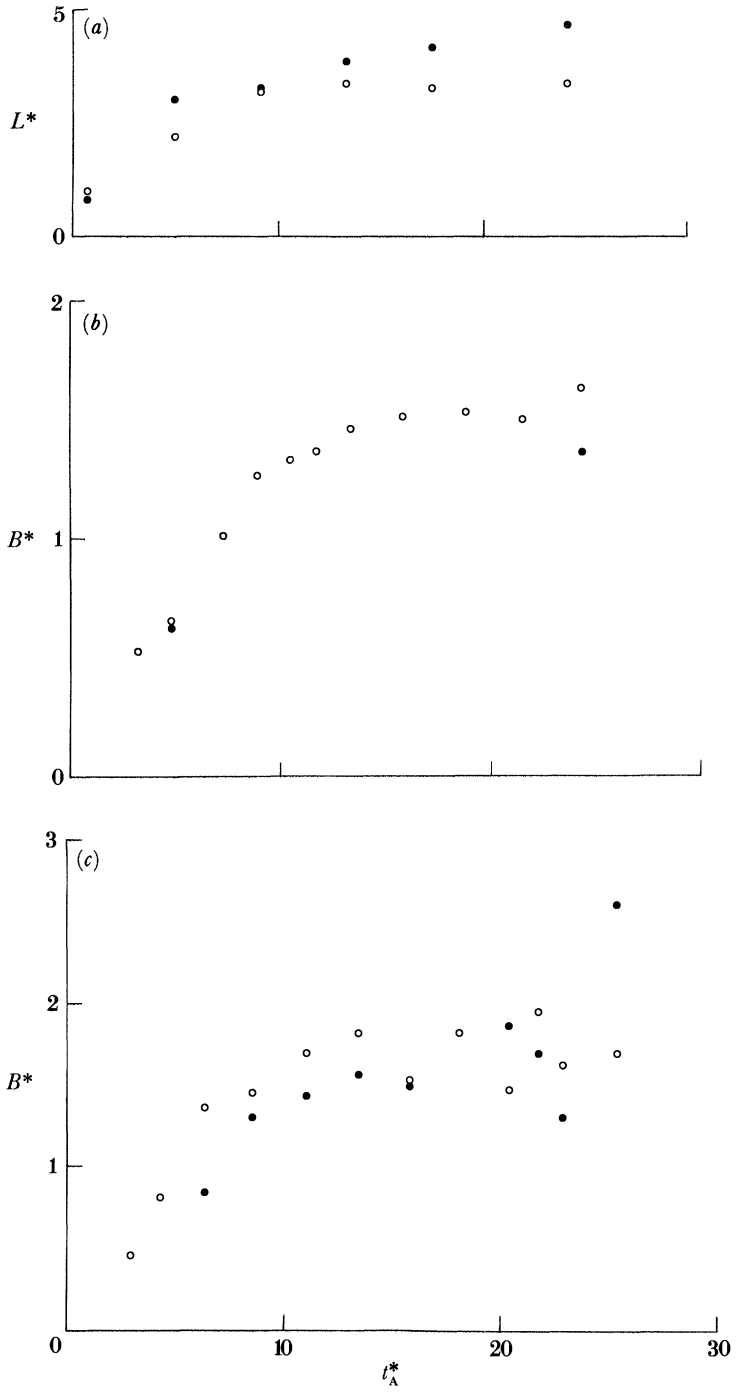

FIGURE 11. Attached eddy pair régime: plots against t_A^* of (*a*) L^* and (*b*, *c*) B^*, for $E = 9.4 \times 10^{-5}$, $h/H = 1.0$, $H/D = 2.5$, and $\{Bu:Ro\}$ = (*a*) {8.85:0.029}, (*b*) {10.56:0.033}, and (*c*) {2.56:0.043}. Open and closed symbols represent cyclonic and anticyclonic starting eddies respectively.

approximately 6 and 10. When these results are compared with those presented previously for corresponding non-rotating flows of homogeneous or stratified fluids, a number of difficulties arise. Firstly, measurements of attached eddy lengths in non-rotating flows are restricted to values of the Reynolds number below the critical value (approximately 40) for vortex street formation, in contrast to the present rotating flow investigation, where measurements of attached eddy pairs were made in the Reynolds number range 60–230. Such a discrepancy between the Reynolds number ranges precludes direct quantitative comparisons between the two cases. Secondly, any comparisons have to take account of differences in the aspect ratios of the obstacles and the blockage factors.

Notwithstanding the above difficulties, it is useful to compare some of the present data with existing measurements of non-rotating low Reynolds number cases. The growth rate curves shown by Honji & Taneda (1969) for homogeneous flows indicate that, for a Reynolds number range $30 < Re < 300$, the initial growth rates of attached and shed eddies is linear and is given by an empirical relation:

$$B'^* = (0.4)\, t_A^*. \tag{3}$$

For the cases where the flow is attached, the growth curve shown in Honji & Taneda (1969) flattens out to a constant value much more rapidly than in the cases presented in figure 11. Similar conclusions can be drawn from the growth rate curves presented for non-rotating homogeneous cases by Coutanceau & Bouard (1977*a*, *b*) for $Re = 20$–40 and blockage factors of 0.12. In general, it can be concluded that the eddy growth rates in the case of non-rotating homogeneous flow appear to be more rapid than the counterpart cases of rotating stratified flow. This would seem to indicate that vorticity is generated more rapidly in the shear layers on the cylinder in the non-rotating cases, and may explain why shedding occurs at much lower Reynolds numbers than in rotating stratified flows.

Taneda (1956) showed that the asymptotic value of the attached eddy length for the two-dimensional ($h/D > 5$) homogeneous flow was a strong function of Reynolds number. Specifically, it was found to vary between 0.25 and 2.0 cylinder diameters for Re values of 10 and 40 respectively. For an aspect ratio h/D of 8.2 and a blockage factor of 0.12, Coutanceau & Bouard (1977*a*, *b*) have shown that the dimensionless eddy length varies between less than 0.1 at $Re = 10$, to approximately 1.75 at $Re = 40$. The present experiments used h/D values and blockage factors of 2.5 and 0.15 respectively, so full quantitative comparisons with the above non-rotating eddy length data are not feasible. However, in a qualitative sense, it appears that the increase of the eddy lengths with Reynolds number in the rotating stratified cases is significantly less than in the counterpart non-rotating cases.

The data shown in figure 12 for the increase in eddy bubble length with Rossby number may be compared with the results of Boyer & Davies (1982) for fully developed, rotating, homogeneous flow past a cylinder. The latter showed that, for a similar Ekman number to the present study and an aspect ratio of 1.4, B_0^* varied between approximately 1.2 and 2.0 within a Reynolds number range of approximately 40 to 170. Though these values are of the same order as those indicated by the corresponding data in figure 12, care is required in comparing the data-sets directly. The length of the attached eddy bubble defined by Boyer & Davies (1982) was the distance downstream from the rear of the cylinder to the position where the lateral separation of reference streaklines originating at the cylinder walls reduced to an arbitrary value. This definition differs considerably from the definition of B_0^* used in the present study, since differences are observed in the structure of the standing eddies in the two

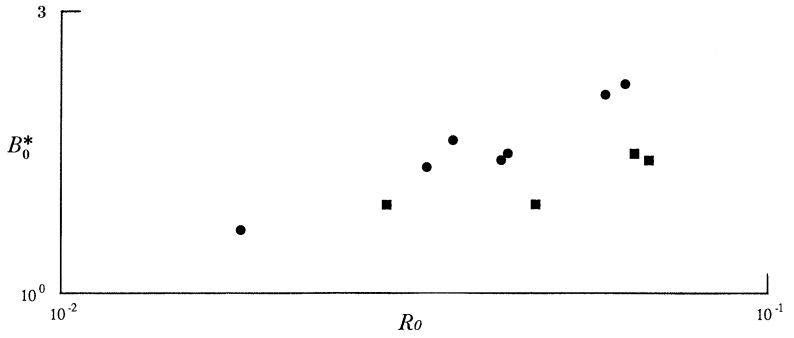

FIGURE 12. Attached eddy pair régime: plot of B_0^* against Ro, for $E = 9.4 \times 10^{-5}$, $h/H = 1.0$, $H/D = 2.5$, and $Bu =$ (●) 0, (■) 1.0–11.0.

studies. Boyer & Davies (1982) observed that the streaklines surrounding the attached eddy pair bubble tapered gradually towards the centre line in the downstream direction. However, in the present investigation, the general pattern for the attached eddy pair flow régime consisted of an attached bubble with either a rounded or irregular structure on its most downstream portion (see figure 8*a*), thus making quantitative comparisons with the Boyer & Davies data impossible.

Figure 13*a* and *b* show $B^*(t)$ and $L^*(t)$ eddy length data for typical transitional and vortex wake cases respectively, where the growth curves of the initially attached starting eddies are discontinuous. These plots all contain data in the mid-range of Bu, for various values of the Rossby number. Both show that the eddies within the attached pair grow linearly with time, until disintegration occurs after a period of between 10 and 20 advective timescales.

Note that for the flow which, when fully developed, is of the vortex wake type (figure 13*b*), the first eddies to be shed are the cyclonic starting eddies between t_A^* values of 15 and 20. Inspection of the sequence of eddy growth plots shows that the maximum lengths reached by the starting eddies are largest for the cases classified as transitional. For the vortex shedding flows, the initial growth in the size of the starting eddies is arrested prematurely as the vorticity generated by the cylinder's motion is sufficient for shedding to occur. The dimensionless size of the eddy at shedding is seen to decrease as the Rossby number increases. The maximum lengths L_{max}^* to which given starting eddies grew before either disintegration (transitional flows) or shedding (vortex wake flows) were estimated by extrapolation of curves typified by those in figure 13. Figure 14 shows a plot of L_{max}^* against Rossby number for transitional and vortex wake flows for various Bu number ranges. The previously indicated decrease of L_{max}^* with increasing Ro is confirmed by this plot.

The $B^*(t)$ measurements indicate that before the first starting eddies are shed the transitional and shedding flows have growth rates with typical gradients of almost 0.2 and between 0.3 and 0.4 respectively. These results agree quite well with existing data from non-rotating cases, where the bubble length B'^* is known to grow initially with time t_A^* as

$$B'^* = 0.37 t_A^* \quad \text{(Honji \& Taneda 1969)},$$

indicating that the presence of density stratification causes the strong control exerted by background rotation upon the eddy development to be weakened considerably.

Finally, it is of interest to note for the vortex wake cases the oscillatory variations in $L^*(t)$

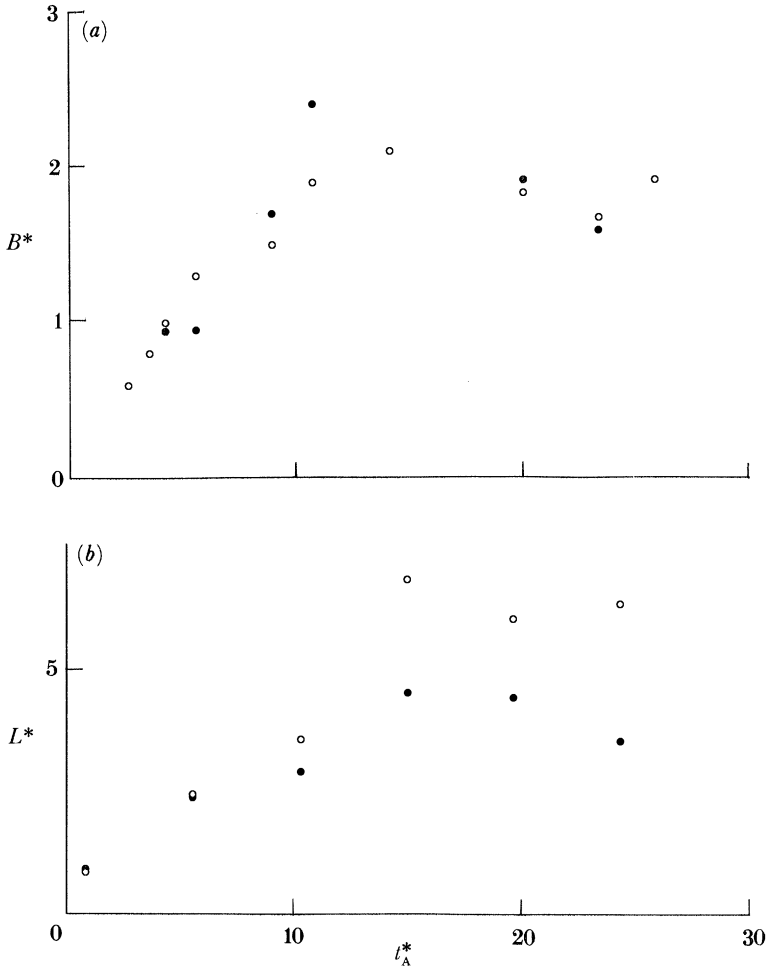

FIGURE 13. Transitional (*a*) and vortex wake (*b*) flow régimes: plots against t_A^* of B^* (*a*) and L^* (*b*) for $\{Bu:Ro\}$ = (*a*) {2.25:0.059}, and (*b*) {17.01:0.034}. Values of other parameters, and symbols, as in figure 11.

and $B^*(t)$ after the first starting eddy has been shed. This behaviour, which is evidence of eddy shedding in the fully developed flow, is seen particularly clearly in the plots shown in figure 15.

4.1.3. *Eddy retention times*

In the above section, eddy length data have been presented to show the transient evolution of vortex wake flows and the fluctuations in eddy size in the fully developed flows. In this section, the transient phase in the development of the vortex wake type of flow is explored further by focusing attention on starting eddy retention times. The eddy retention time t_r is defined as the elapsed time between the initiation of the flow and the formation downstream of the first isolated eddy of either sign. For this vortex wake type of flow, the value of t_r effectively indicates the duration of the transient growth phase of flow development.

To measure t_r, photographs of the flow were taken at pre-set intervals, and individual frames were inspected sequentially to follow the evolution with time of individual eddy structures. Values of t_r could then be computed using (i) the elapsed time since the initiation of motion to the time at which the photographic negative was exposed, (ii) the exposure interval, and (iii)

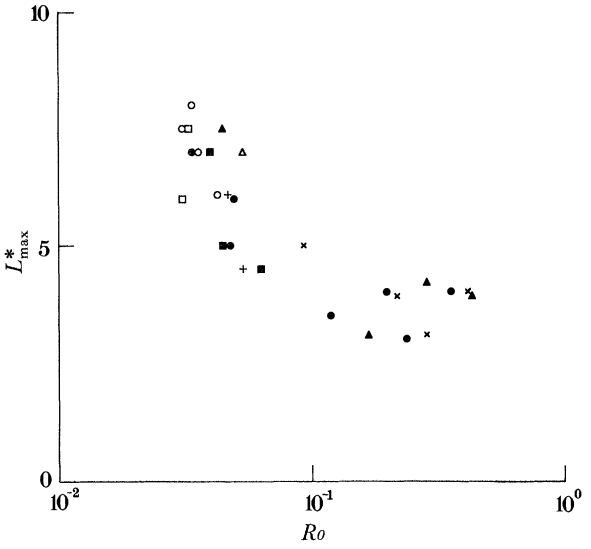

FIGURE 14. Composite plot of L_0^* against Ro for transitional (open symbols) and vortex wake (closed symbols) data for Bu values shown. Values of other parameters as for figure 12. Transitional eddies: □, 19.1–25.0; ○, 11.1–15.0; △, 0.1–5.0. Isolated vortices: ■, 19.1–25.0; ●, 15.1–19.0; ▲, 11.1–15.0; +, 5.1–11.0; ×, 0.1–5.0.

an interval based upon an interpolation procedure between two successive frames in a given sequence.

The rotating stratified system under investigation is characterized by four externally imposed timescales; namely (i) the rotational timescale $t_\Omega = 2\pi/\Omega$, (ii) the advective timescale $t_A = D/U_0$, already defined previously, (iii) the viscous timescale $t_V = D^2/\nu$, and (iv) the buoyancy timescale $t_N = 2\pi/N$. In the present study, the ranges of these timescales were as follows:

t_Ω: 13.5 s,

t_A: 1.0–86.0 s,

t_V: 500.0–3600.0 s,

t_N: 3.2–17.5 s,

while the observed values of t_r varied between 5.0 and 600 s. Thus the timescale associated with the background rotation is generally of the same order of magnitude as the observed t_r values, except at the smallest values of t_r where isolated eddies are generated faster than the time required for the influence of rotation to be effective. It can be seen from above that the retention times are of the same order as all of the other timescales except the viscous timescale t_V. The latter is always much longer than the timescale associated with the formation of the first starting eddy, being almost an order of magnitude greater for both cylinders.

The plots on figure 16 show the variation with Rossby number of the retention times t_r, normalized with the rotational period $t_\Omega((t_r)^*_\Omega = t_r/t_\Omega)$. Data are shown for the large and small diameter cylinders and for discrete Burger number ranges. Though these plots show some scatter, the data on each show no significant dependence upon the Burger number, indicating that the stratification has little direct effect upon the eddy retention times. Both plots show linear decreases in $\ln[(t_r)^*_\Omega]$ with increases in $\ln[Ro]$.

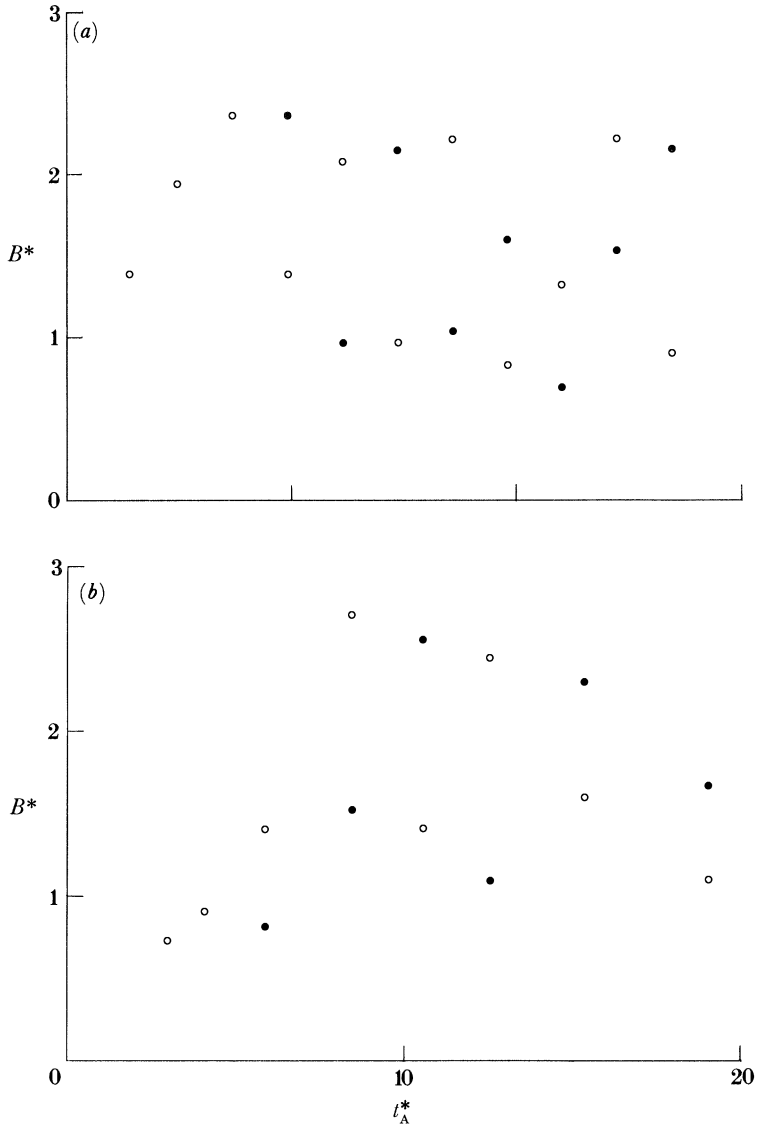

FIGURE 15. Transitional (*a*) and vortex wake (*b*) flow régimes: plots of B^* against t_A^* for cyclonic (open) and anticyclonic (closed) eddies and values of $\{Bu:Ro\}$ = (*a*) {2.25:0.059}, and (*b*) {0:0.079}. Other parameters as for figure 12.

It is clear that for both full cylinders, the Rossby number is sufficiently large in some cases to produce scaled retention times $(t_r)_\Omega^*$ significantly less than unity, and for such cases, the first isolated eddy is formed after a fraction of a rotational period following the impulsive start. Since it is also clear from figure 16*a* and *b* that the magnitude and functional variation of the scaled retention time is also dependent on the aspect ratio of the obstacle, it is convenient to investigate this dependence further by plotting the dimensionless retention time $(t_r)_N^* = t_r/t_N$ against the Froude number $Fr = (U/Nh)$. In this way, the effects of aspect ratio can be considered, and the effects of background rotation can be isolated. Such plots show (Davis 1989) that $(t_r)_N^*$ decreases with increasing Fr at the same rate for both values of h/D, and, for each case, the influence of Bu upon the tendency of the data is weak. For the $h/D = 2.5$ case

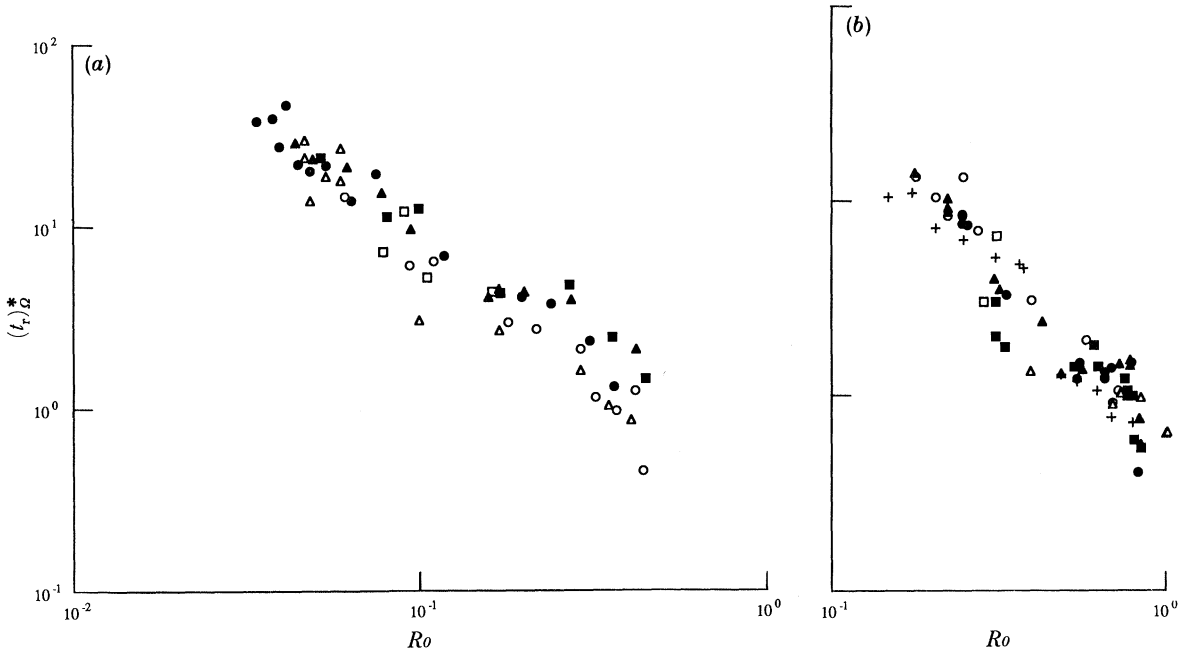

FIGURE 16. Individual plots of t^*_Ω against Ro for Bu ranges shown, and H/D = (*a*) 2.50, (*b*) 6.25. Other parameter values as for figure 12. (*a*) □, 0; ○, 1.0–7.9; △, 8.0–12.0; ■, 12.1–15.0; ●, 15.1–20.0; ▲, 20.1–25.0. (*b*) □, 0; ○, 1.0––20.0; ■, 40.1–60.0; ●, 60.1–80.0; ▲, 80.1–100.0; +, 100.1–130.0.

there is no clear significant dependence upon Bu, though for the small cylinder ($h/D = 6.25$) the data indicate somewhat higher values of $(t_r)^*_N$ at lower values of Bu, for a given Fr value. This indicates that in this case the background rotation may exert a weak influence upon the retention timescale.

On the above evidence, it is tempting to conclude that the dimensional retention time t_r depends principally upon the obstacle velocity U_0 and the diameter D of the cylinder as:

$$t_r = KD/U_0, \tag{4}$$

with the effects of rotation and stratification being very weak. K is a constant to be determined. Using the above proposed relation (4) it is straightforward to show that:

$$(t_r)^*_N = K(h/D)^2\,(Bu)^{\frac{1}{2}}[(2\pi D)\,(Ro)]^{-1} \tag{5}$$

so, for a given value of h/D, a logarithmic plot of $(t_r)^*_N$ against Ro will show a slope of -1.0 and a dependence of the intercept on Bu. Such behaviour is shown clearly in figure 17 for the large and small diameter cylinders respectively.

4.2. *Fully developed flows*

The sections above have shown that within the range of parameters studied here, the observed fully developed flows were of three main types, denoted respectively as *attached eddy pairs*, *transitional* and *vortex wake* flows. Typical examples of such flows have been presented in figures 2–5.

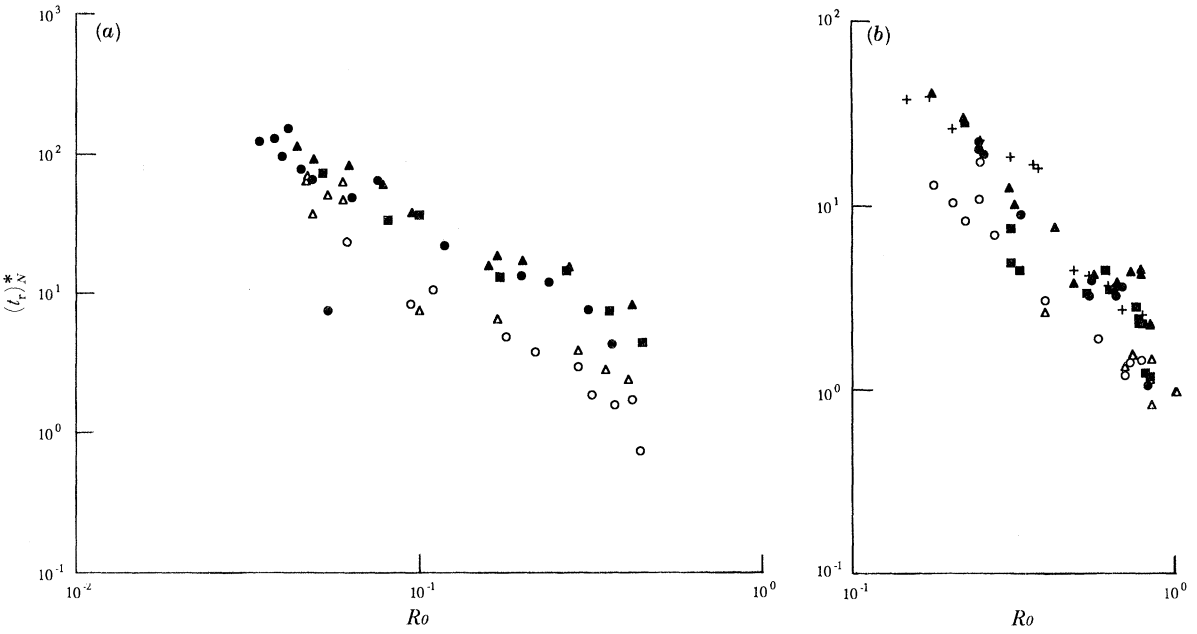

FIGURE 17. Plots of t_N^* against Ro for Bu ranges shov and H/D = (a) 2.50, (b) 6.25. Other parameters as for figure 12. (a) ○, 1.0–7.9; △, 8.0–12.0; ■, 12.1–15.; ●, 15.1–20.0; ▲, 20.1–25.0. (b) ○, 1.0–20.0; △, 20.1–40.0; ■, 40.1–60.0; ●, 60.1–80.0; ▲, 80.1–100.0; +, 100.1–130.0.

4.2.1. *Flow transitions*

The flow régime diagrams in figure 18 summarize the occurrence of each flow type in terms of the Rossby and Burger numbers, and the aspect ratio h/D. The data show that for both cylinders, the critical values of the Rossby number for vortex wake formation are strong functions of the Burger number, for low values of the latter parameter. However, as the Burger number is increased from zero, the critical Rossby number at which vortex wake formation is observed decreases sharply for both cylinders. For intermediate and high values of Bu, the critical value of Ro for vortex generation remains essentially constant for the small cylinder and decreases slowly with increasing Bu for the large cylinder. The borders of the régimes separating the three types of flow are not clearly delineated, since, at a given Burger number, the two changes of flow type (from attached eddy pairs to transitional to vortex wake flows) which occur as the Rossby number is increased, are not, in general, smooth and continuous. In some cases, the transitions between the three flow types are difficult to identify in the flow visualization data, even though it is always clear from such data when isolated eddies are present downstream of the obstacle.

Note that most of variation in the critical value of Ro for the appearance of isolated vortices in the wake takes place over ranges of Bu of 0–10 and 0–20 for the large and small cylinders respectively. Note further that for both cylinders this critical value of Ro at $Bu = 0$ is reduced to approximately half of its value at the largest values of Bu. (As stated in previous sections, the aspect ratio h/D appears in the Burger number definition as $Bu = (N/2\Omega)^2(h/D)^2$, so that for a given value of $(N/2\Omega)$ the smaller diameter cylinder has associated with it a much larger value of Bu than its larger counterpart.) Quantitative comparisons between the régime diagrams for the two cylinders illustrate that the shapes of the transition boundaries are similar,

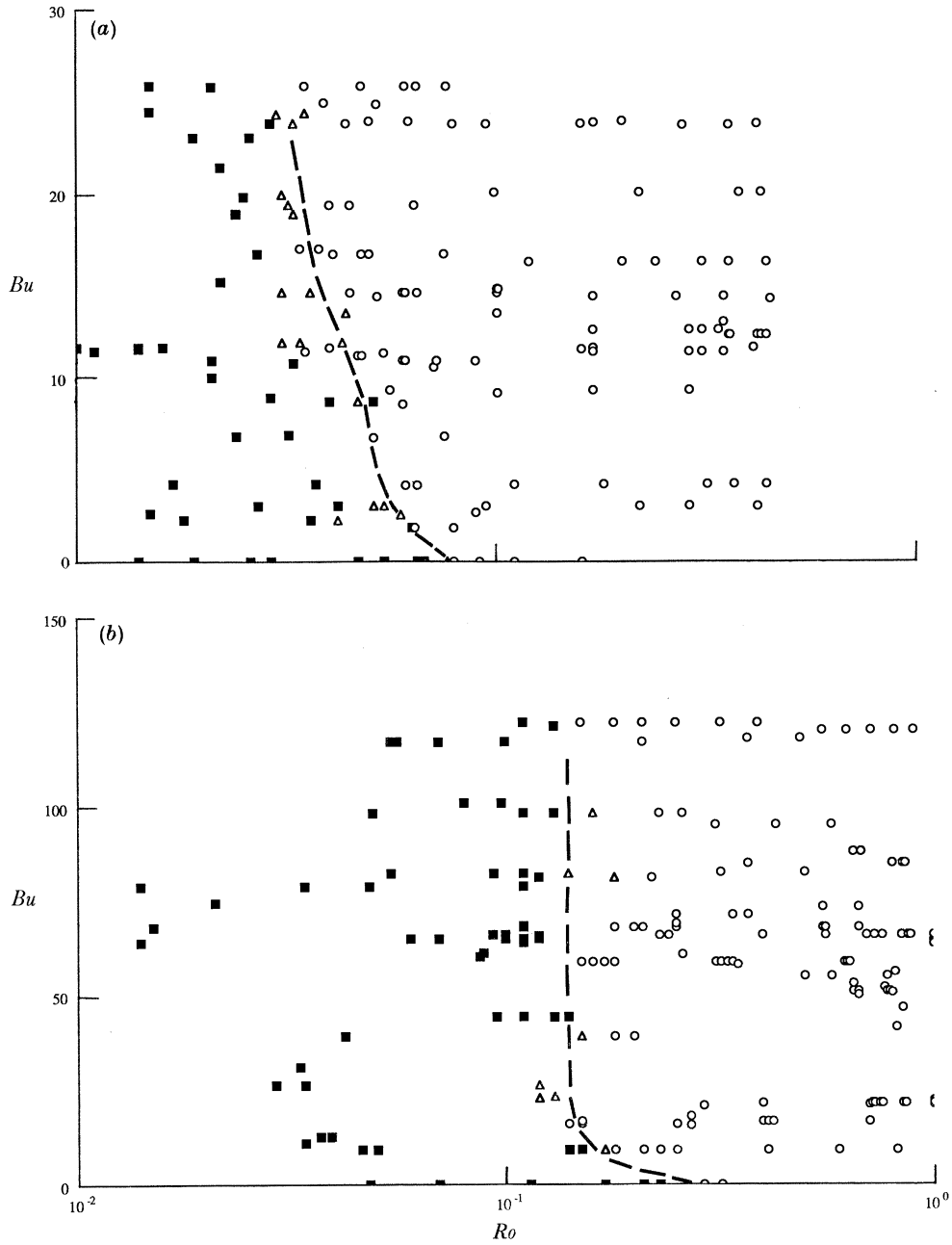

FIGURE 18. *Bu*:*Ro* régime diagrams for H/D = (*a*) 2.50, (*b*) 6.25 and other parameter values as for figure 11.

implying that the effect of varying the Burger number is to produce similar effects on the critical Rossby number for vortex wake formation for both cylinders. The values of the critical Rossby numbers for the two cylinders, for a given value of *Bu*, show that the small diameter cylinder ($h/D = 6.25$) requires systematically higher values (typically factors between 3 and 4) of *Ro* than its larger counterpart to induce vortex wake formation.

In view of this result, it is tempting to consider that the critical conditions for vortex wake formation are determined solely by the Reynolds number of the flow, as in homogeneous non-

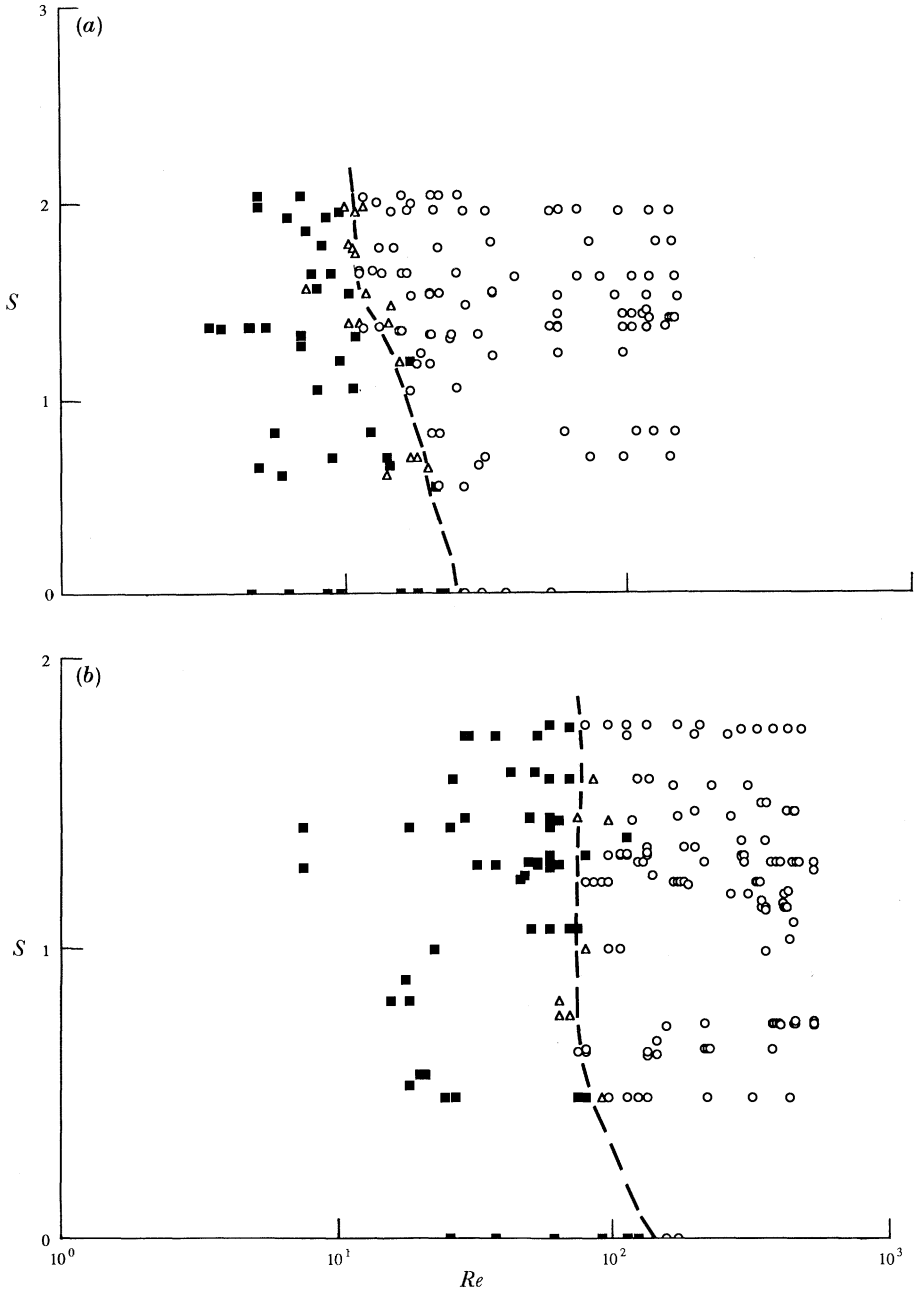

FIGURE 19. S:Re régime diagrams. Otherwise, legend as for figure 18.

rotating flow past a circular cylinder. Accordingly, the data have been replotted (see figure 19) to show the flow régimes in terms of $S = N/2\Omega$ against Re for both cylinders. However, the resulting plots show that the transitional data for both values of h/D do not collapse to a common interface between attached eddy pairs and vortex wake formation régimes. Instead, the critical value of Re at which isolated vortices are observed is significantly greater for the $h/D = 2.5$ case, particularly for relatively low values of S. This result suggests that for this parameter range the aspect ratio itself may play a controlling role in the flow transition. In this

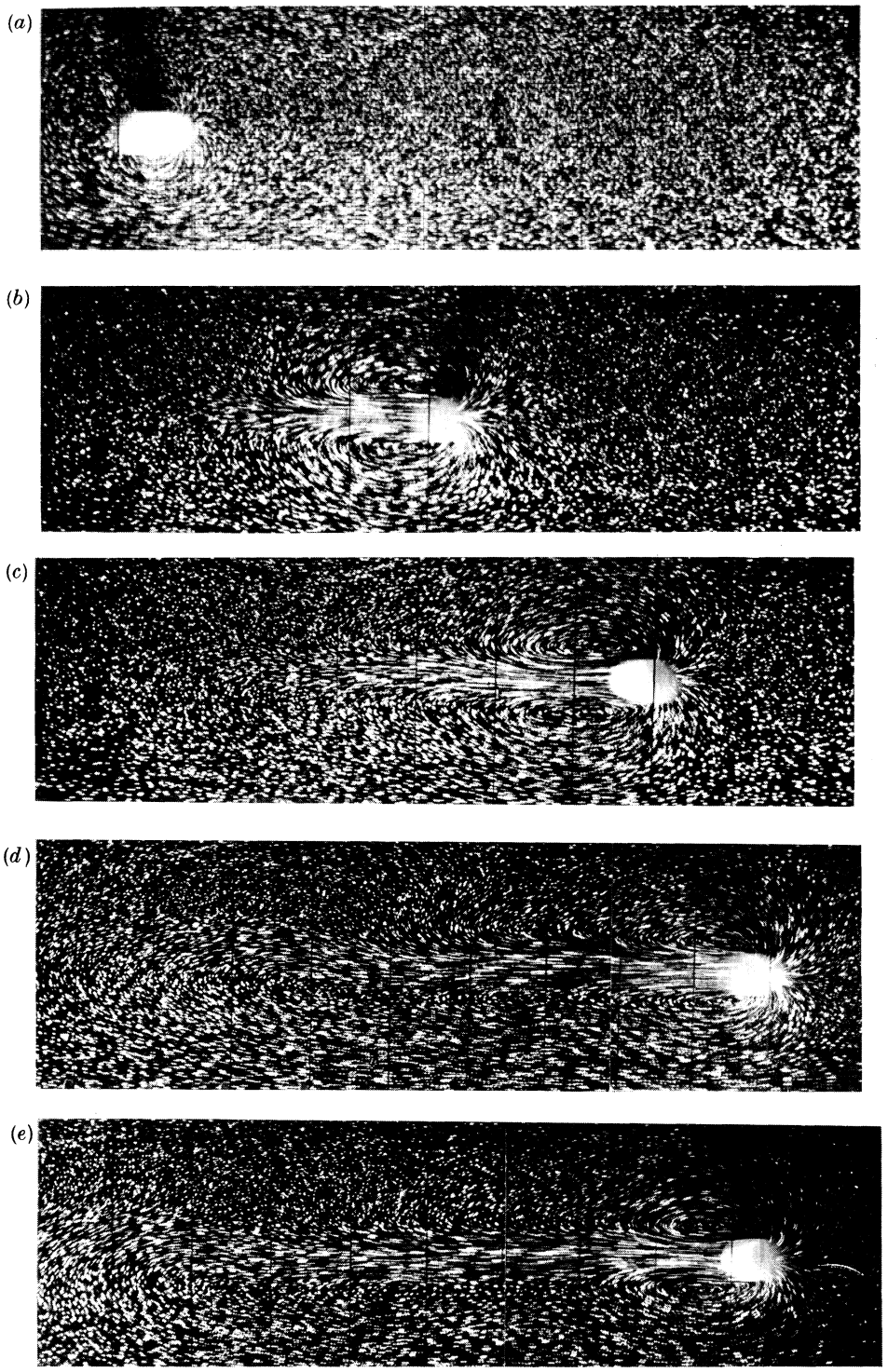

FIGURE 2. Time sequence of plan photographs in decoupled frame for $Bu = 23.8$, $Ro = 0.029$, $E = 9.4 \times 10^{-5}$, $h/H = 1.0$, $H/D = 2.5$ and t_A^* is (*a*) 0.88, (*b*) 6.21, (*c*) 15.92, (*d*) 22.48, and (*e*) 25.60. Sense of background rotation counter-clockwise.

(*Facing p.* 262)

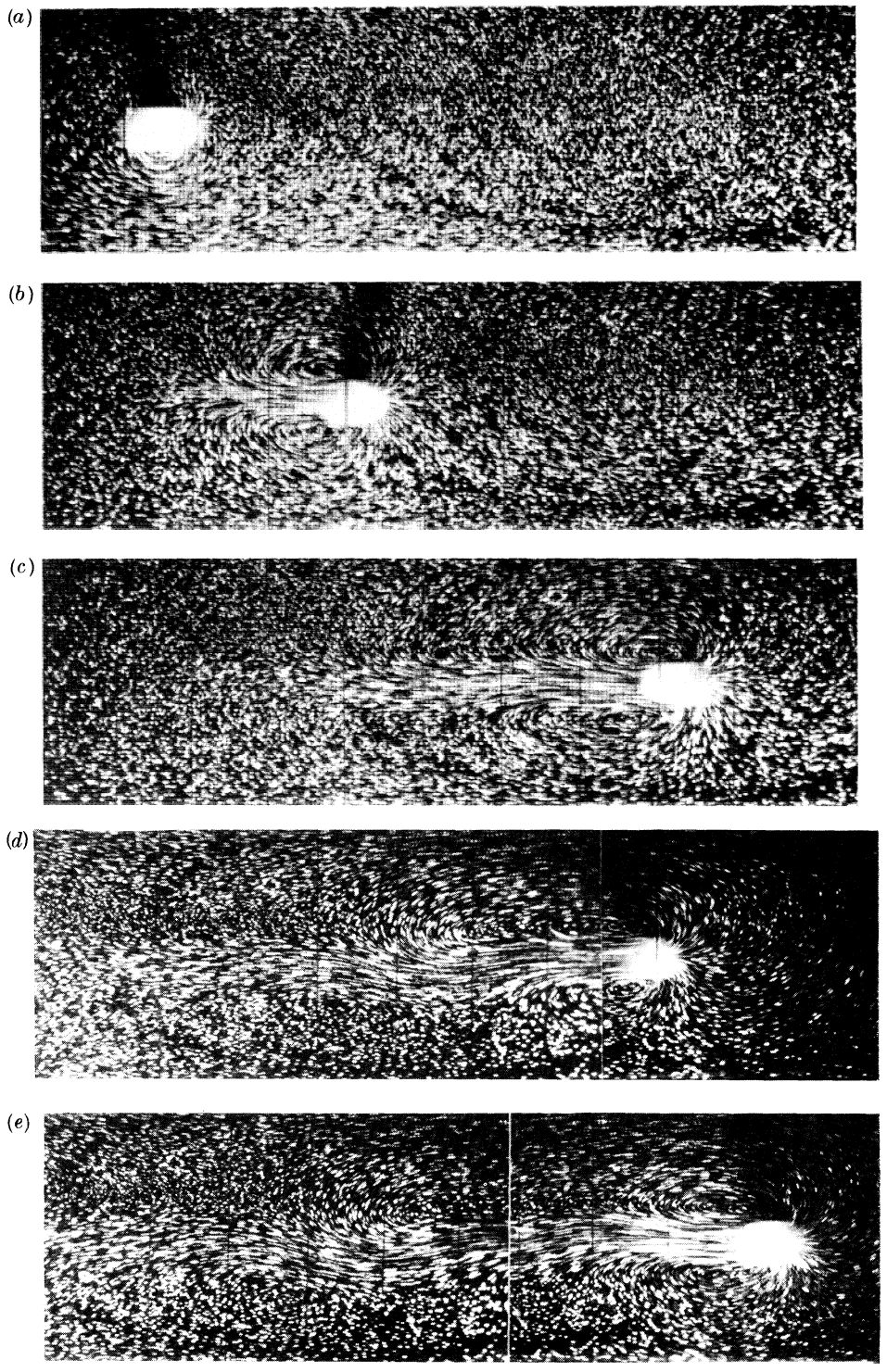

FIGURE 3. Same legend as figure 2, except $Ro = 0.033$ and t_A^* is (*a*) 0.78, (*b*) 8.52, (*c*) 14.04, (*d*) 21.30, and (*e*) 24.42.

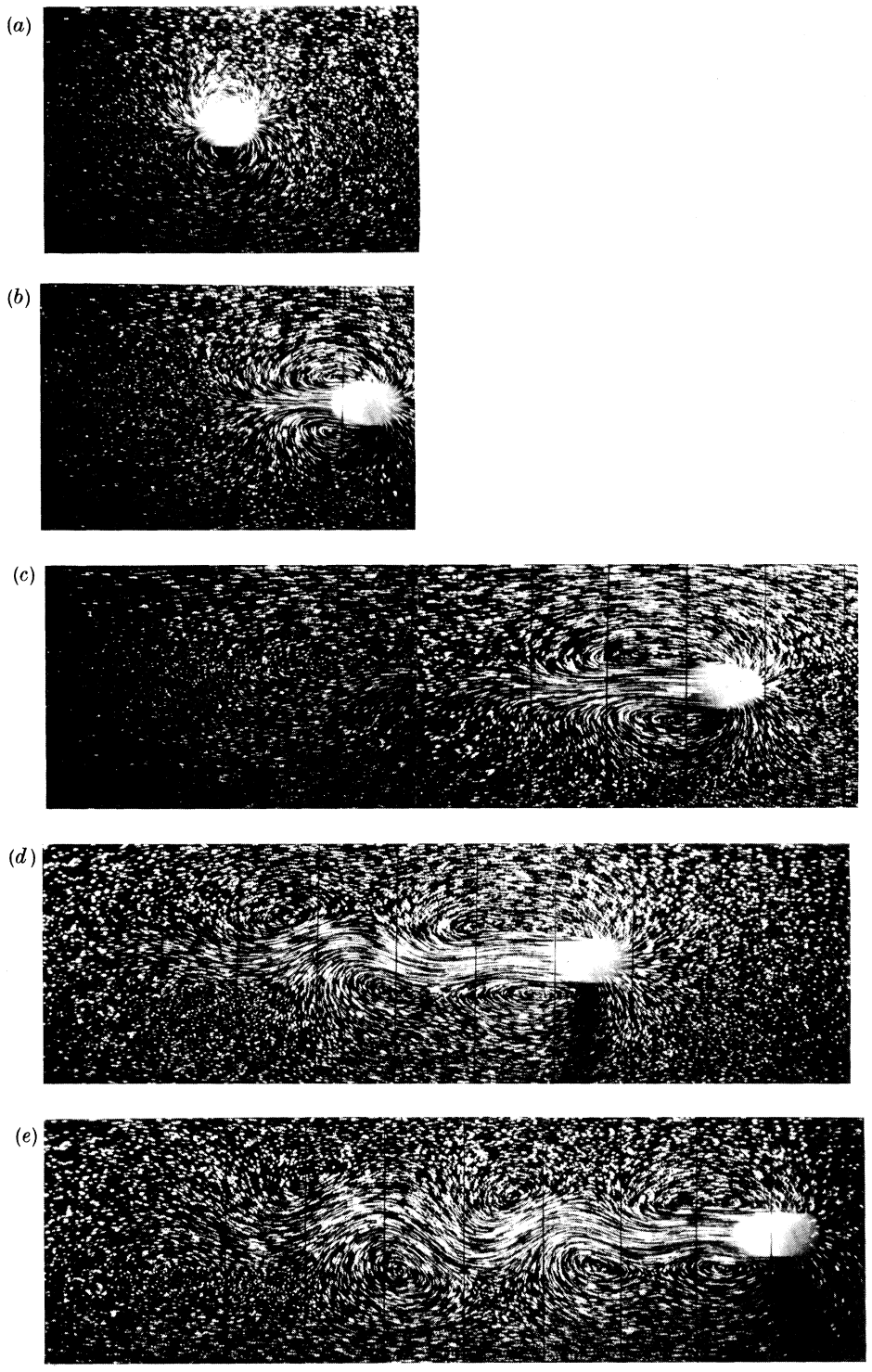

FIGURE 4. Same legend as figure 2, except $Ro = 0.044$ and t_A^* is (*a*) 0.84, (*b*) 5.24, (*c*) 12.84, (*d*) 19.08, and (*e*) 24.52.

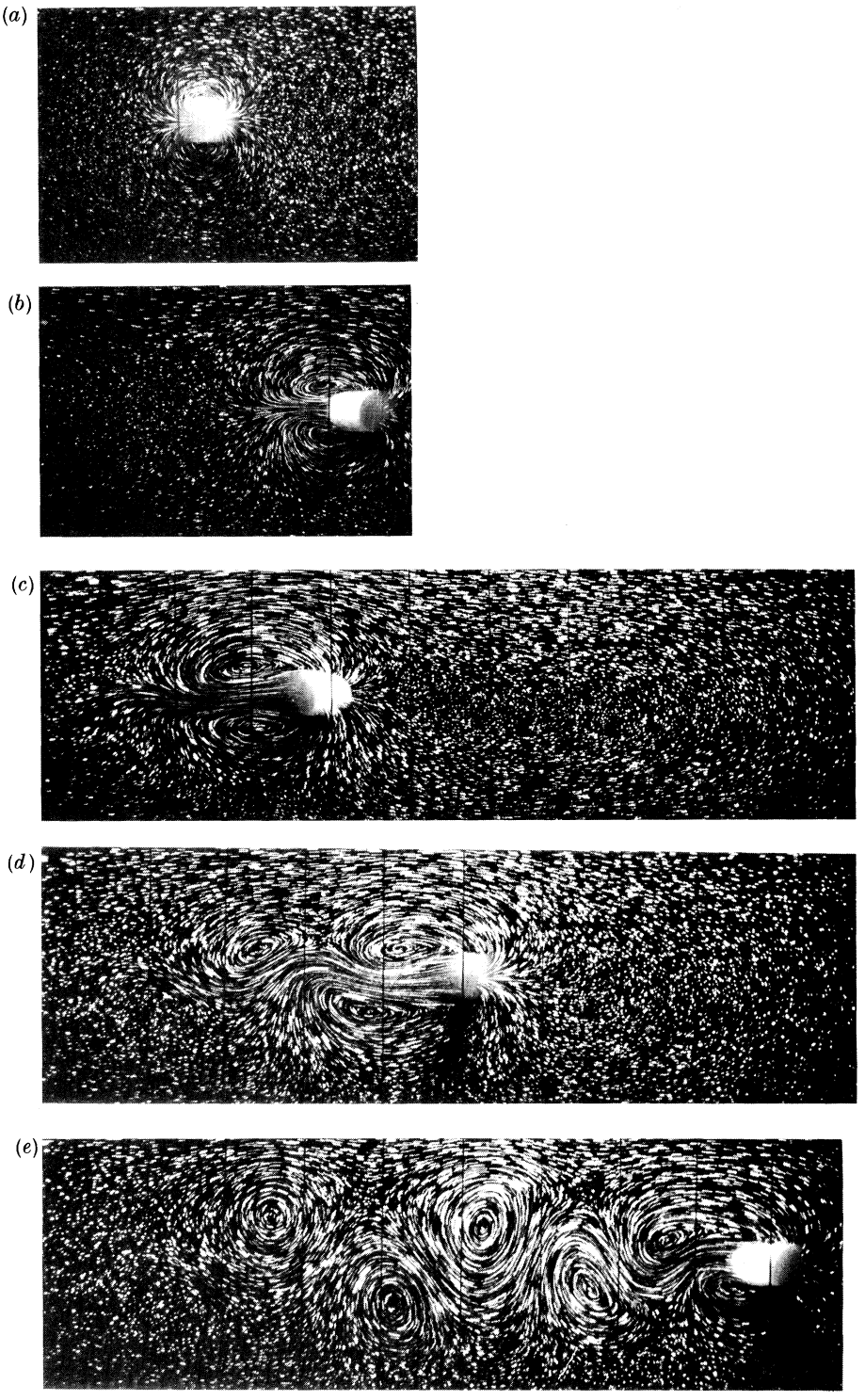

FIGURE 5. Same legend as figure 2, except $Bu = 23.9$, $Ro = 0.095$, and t_A^* is (*a*) 0.87, (*b*) 5.55, (*c*) 11.44, (*d*) 16.12, and (*e*) 24.18.

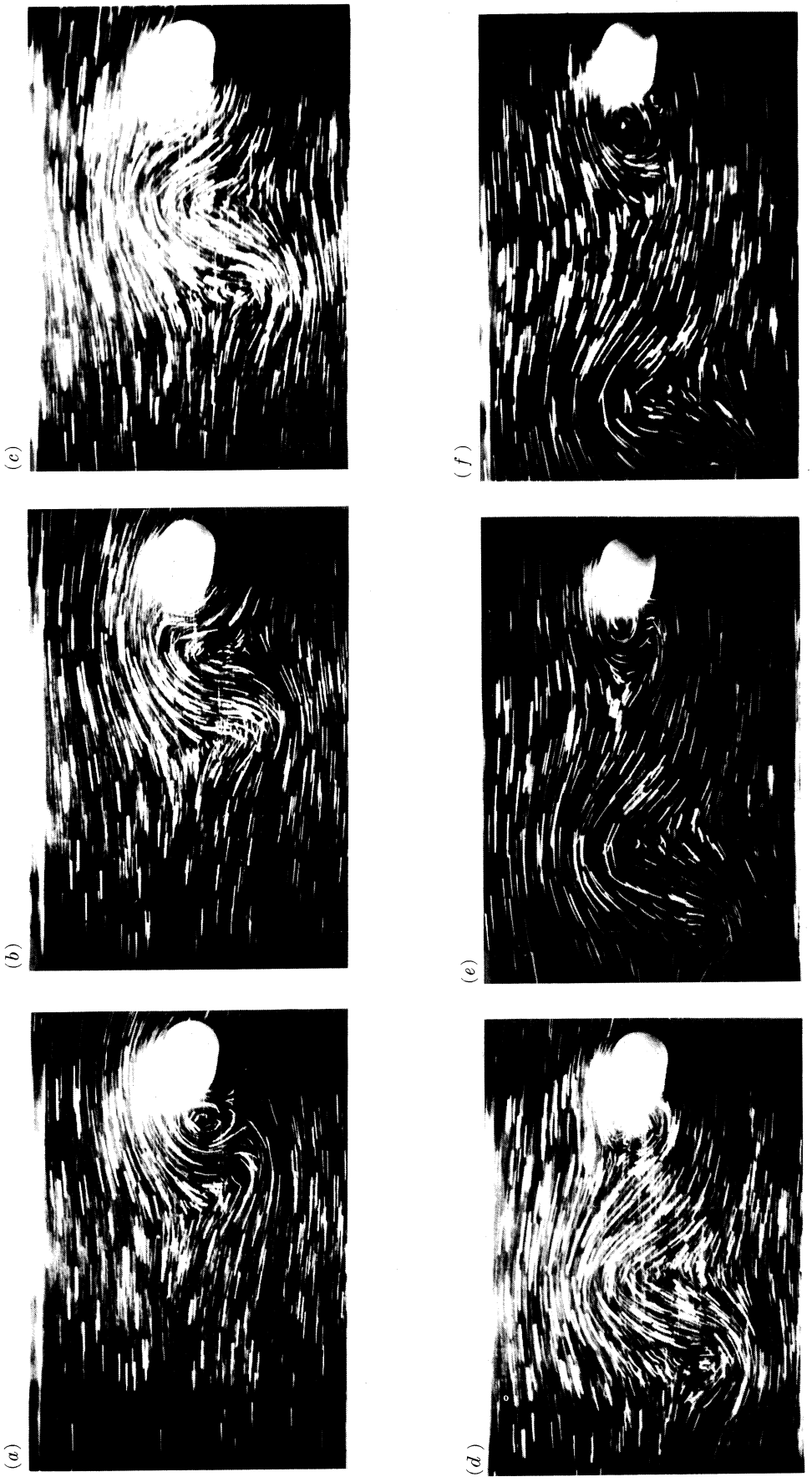

FIGURE 6. Same legend as figure 2, except coupled frame, $Bu = 11.6$, $Ro = 0.41$, and t_A^* is (*a*) 6.10, (*b*) 7.30, (*c*) 8.40, (*d*) 9.60, (*e*) 10.70, and (*f*) 11.90.

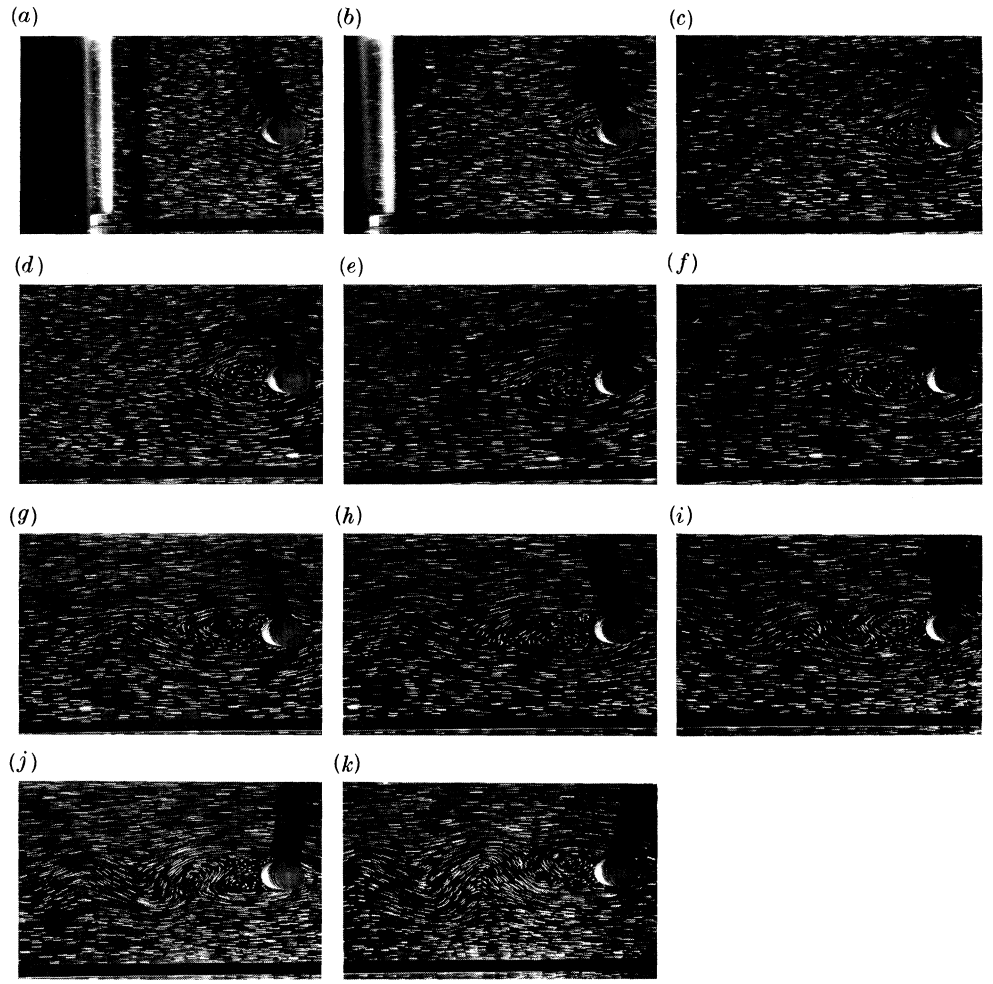

FIGURE 7. Same legend as figure 2, except coupled frame, $Bu = 25.80$, $Ro = 0.065$, and t_A^* is (*a*) 0.13, (*b*) 2.75, (*c*) 5.40, (*d*) 8.00, (*e*) 10.60, (*f*) 13.30, (*g*) 15.90, (*h*) 18.50, (*i*) 21.10, (*j*) 23.80, and (*k*) 26.40.

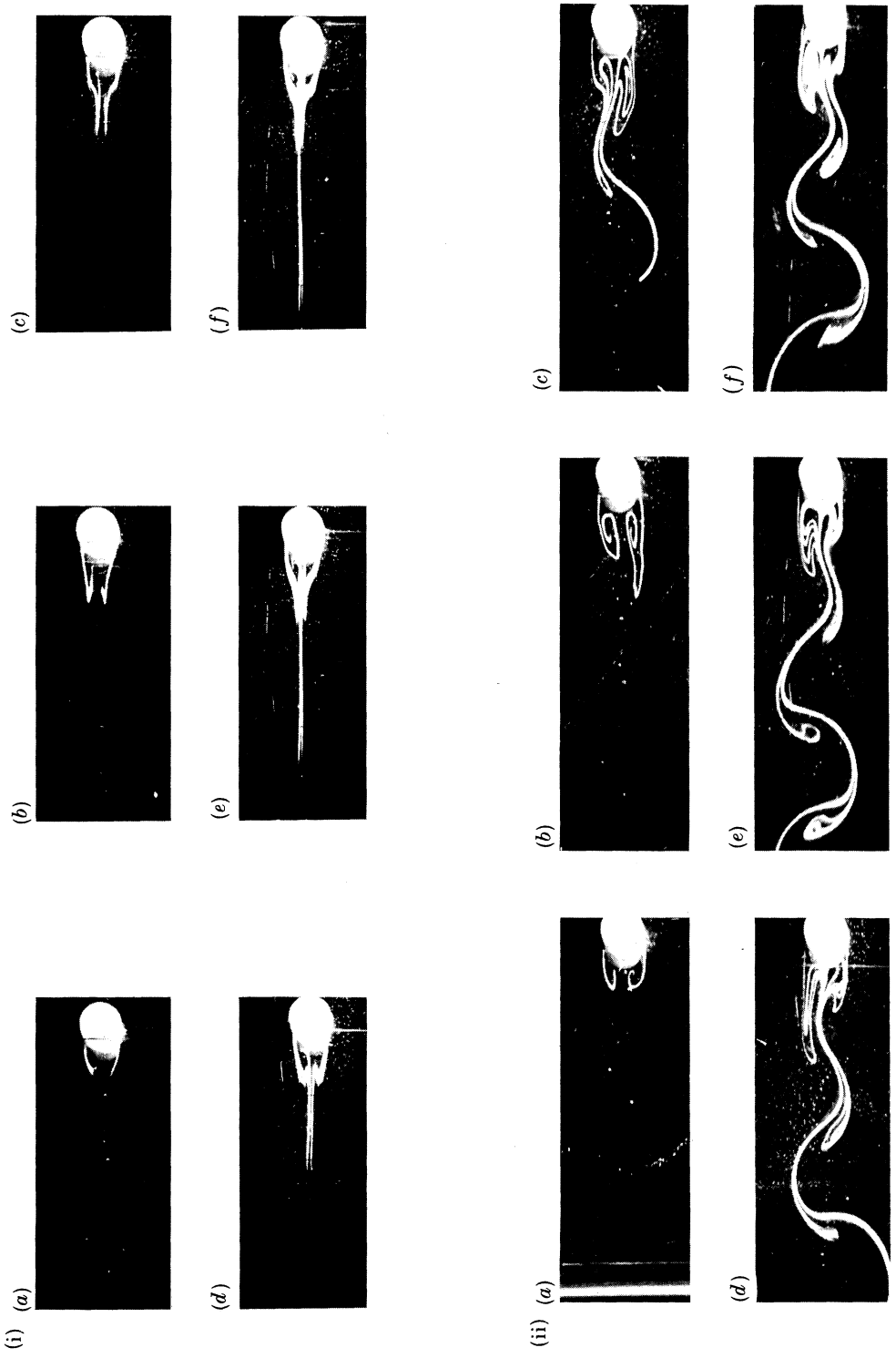

FIGURE 8. Same legend as for figure 2, except coupled frame, $Bu = 10.56$, and (i) $Ro = 0.033$, t_A^* is (*a*) 7.04, (*b*) 10.34, (*c*) 12.16, (*d*) 15.38, (*e*) 19.47, (*f*) 23.21; and (ii) $Ro = 0.071$, t_A^* is 4.17, (*b*) 8.47, (*c*) 12.30, (*d*) 15.85, (*e*) 19.61, and (*f*) 23.92.

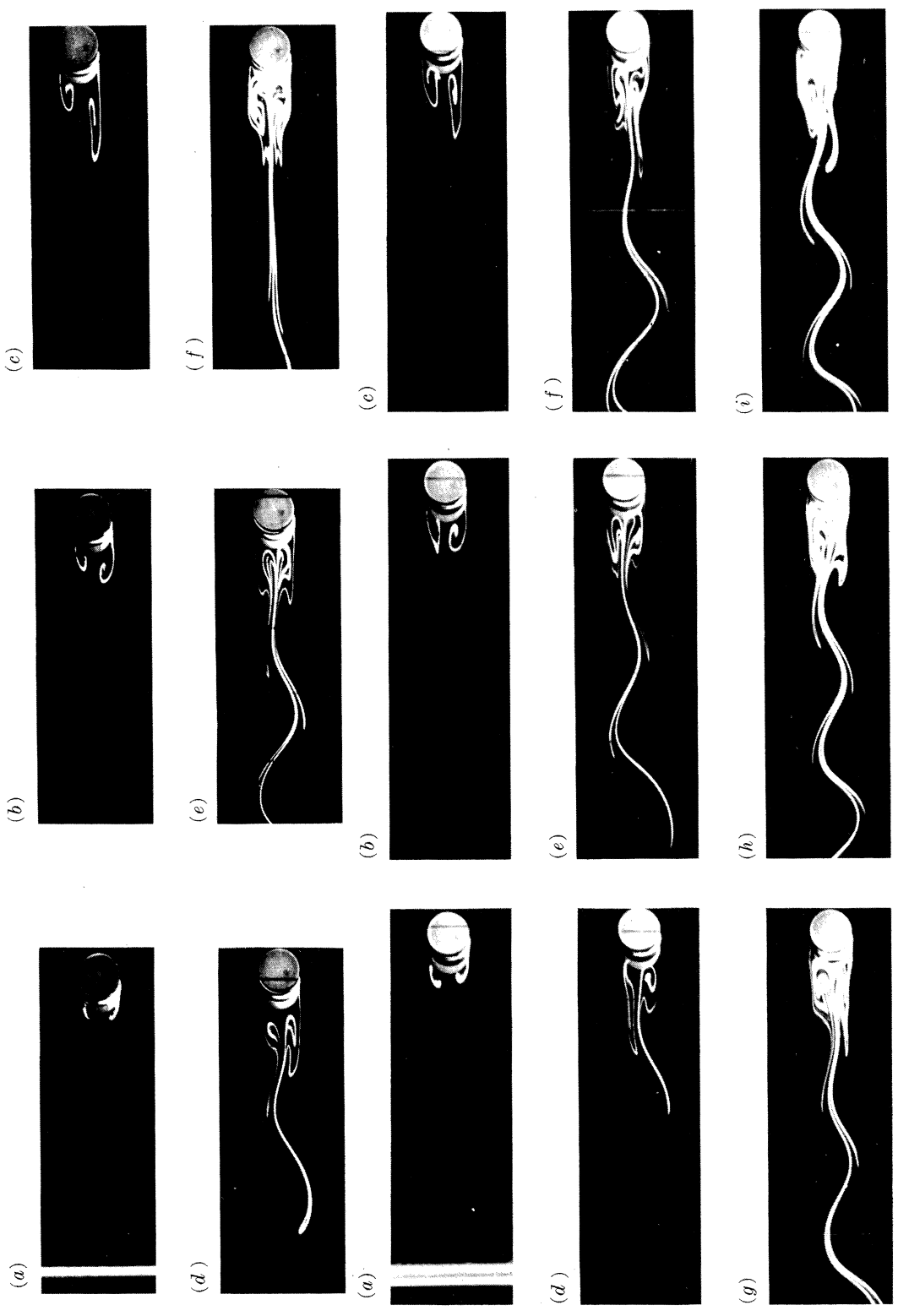

FIGURE 9. Same legend as figure 2, except coupled frame, $Bu = 1.80$, and (i) $Ro = 0.063$, t_A^* is (*a*) 2.28, (*b*) 5.16, (*c*) 9.00, (*d*) 12.60, (*e*) 19.20, (*f*) 30.00; and (ii) $Ro = 0.064$, t_A^* is (*a*) 2.86, (*b*) 4.75, (*c*) 7.12, (*d*) 10.34, (*e*) 15.33, (*f*) 18.37, (*g*) 21.41, (*h*) 24.46, (*i*) 25.79.

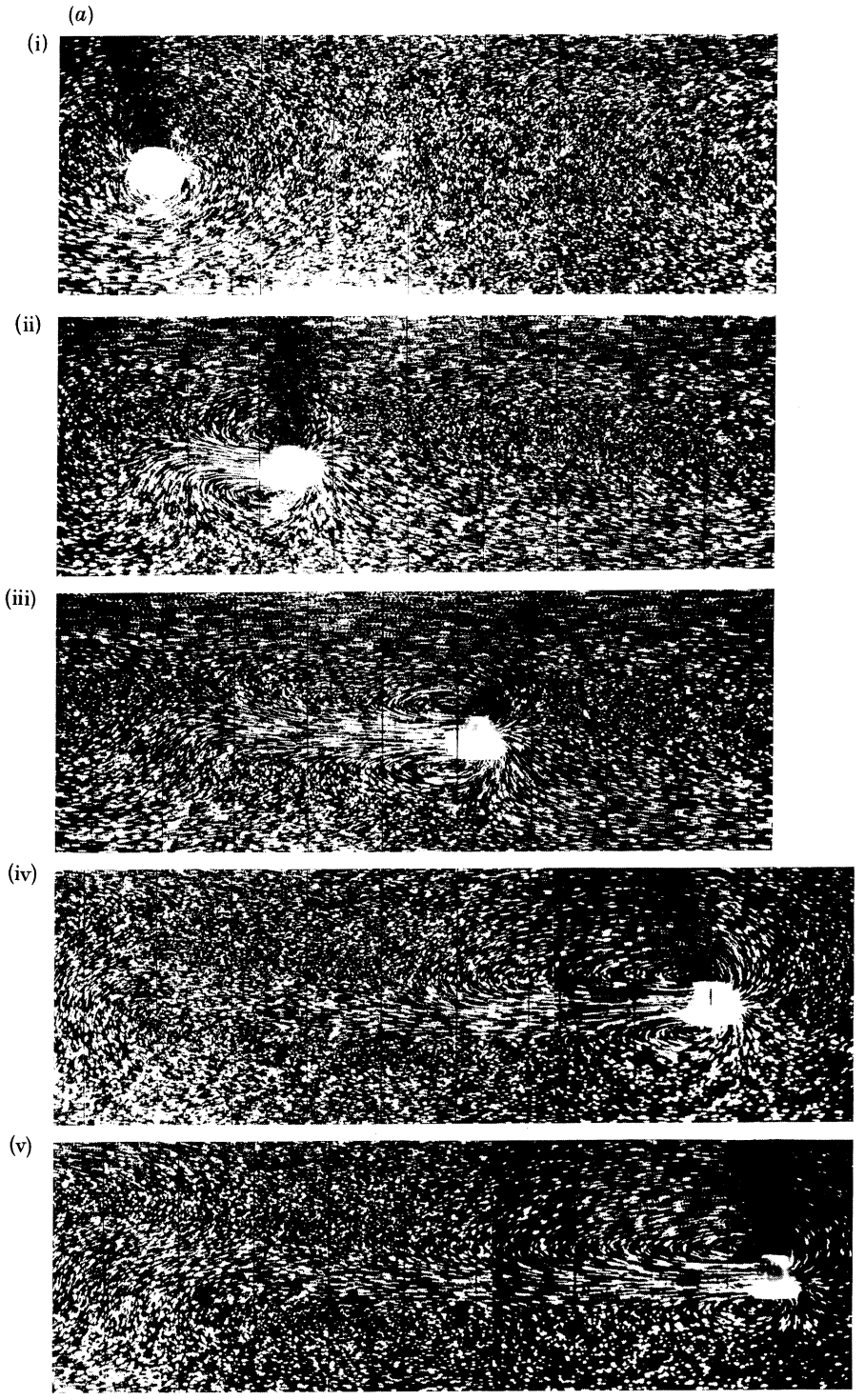

FIGURE 25. Plan photograph time sequences in decoupled frame, for $z^* = 0.2$, $E = 9.4 \times 10^{-5}$, $h/H = 0.40$, $h/D = 1.0$, and $\{Bu{:}Ro\} = (a)$ {18.75:0.024}, (b) {19.30:0.051}, (c) {18.80:0.081}. Values of $t^*_A = (a)$ 0.78; 5.10; 11.20; 22.10; 25.70, (b) 0.80; 6.30; 12.90; 23.10; 26.90, (c) 0.81; 5.40; 11.30; 22.10; 25.30.

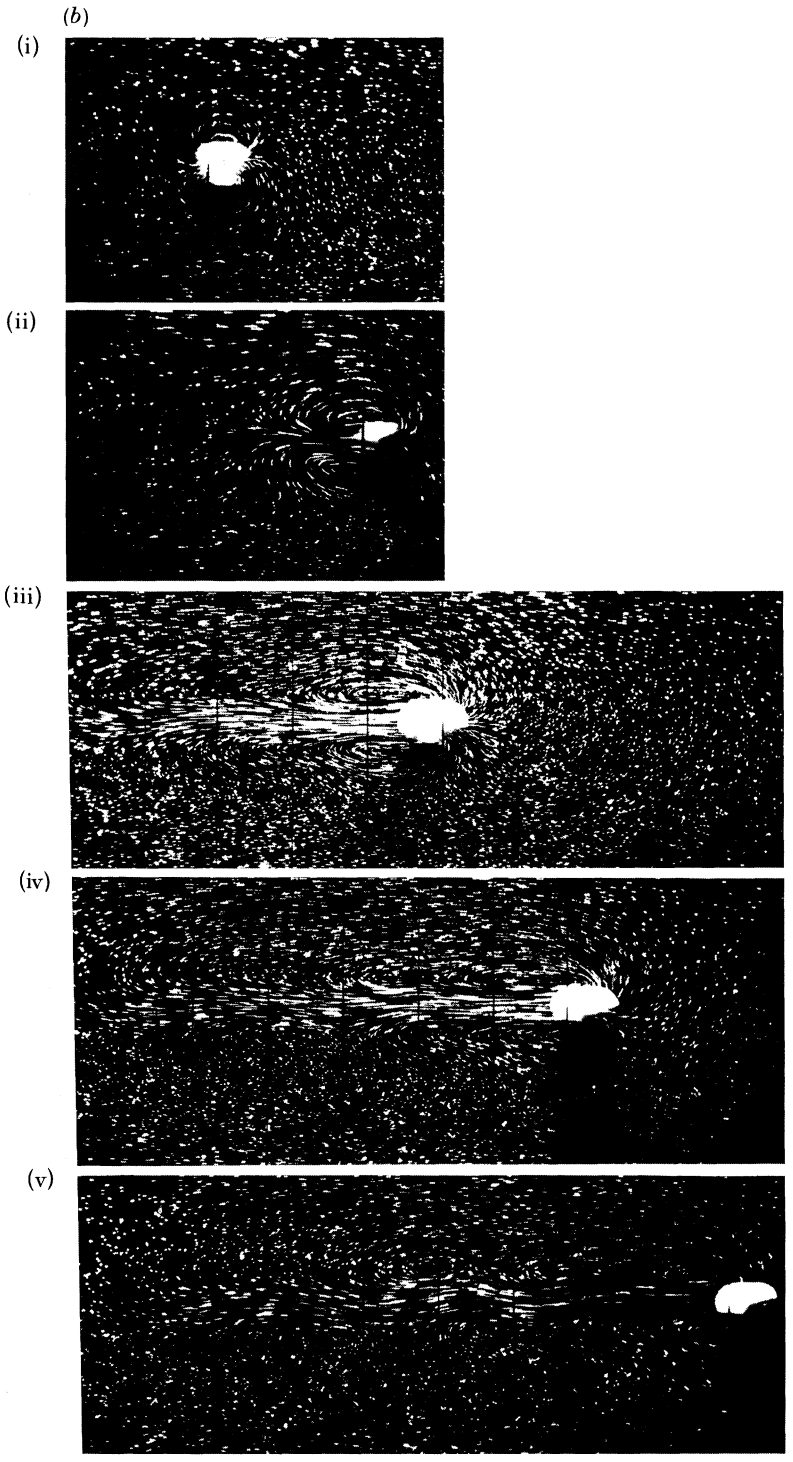

FIGURE 25*b*. For description see plate 9.

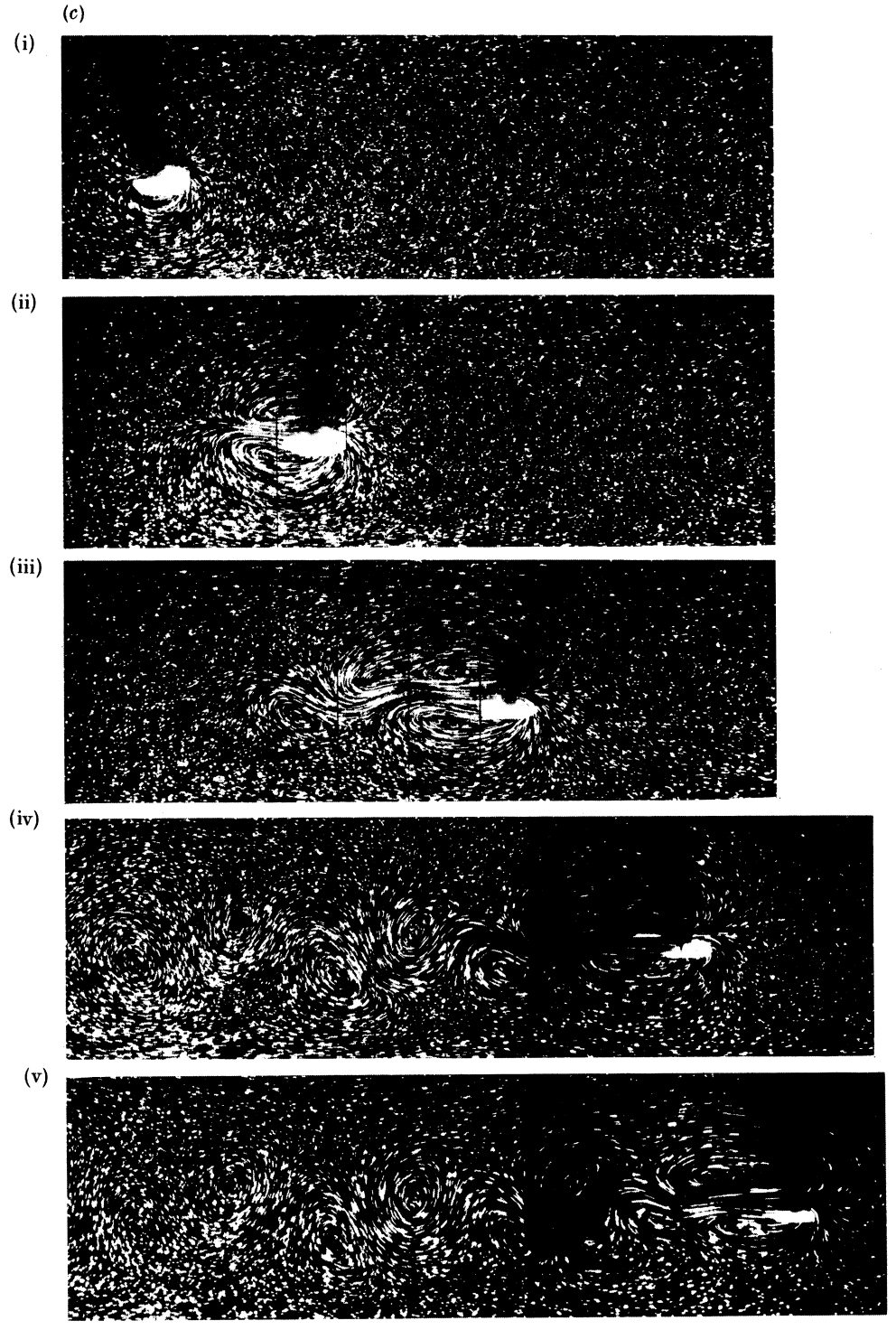

FIGURE 25*c*. For description see plate 9.

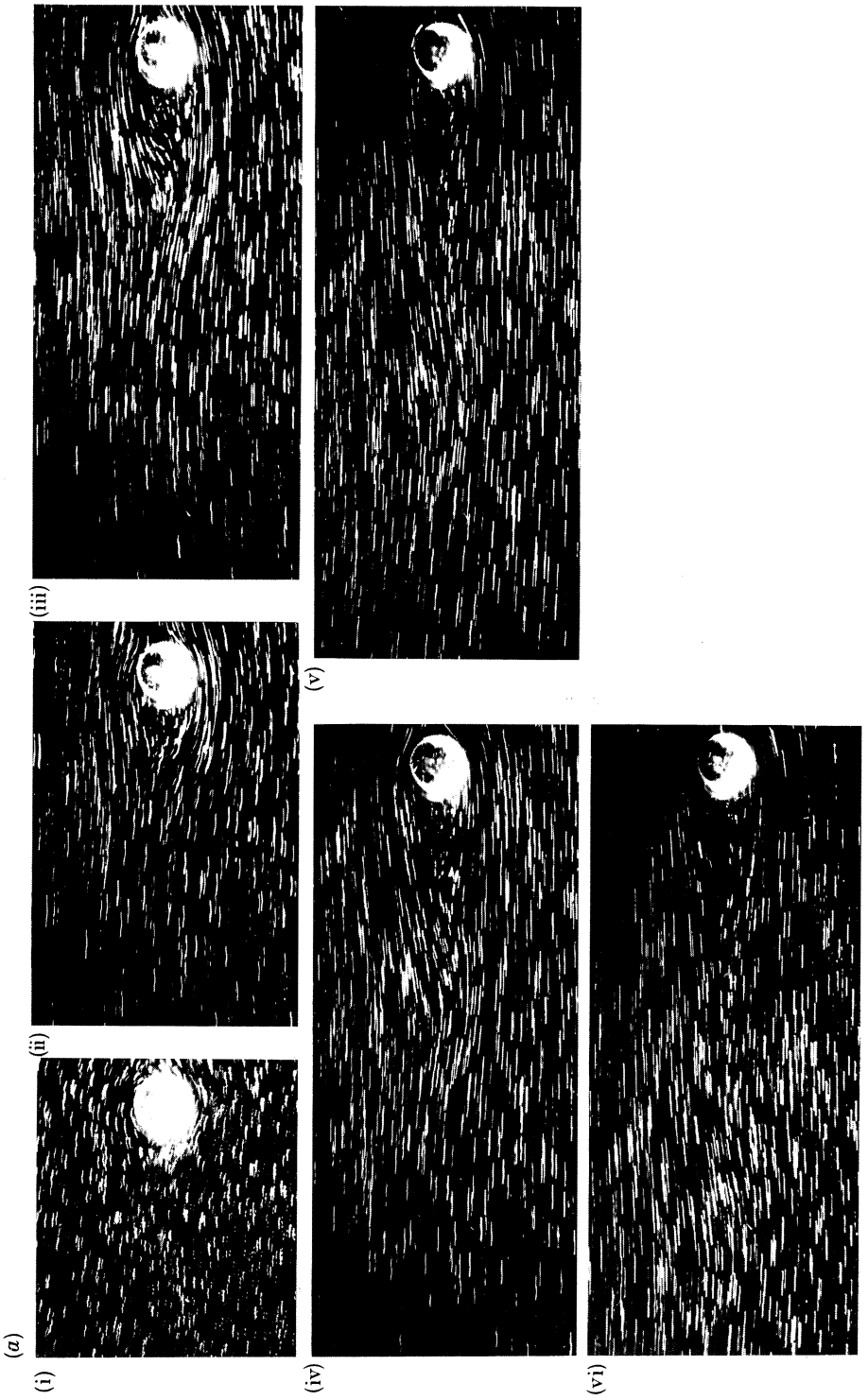

FIGURE 26. Plan photograph time sequences, in coupled frame, for $Bu = 17.6$, $Ro = 0.027$ and z^* is (*a*) 0.43, (*b*) 0.55. Values of t_A^* is (*a*) 0.63; 3.80; 6.90; 10.00; 13.10; 16.80, and (*b*) 0.67; 4.00; 7.30; 14.20; 17.53. Other parameters as for figure 25.

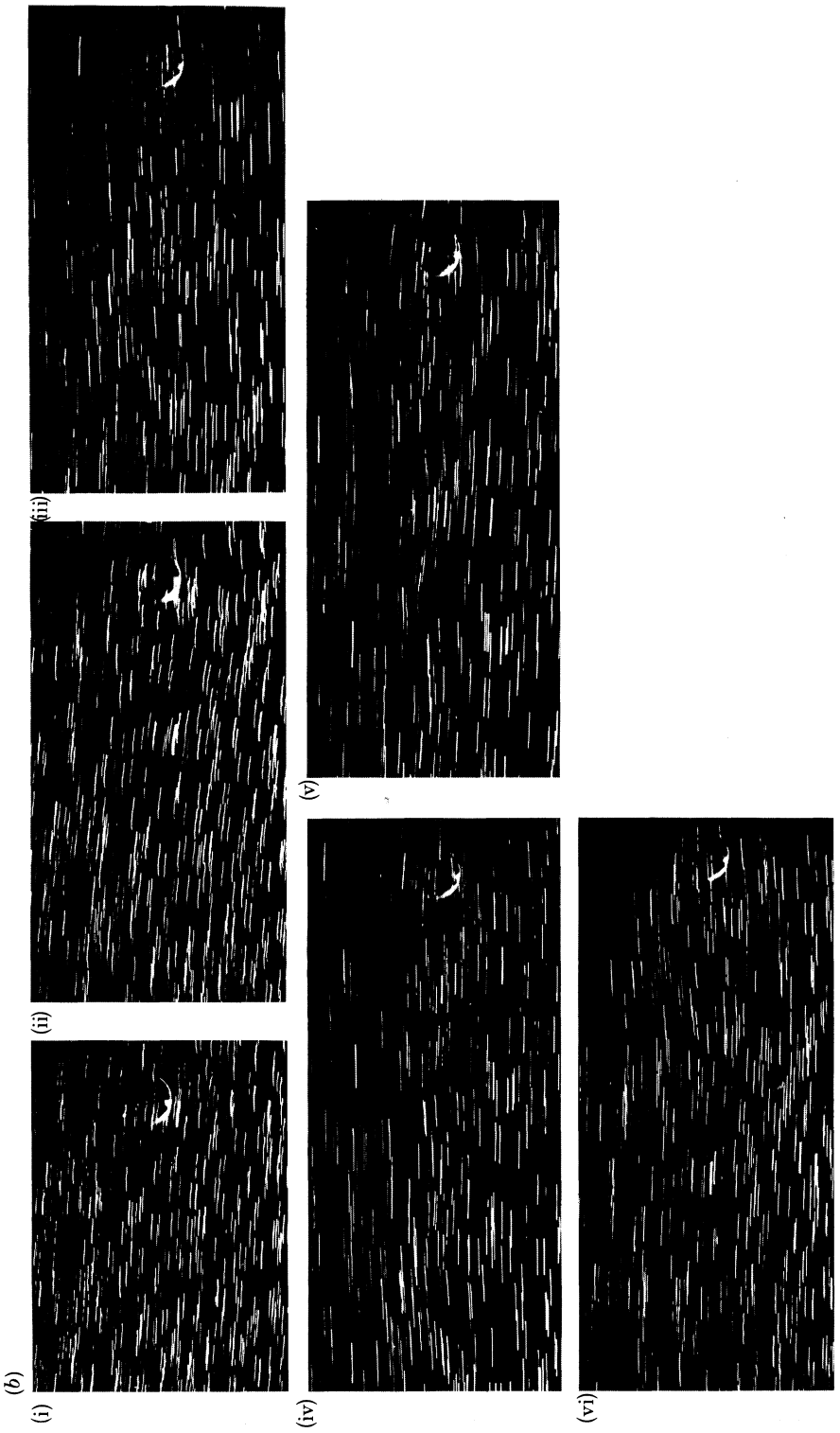

FIGURE 26*b*. For description see opposite.

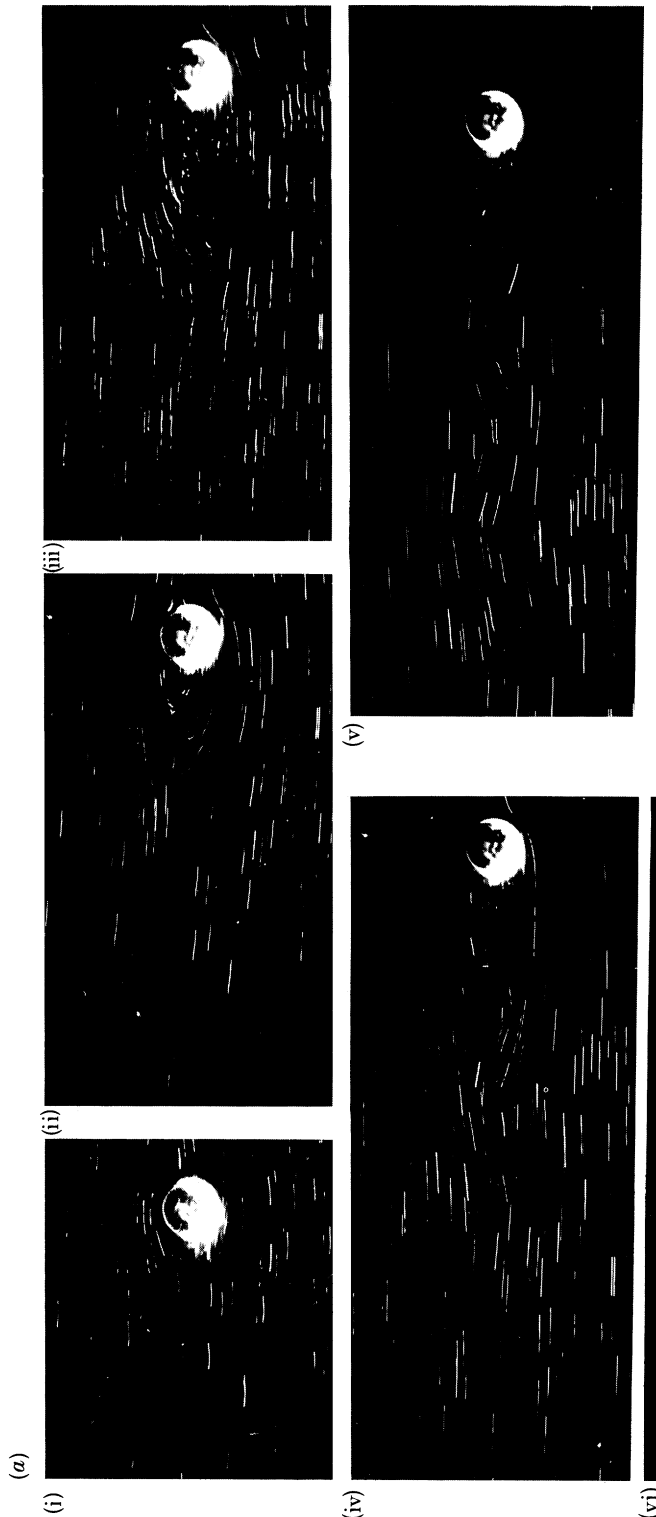

FIGURE 27. Legend as figure 26, except $t_A^* =$ (*a*) 0.80; 4.80; 8.80; 12.80; 16.60; 19.90, and (*b*) 0.88; 5.30; 9.60; 14.00; 18.60; 22.80.

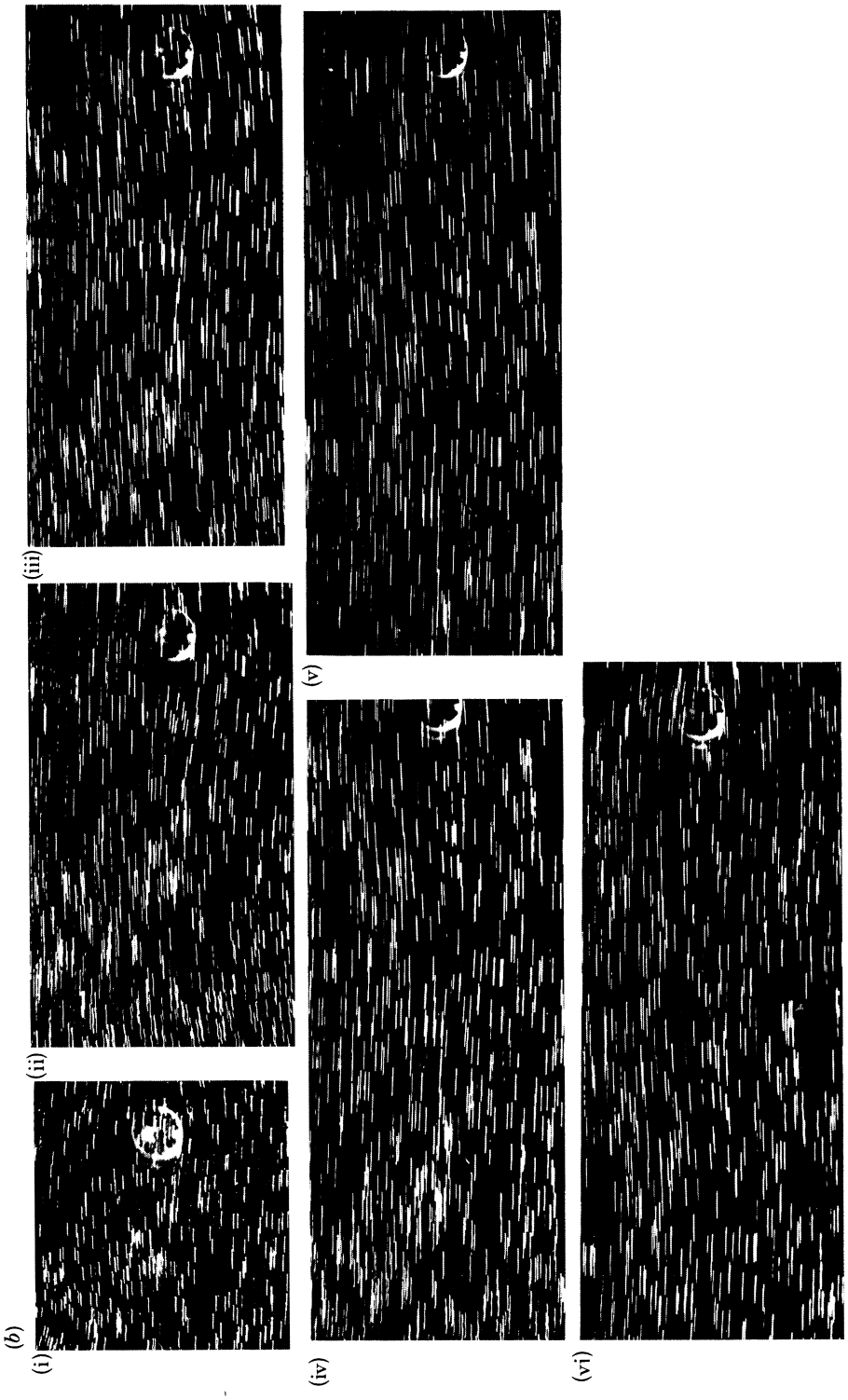

FIGURE 27 *b*. For description see opposite.

(*a*)

(*b*)

(*c*)

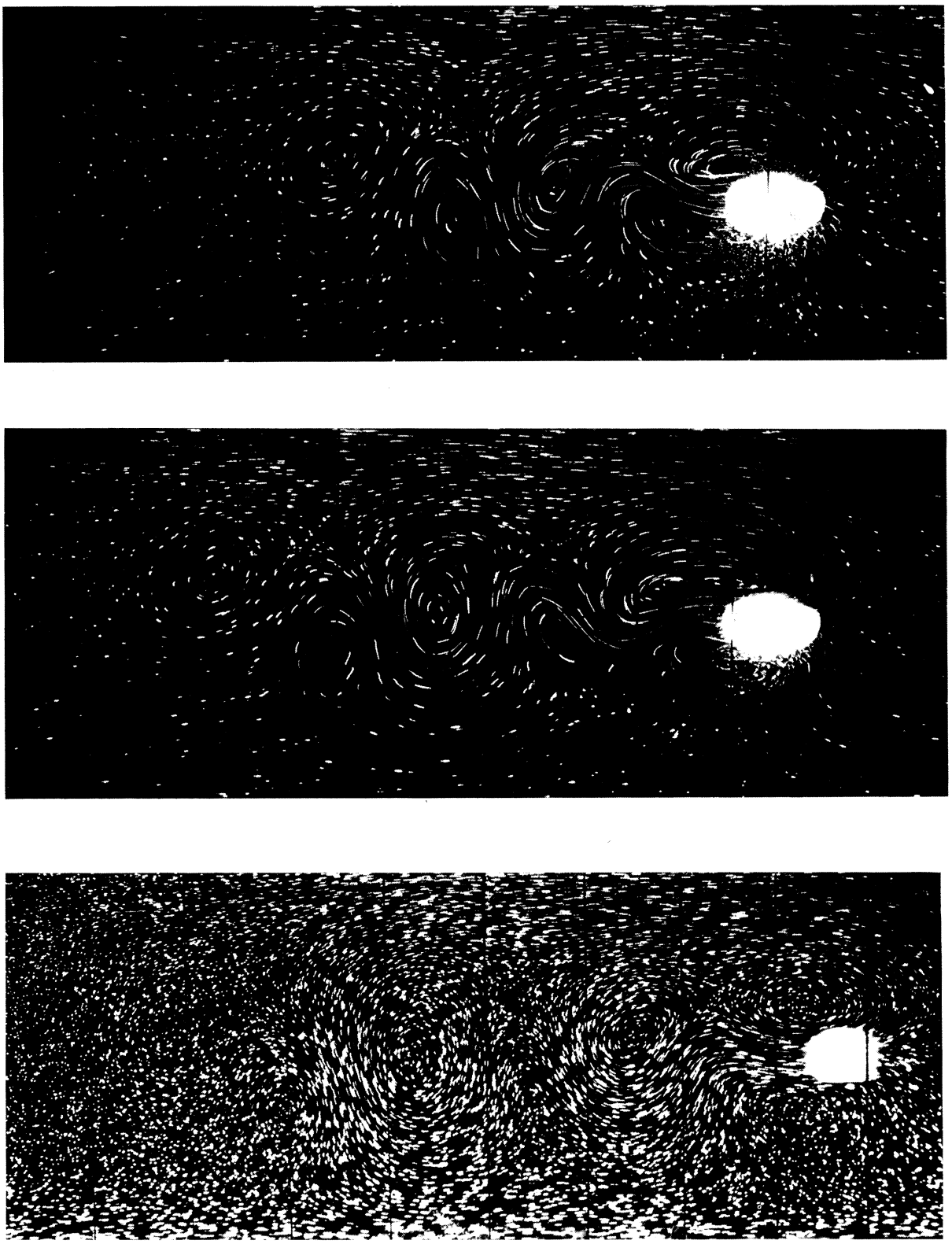

FIGURE 29. Legend as figure 25, except $Bu = 6.90$, $Ro = 0.10$ and $\{t_A^*:z^*\}$ = (*a*) {18.60:0.45}, (*b*) {21.50:0.45}, and (*c*) {24.50:0.60}.

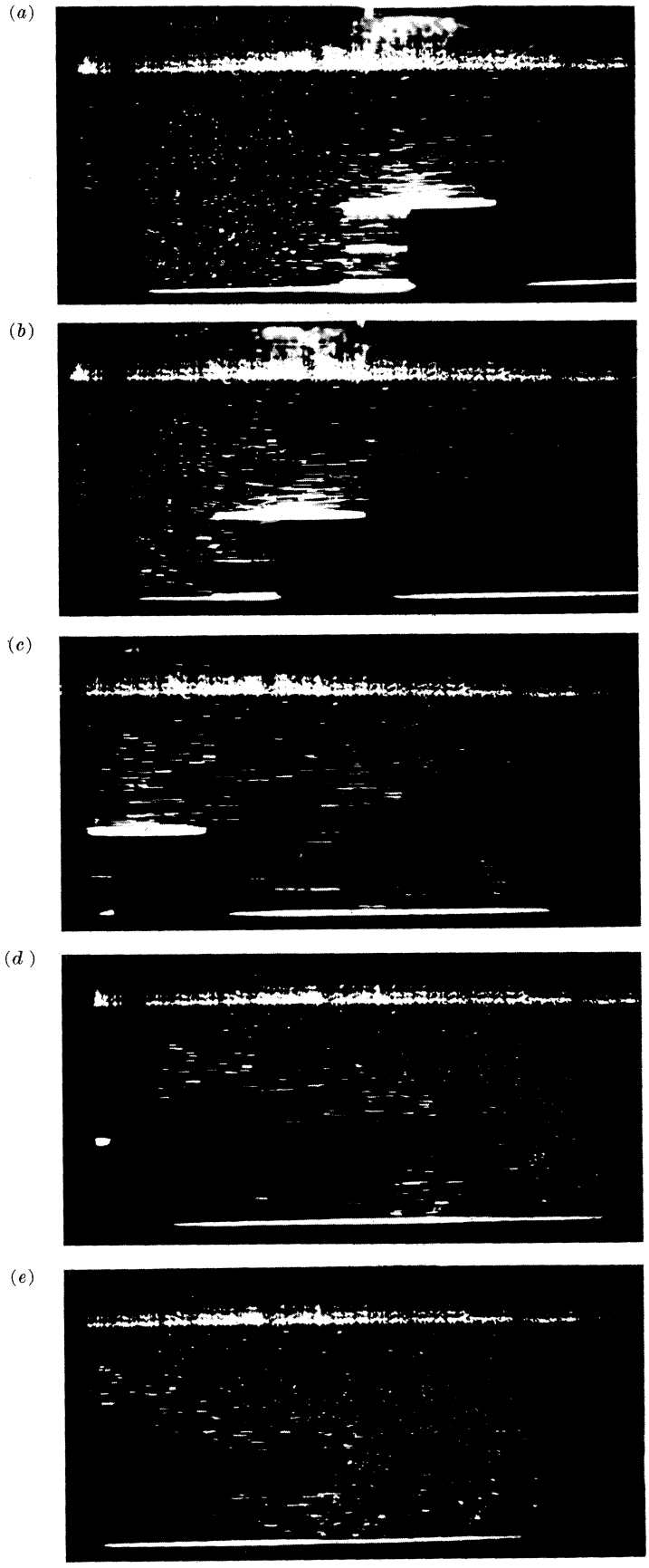

FIGURE 30. Elevation photograph time sequences for $Bu = 33.40$, $Ro = 0.076$, $h/H = 0.40$, $h/D = 1.00$, $E = 9.4 \times 10^{-5}$ and $t_A^* =$ (*a*) 13.20, (*b*) 14.10, (*c*) 14.90, (*d*) 15.80, and (*e*) = 16.60.

(*a*) (*b*)

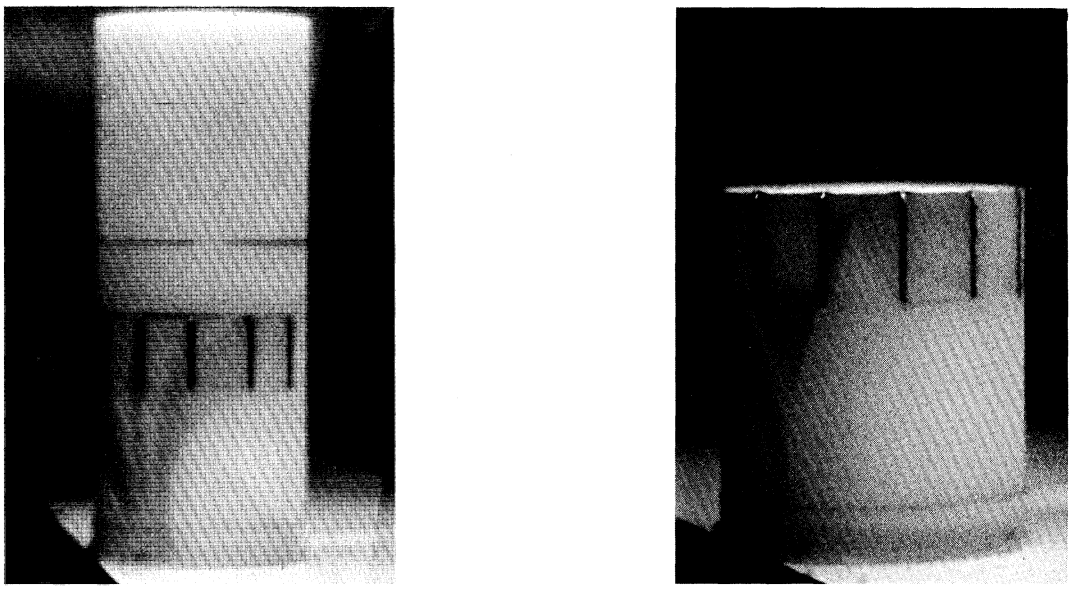

FIGURE 37. Oblique elevation dyeline photographs of shear layer patterns for $Bu = 0$, $Ro = 0.038$, $E = 9.4 \times 10^{-5}$ and $\{h/H : h/D ; t_A^*\}$ = (*a*) {1.00 : 2.50 : 6.10}, and (*b*) {0.40 : 1.00 : 10.20}. Motion of obstacle from left to right.

regard, it is noted that for the non-rotating homogeneous case the critical Reynolds number at which isolated eddies are observed is also a function of the aspect ratio (Nishioka & Sato 1974).

It can be seen from the régime diagrams above that for both cylinders the critical Reynolds number for the formation of isolated eddies is significantly larger at all Burger numbers than for corresponding non-rotating homogeneous flow past such cylinders. Such effects are known to occur (Boyer 1970; Merkine & Solan 1979; Boyer & Davies 1982) for rapidly rotating homogeneous systems ($Bu = 0$) for certain combinations of the Rossby and Ekman numbers. Five different flow régimes (fully attached, single attached eddy, asymmetrical double eddy, unsteady double eddy, and eddy shedding) were observed by Boyer (1970) as these parameters were varied. Of particular interest here is the transition to eddy shedding; if the same values of the Ekman number are compared in the studies of Boyer (1970) and the present authors, the régime diagram of the former predicts critical Rossby numbers of 0.15 and 0.60 respectively for vortex wake formation behind the large ($h/D = 2.5$) and small ($h/D = 6.25$) diameter cylinders. These values are to be compared with corresponding critical Rossby numbers of 0.08 and 0.22 for the present $Bu = 0$ results in figure 17. A number of factors contribute to these discrepancies between the two studies: firstly, the cylinder aspect ratio in Boyer's experiments was less than those in the above investigations, and, secondly, the geometrical configurations in the two studies were fundamentally different. Specifically, the flow system adopted by Boyer (1970) and Boyer & Davies (1982) consisted of a uniform flow of fluid past a stationary cylinder, in contrast to the present case where the cylinder and the bottom solid boundary were translated through a stationary fluid. As shown in §6, the structures of the boundary layers in the two systems are much different when the fluid is homogeneous, implying that the discrepancies cited above originate at least partly from these differences (see also Boyer & Kmetz 1983).

For the stratified rotating cases ($Bu \geqslant 0$), aspect ratio effects may be expected to dominate. In the non-rotating cases, it is known (Nishioka & Sato 1974) that for values of the aspect ratio h/D less than 50, decreases in the latter quantity result in dramatic increases in the critical value of the Reynolds number for vortex shedding. For the present h/D values of 2.5 and 6.25, the predicted values of the critical Reynolds numbers for vortex shedding in the non-rotating case are 260 and 100, though the former value is based on an extrapolation of the data presented by Nishioka & Sato (1974). (Note that the classical critical value of $Re = 40$ relates to vortex shedding from a cylinder having $h/D \geqslant 50$.) Inspection of the régime diagrams in figure 19 reveals that the critical values of Re for vortex wake formation in the high Burger number cases accord well with the above predicted values of Nishioka & Sato (1974). This suggests that for such cases, the control of rotation upon the flow is very weak, a finding in consonance with previous results for the transient phase (figures 16 and 17).

4.2.2. *Isolated eddy formation*

For the vortex wake régime, the periods of formation t_s of individual isolated eddies in the wake were calculated by the procedure described by Boyer *et al.* (1987), in which (i) the appearance and (ii) the motion of the eddies were followed through consecutive frames of flow visualization sequences. The formation or shedding period t_s was defined for a given array of isolated downstream vortices as

$$t_s = x_s t/s, \tag{6}$$

where s is the distance moved by a given vortex in a time t, and x_s is the spacing between the centre of this vortex and that of the consecutive vortex of the same sign. In the measurements of t_s, the spatial coordinates of the eddy centres were corrected for perspective distortion, and an interpolation procedure was developed to overcome the discontinuous nature of the data-set resulting from the photographic flow visualization sequences. A calibration curve of the eddy centre velocity U_v against the distance L_v of the centre of the eddy from the rear of the obstacle was constructed, and values of x_s could then be correlated with the velocities U_v of the eddy centres. For each value of x_s, the period t_s could then be calculated from $t_s = x_s/U_v$, and the values of t_s for each identifiable vortex were then averaged to give a representative value for all of the eddies observed in a given run. Examples showing the variation of the eddy centre velocities U_v^* with the distance L_v^* between the eddy centre and the rear of the obstacle are shown in the plots of figure 20.

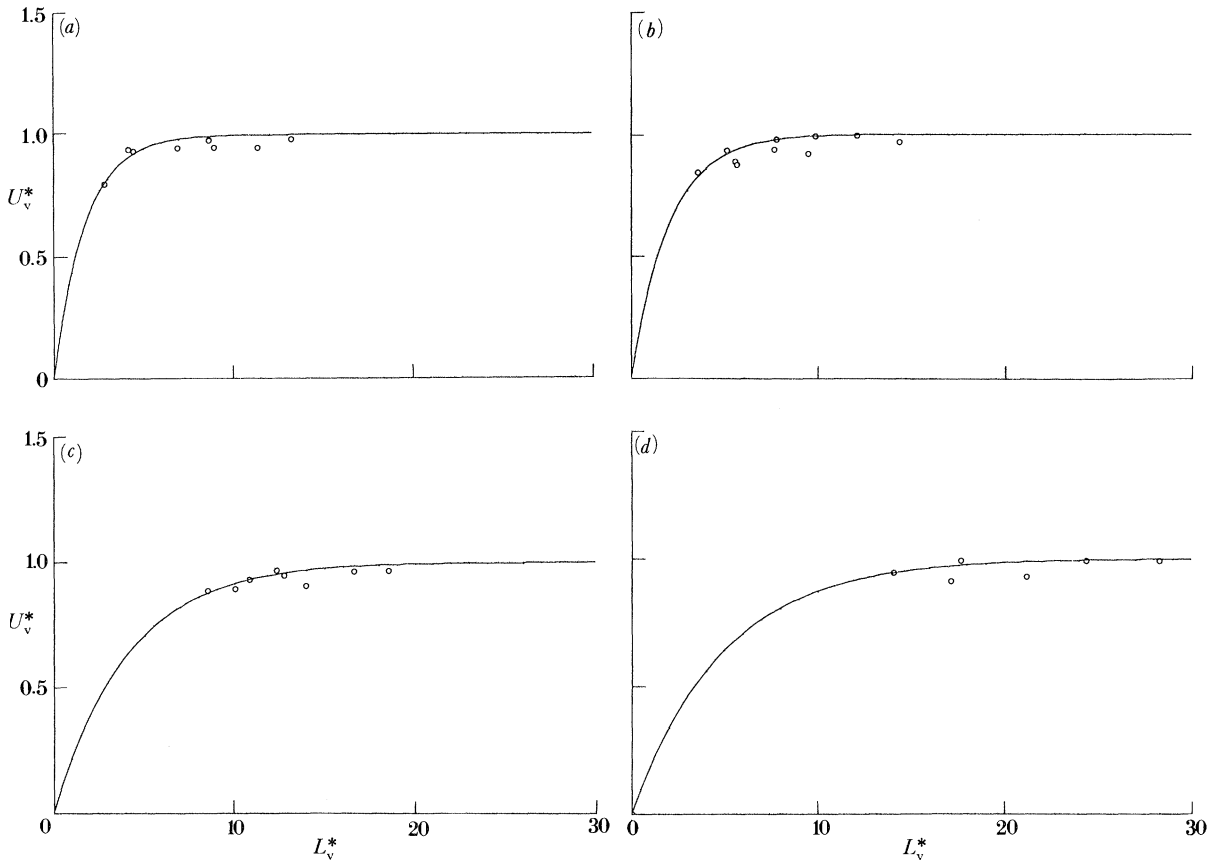

FIGURE 20. Plots of U_v^* against L_v^* for $\{Bu:Ro:H/D\}$ values (*a*) {16.30:0.20:2.5}, (*b*) {14.40:0.45:2.5}, (*c*) {16.50:0.71:6.25}, and (*d*) {122.7:0.15:6.25}. Other parameters as for figure 2. Solid curves represent best-fit exponential curves of form (1) – see text – through origin.

Dimensional plots showing the variations of t_s with U_0, h/D and Bu are shown in figure 21. Although both individual plots in figure 21 *a* and *b* display some scatter, the values of t_s in each case are seen to scale well with $1/U_0$ and to show no significant dependence upon Bu. This result is identical to that obtained earlier for the transient retention time data. The composite plot of figure 21 *c* shows the effect on t_s of the aspect ratio h/D, and it can be seen that the

smaller diameter cylinder has systematically shorter formation periods across the velocity range. It can also be seen from figure 21*c* that there is a tendency for the two sets of data to converge at higher values of $1/U_0$. This effect has been detected for similar homogeneous, non-rotating flows (Roshko 1954; Berger & Wille 1972) as a weak dependence of the Strouhal number *St* upon *Re*. For comparative purposes, the empirical relationships derived from Roshko's results for the dependence of t_s upon U_0 and d are shown for each cylinder. The good agreement between the present results and Roshko's data is shown clearly by these comparisons, indicating that the combined effects of rotation and stratification do not exert significant controls upon t_s in this parameter range.

This result is confirmed (Davis 1989) when alternative plots of the same data are made, as for the earlier retention time data. All plots show behaviour consistent with a dependence of the form

$$t_s = K_s D/U_0, \tag{7}$$

as with the corresponding eddy retention plot in figure 16.

4.2.3. *Strouhal number data*

The above t_s data are easily converted to Strouhal number data, since the latter quantity *St* is defined as

$$St = nD/U_0, \tag{8}$$

where n is the shedding frequency and, thus, $St = D/U_0 t_s$. Figure 22*a* and *b* show plots of *St* against *Ro* for the large and small diameter cylinders respectively. In both cases the data do not differ significantly (Davis 1989) from the relationship

$$St = 0.212(1-21.2/Re) \quad \text{(Roshko 1954)}$$

derived empirically from experiments conducted with non-rotating, homogeneous fluids over a Reynolds number range of 20–600, with values of $h/D > 5$. In both plots, there is significant scatter, but the trend is to larger *St* as *Ro* (and hence *Re*, for a given cylinder) is increased. In view of the apparent insensitivity of the *St* data to changes in either the stratification and/or rotation, the differences shown between figure 22*a* and *b* may be ascribed to aspect ratio effects (see also West & Apelt 1982). This is seen particularly clearly in figure 22*b* where *St* shows a weak increase with increasing *Ro* (and *Re*), an increase which is steeper than that in Roshko's non-rotating homogeneous experiments.

Other Strouhal number comparisons may be made between the present data and those of Boyer & Kmetz (1983) and Chabert d'Hieres *et al.* (1989) with rotating homogeneous flows past circular cylinders. These studies have detected slight effects of E and h/D upon *St*, though these effects are very weak.

4.2.4. *Velocity defect wake profiles*

Thus far, very few data are available on velocity profile measurements in the wake of an obstacle in a rapidly rotating fluid. Experimental studies by Maxworthy (1970) and Serotsky & Titman (1975) of longitudinal Taylor columns have included such measurements, but corresponding data on cylinder flows have not been made. In the present study, such data will be described for the flow type characterized above as attached eddy pairs. Only homogeneous fluids will be considered.

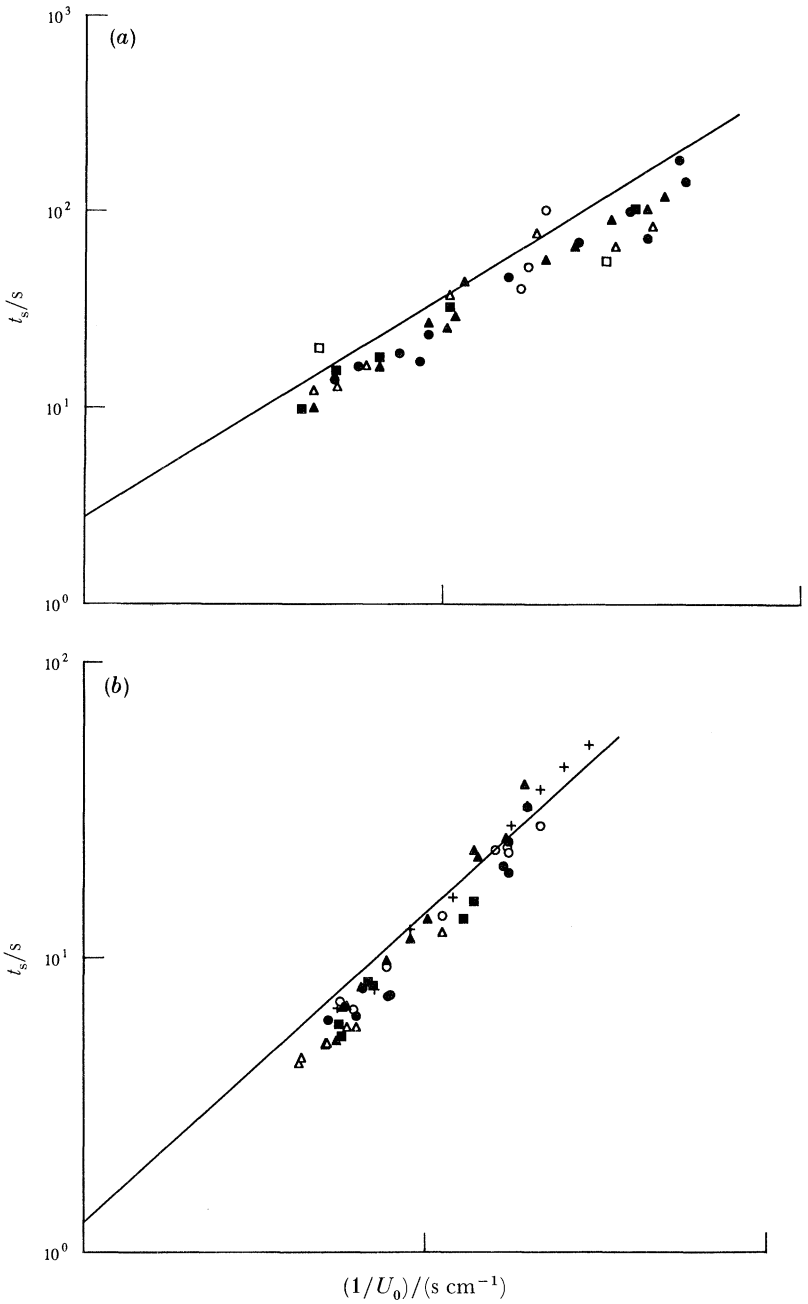

FIGURE 21 *a, b*. For description see opposite.

4.2.4.1. *Defect computations.* The velocity profiles measured at various stations downstream of the cylinder can be used to compute the momentum flux defect associated with the presence of the obstacle in the flow. By choosing a control volume containing upstream and downstream portions of the flow, and measuring the momentum flux upstream and downstream of the obstacle, the momentum flux defect within the control volume can be calculated. For cases in which the pressure is the same at upstream and downstream stations, the momentum flux defect in the undisturbed flow direction is equal to the drag force on the obstacle. However,

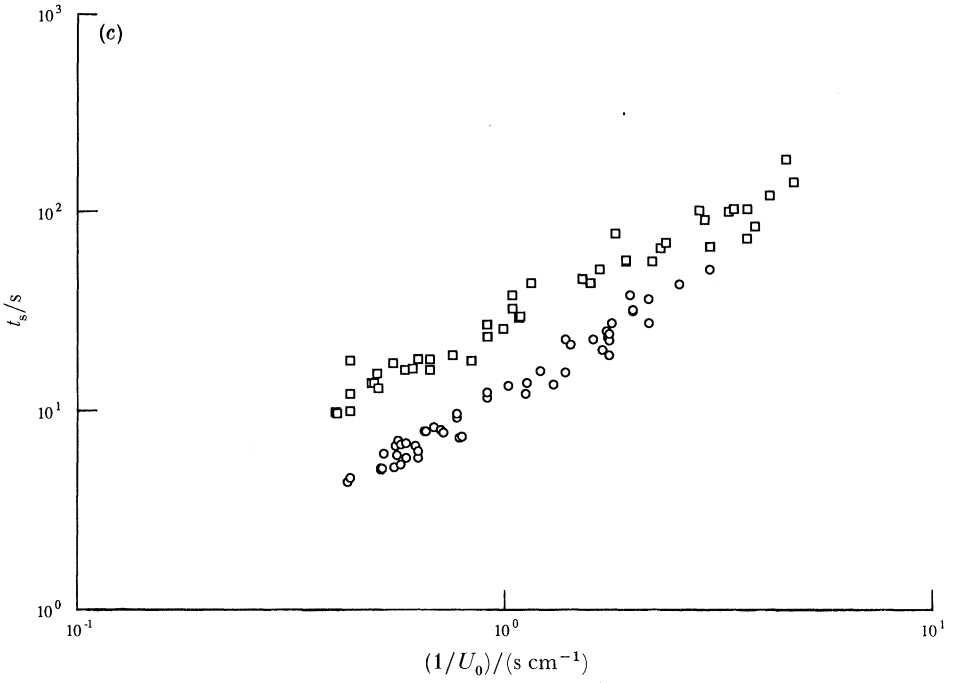

FIGURE 21. Individual plots of t_s against $1/U_0$ for H/D = (*a*) 2.50 and (*b*) 6.25 and *Bu* ranges shown, and (*c*) composite plot of t_s against $1/U_0$ for $H/D = 2.50$ (open symbols) and 6.25 (closed symbols). Other parameter values as for figure 2. Solid lines show results of Roshko (1954) for non-rotating, homogeneous flows. (*a*) □, 0; ○, 1.0–7.9; △, 8.0–12.0; ■, 12.1–15.0; ●, 15.1–20.0; ▲, 20.1–25.0. (*b*) ○, 1.0–20.0; △, 20.1–40.0; ■, 40.1–60.0; ●, 60.1–80.0; ▲, 80.1–100.0; +, 100.1–130.0.

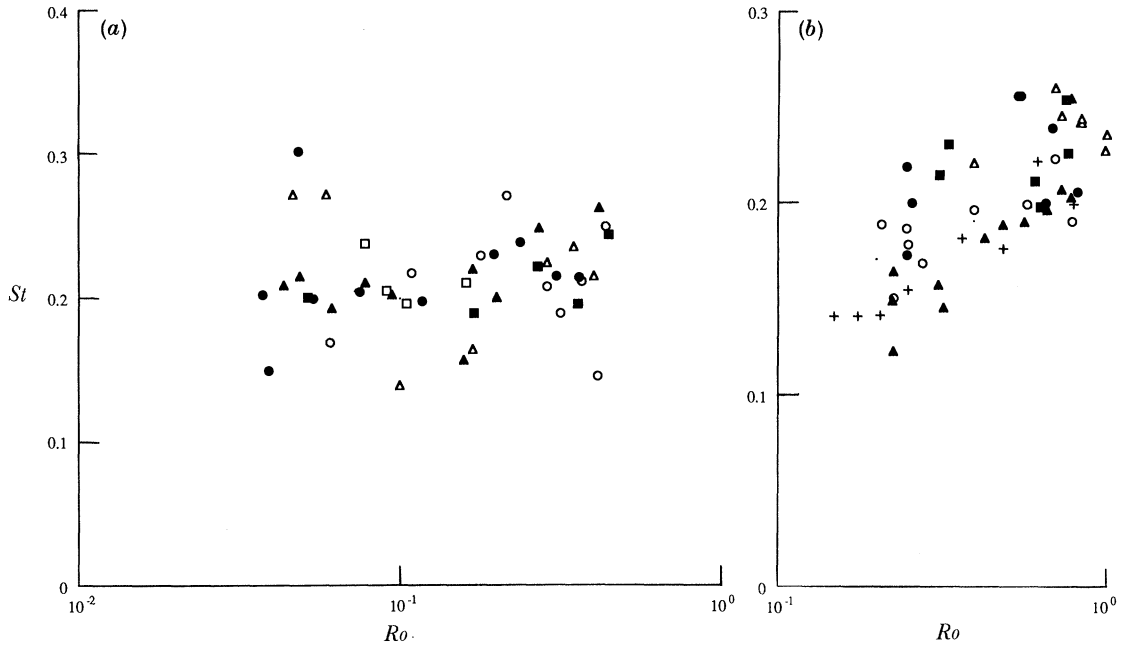

FIGURE 22. Plots of *St* against *Ro* for H/D = (*a*) 2.50, (*b*) 6.25, and *Bu* ranges shown. Other parameters as figure 2. (*a*) □, 0; ○, 1.0–7.9; △, 8.0–12.0; ■, 12.1–15.0; ●, 15.1–20.0; ▲, 20.1–25.0. (*b*) ○, 1.0–20.0; △, 20.1–40.0; ■, 40.1–60.0; ●, 60.1–80.0; ▲, 80.1–100.0; +, 100.1–130.0.

this interpretation is valid only if the upstream and downstream limits of the control volume are sufficiently far from the obstacle for (i) viscous forces at the control surface to be negligible, and (ii) the downstream streamlines to have regained their straight and parallel upstream forms (Batchelor 1970). As will be demonstrated below, the limitations in size of the present apparatus, and the time needed for the flow to achieve a steady state, both meant that the asymptotic conditions were not satisfied in the experiments. This factor precluded the use of the momentum flux defect measurements in the computation of the total drag force on the obstacle. (In recent studies by one of the authors (Chabert d'Hieres *et al.* (1990)), direct measurements have been made of the drag and lift forces on full and truncated cylindrical obstacles in rotating fluids. Such measurements extend those obtained previously truncated obstacles by Mason (1975) for very low *Ro*:*Re* flows.)

For a two-dimensional flow, the momentum flux deficit M_f is given by:

$$M_f = \rho H U_0^2 \int_{-W}^{W} \frac{u(y)}{U_0}\left[1-\frac{u(y)}{U_0}\right]dy, \tag{9}$$

where $u(y)$ is the local axial velocity component in the wake, and integration is across the width of the channel from $y = +W$ to $y = -W$. The above integral may be replaced by a summation, and the resulting expression may then be used to calculate M_f from a set of discrete measurements of $u(x, y)$ and U_0.

4.2.4.2. *Experimental techniques.* The horizontal velocity fields upstream and downstream of the obstacle were visualized at a given height (mid-depth) in the fluid using the thymol blue technique (Baker 1966). Dye was released electrochemically from horizontal wires of thickness 0.025 mm fixed in position with respect to the tank, and the displacements of dyelines in given time intervals were recorded photographically. For the upstream location and for each of the three downstream stations, velocities were measured at 60 discrete points along the dye line, and the resulting velocity profiles were transformed to the frame of reference of the moving obstacle.

4.2.4.3. *Results.* Figure 23*a* and *b* show typical velocity profiles at various distances x^* ($=x/D$) downstream of the rear of the obstacle and for various values of *Ro*. The maximum velocity defect at a given value of x^* is seen to increase with increasing *Ro*, and some evidence of asymmetry in the velocity profiles is shown in the near field data. (It should be noted that for the lowest values of *Ro*, the distances moved by the dye lines in intervals of 30 s were sometimes so small as to be close to the resolution limit of the photographic negatives. Attempts to improve the resolution by increasing the interval over which the dye line distortions were measured foundered because dye diffusion effects then became significant. Such problems are responsible for the relatively poor resolution at low values of *Ro* and at stations far from the obstacle.)

The momentum flux defect M_f for each of the measured velocity profiles were computed using the summation derived from expression (9) in §4.2.4.1. For all stations, the values of M_f are seen to increase monotonically with increasing *Ro*, with a form which implies that for a given full depth cylinder and a given fluid:

$$M_f = A(Ro)^n. \tag{10}$$

Measurements indicate that the index n takes a typical value of about 3.3.

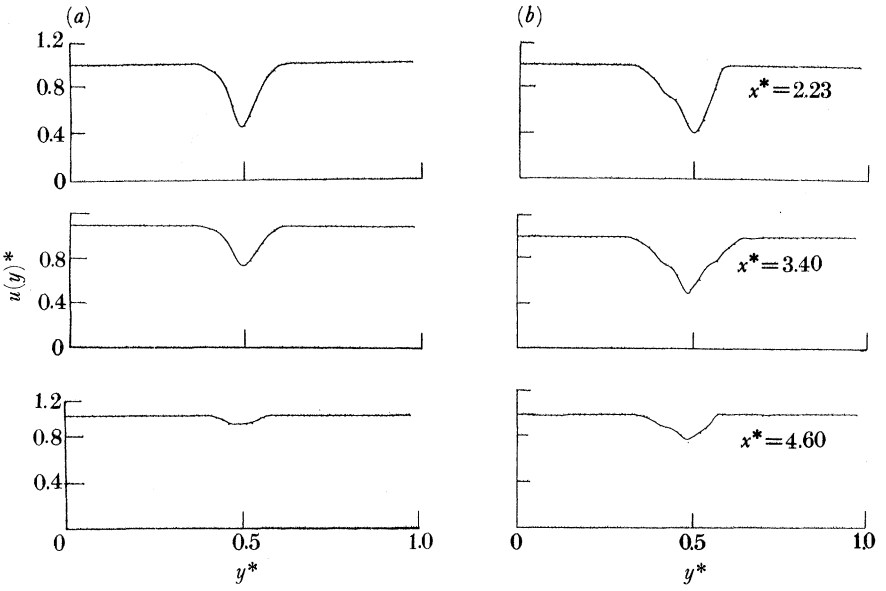

FIGURE 23. Mid-depth ($z^* = 0.5$) wake profiles $u(y)^*$ for x^* values shown and $\{Bu{:}Ro\}$ = (*a*) {0:0.031}, (*b*) {0:0.040}. Other parameters as figure 2.

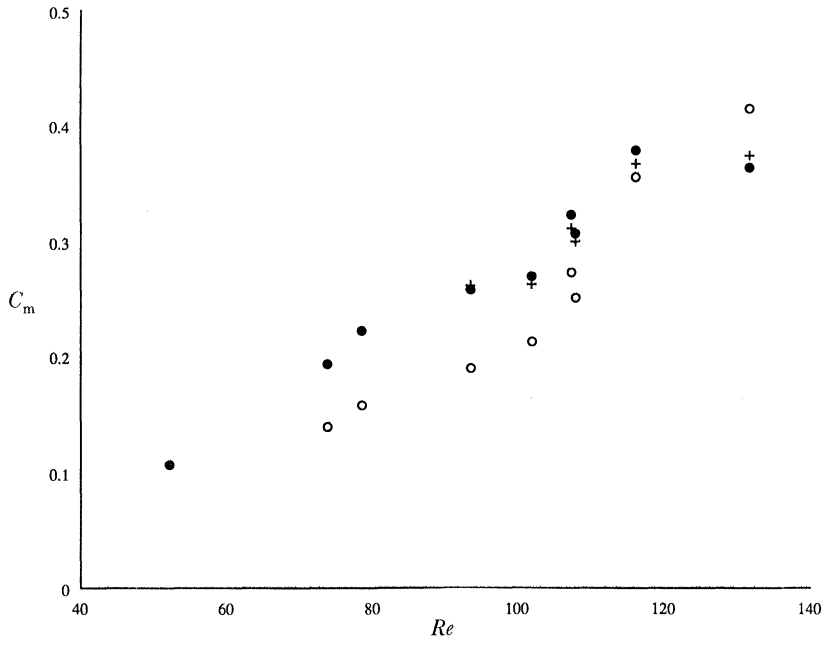

FIGURE 24. Composite plot of C_m against Re, for $Bu = 0$, $E = 9.4 \times 10^{-5}$, $H/D = 2.50$, $h/H = 1.0$, and x^* values shown. ●, $x^* = 2.23$; ○, $x^* = 3.40$; +, $x^* = 4.60$.

To facilitate more general comparisons with velocity defect measurements from non-rotating fluid experiments, the data are replotted in dimensionless form in figure 24 in terms of a momentum flux coefficient C_m against Re. Here C_m is defined in the usual way as

$$C_m = 2M_f/\rho_0 U_0^2 Dh. \tag{11}$$

The replotted data show that, within the experimental uncertainty limits, the values of C_m

increase with increasing Reynolds number in the fully attached eddy pair régime. The nature of the increase suggests a power law dependence of the form postulated for the M_f against Ro data. Note that the C_m values are significantly less than typical drag coefficients to be expected for the same Reynolds number range in either rotating (Chabert d'Hieres *et al.* 1989) or non-rotating (Tritton 1988) cases. These discrepancies offer further evidence that the pressure difference between the ends of the control volume used in the derivation of M_f were still significant for stations as far downstream as $x^* = 4.6$.

5. Results: truncated cylinder

In the case of the truncated cylinder, fluid is no longer forced to go around the solid obstacle, but is also able to pass over it and to generate three-dimensional motions within the flow. Thus the particular objectives of the present truncated cylinder experiments were (i) to determine the effects of these geometrical changes upon the typical full cylinder flow types described above, and (ii) to investigate the vertical coherence of downstream flow disturbances generated at levels below the top of the truncated cylinders. To this end, measurements were made at various depths in the fluid, for transient and fully developed flows.

5.1. *Transient flow*

5.1.1. *Qualitative observations*

Figure 25*a*, *b* and *c*, plates 9–11, show three sequences of the low-level transient flow development for the three typical flow types observed for the truncated cylinders. It can be seen clearly that these flow types resemble very closely those described previously for the full cylinder case. Indeed, for this level (mid-obstacle height), the fully developed flows, and their transient development, are not only identical with those of the full cylinder, but they also show the same very weak dependence upon changes in the Burger number. As with the full cylinder cases, the only noticeable effect of increasing the Burger number is to increase slightly the width of the wake region. The flow structure in the deep levels is not affected significantly by the upper level flow over the obstacle.

To show the degree of vertical propagation of the disturbances generated by the obstacle's motion, a number of sequences were obtained for $z^* = 0.43$ and 0.52. (Note, the level $z^* = 0.4$ corresponds to the top of the truncated cylinder.)

Figures 26 and 27, plates 12–15, show the vertical attenuation of transient disturbances generated in the lower levels of the fluid for the attached eddy pair and vortex wake types of flow respectively. In figure 26*a* the attached eddies at the rear of the cylinder are still shown clearly, but at an observation level well above the obstacle top (figure 26*b*) the perturbation to the downstream flow is very weak throughout the transient phase. It is only in the later stages of development that the flow at this upper level is perturbed, with the disturbance taking the form of a slight divergence of the flow immediately above the obstacle. Similarly, in figure 27*a*, the perturbation produced just above the top of the cylinder by the formation of isolated vortices in the lower levels takes the form of an undulation in the wake region, with deflection of the flow directly above the top of the obstacle. Figure 27*b* shows that both of these features are attenuated strongly in the vertical direction.

5.1.2. *Eddy retention time*

Using the same procedure as for the full cylinder experiments, measurements of starting eddy retention times have been made over a wide range of values of Ro and Bu. These measurements are presented in figure 28*a–d*, in the forms suggested by the earlier plots with the full cylinders. For example, figure 28*a* (4.24) shows that the data may be represented well by a linear relation between $\ln[(t_r)_N^*]$ and $\ln(Fr)$, with this relation being independent of the value of the Burger number. The comparative plots in figure 28*b*, *c* and *d* show that the trends of the truncated cylinder data are qualitatively the same as for the corresponding full cylinder cases. In the latter cases, the dimensional retention times were shown to scale with U_0 and D, but little dependence upon the background rotation and stratification could be detected. Thus far, the truncated cylinder data have agreed qualitatively with such findings (figure 28*a*), and in the first of the composite plots the proposed D/U_0 scaling is tested directly. Figure 28*b* shows that the truncated data are not significantly different in their behaviour from their full cylinder counterparts. However, figure 28*c* shows a clear differentiation between the full and truncated cylinder data, with the latter having significantly longer retention times t_N^* for a given value of Fr. Such a result implies that t_N is affected by three-dimensional flow perturbations over the truncated cylinder, or by differences in h/D and/or h/H. In the final comparative plot (figure 28*d*), the differentiation is absent; here, the data for the two cylinders having the same diameters ($h/H = 1.0$ and 2.5 respectively) do not show significant differences, while the smaller of the two full cylinders shows significantly higher values $(t_r)_\Omega^*$ for a given Rossby number. On the evidence of the distribution of data points in figure 28*c* and *d* it may be concluded that the dispersion here is due to differences in the values of h/H between full and truncated cylinders, since h/H appears in the plotted parameters in figure 28*c* only. The further evidence of figure 28*d* (in which the data points group according to obstacle diameter) and figure 28*b* (where they do not) suggests that the retention times are determined principally by D, U_0 and h/H, and not by either N or Ω.

In studies of rotating stratified flow over and around three-dimensional obstacles such as cones and cosine-squared topographies, Boyer *et al.* (1987) found an empirical relationship $t_r \approx 10\, D/U_0$ for a single non-rotating stratified case, while for a similar rotating stratified case they observed that t_r tuned to the inertial period $2\pi/\Omega$ and not the advective time D/U_0. As indicated above, no such behaviour was observed in the present study.

5.1.3. *Steady-state flow*

5.1.3.1. *Flow structures.* The sequence shown in figure 26*a* indicates that the flow in the final stages is asymmetrical, with the cyclonic attached eddy appearing to be stronger than its anticyclonic counterpart. This aspect of the flow was observed at all levels for a fixed Rossby number across the full range of Burger numbers, and at various Rossby numbers when the value of the Burger number was held constant. In some cases the anticyclonic attached eddy did not penetrate into the higher levels of the fluid. For the limiting case of $Bu = 0$, flow visualization with Mearle particles showed evidence of strong anticyclonic deflection of the flow above the obstacle, as a result of Taylor column formation there (Boyer *et al.* 1984*a*), in contrast to the rotating stratified cases where the flow over the obstacle is only weakly deflected. Further evidence of eddy asymmetry below and just above the top of the obstacle was also obtained for the flow type categorized as transitional, but for vortex wake flows shed

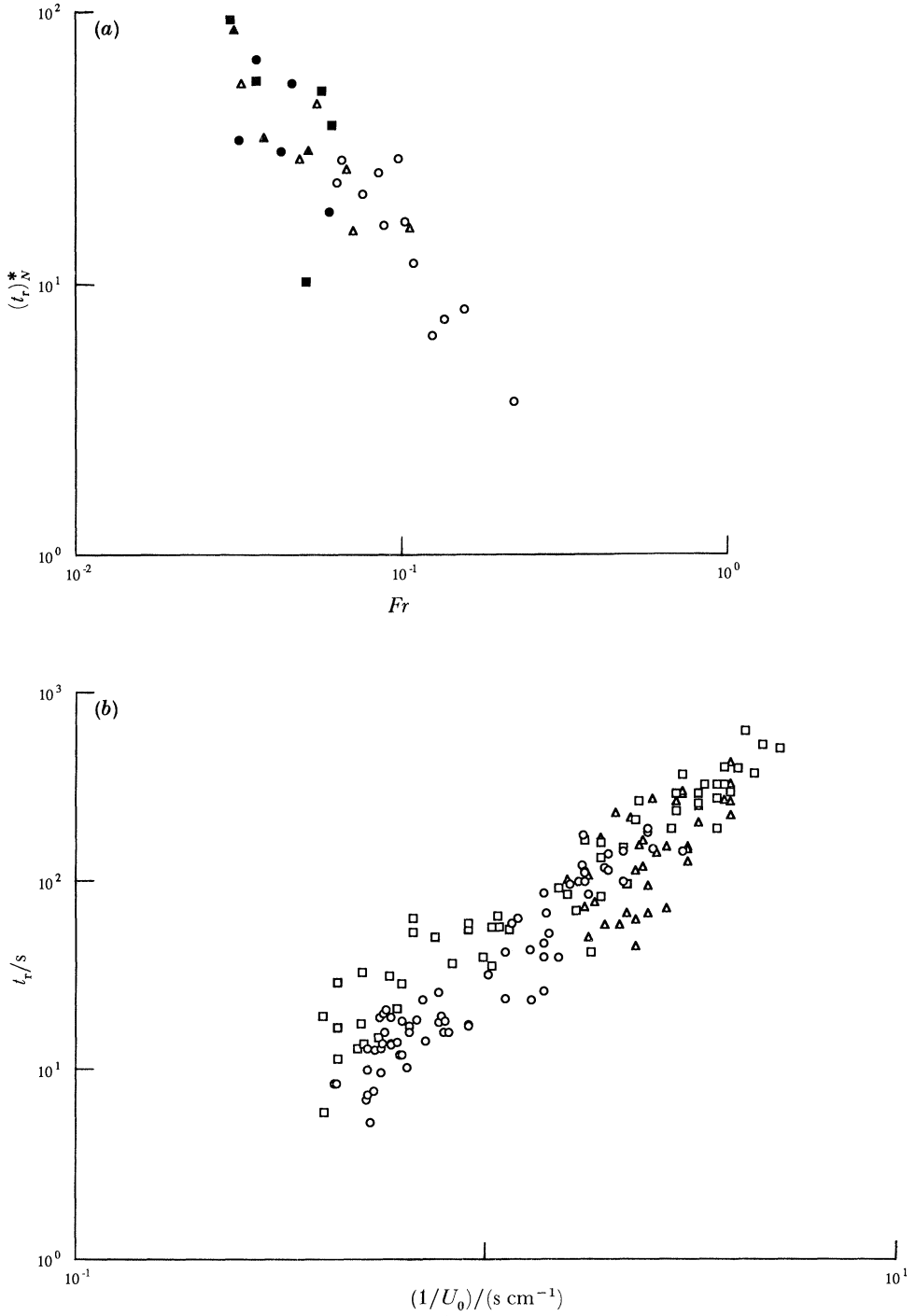

FIGURE 28*a*, *b*. For description see opposite.

anticyclones and cyclones had very similar structures. The asymmetry discussed for the other flows in this section was now absent at levels just above the obstacle summit and at higher levels in the fluid (see figure 29, plate 16). The photographs shown in the latter figure illustrate that the structures of the isolated downstream vortices are coherent throughout the affected depth of fluid, but the circulation within any one of the eddies diminishes with height above the

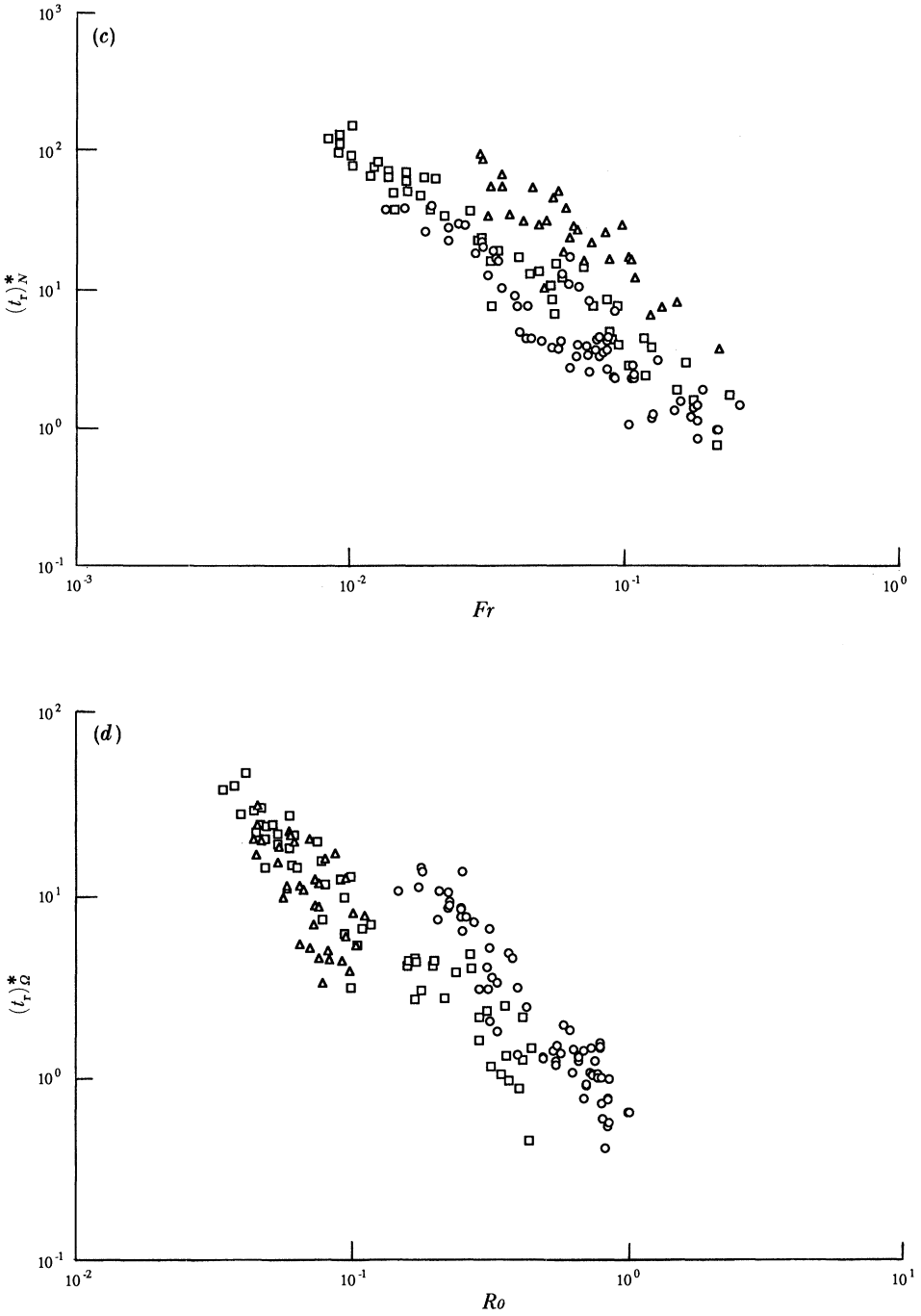

FIGURE 28. (*a*) Plot of t_N^* against Fr for $h/H = 0.40$, $h/D = 1.0$ and Bu values shown, and composite plots for all Bu of (*b*) t_r against $1/U_0$, (*c*) t_N^* against Fr, and (*d*) t_Ω^* against Ro. In (*b*), (*c*) and (*d*) $\{h/D : h/H\}$ values are $\{1.00 : 0.40\}$, $\{2.50 : 1.00\}$ and $\{6.25 : 1.00\}$. In all plots, $E = 9.4 \times 10^{-5}$. (*a*) ○, 0.5–7.9; △, 8.0–12.0; ■, 12.1–15.0; ●, 15.1–20.0; ▲, 20.1–25.0.

obstacle. At any given value of the Burger number, it is possible to find a level in the fluid where the isolated vortices do not penetrate and above which the flow is undisturbed. Figure 30, plate 17, shows a region of strong flow over and in the immediate vicinity of the rear of the obstacle. Just outside the near wake, there are regions of strong flow separated by relatively undisturbed regions, with the individual isolated vortices formed at the rear of the obstacle being separated from the narrow, apparently stagnant regions where the flow is normal to the plane of illumination. As in figure 29, the flow within the eddies is seen to be coherent in the vertical direction, and the disturbed wake region is seen to extend to a level above which the free stream flow remains undisturbed.

A quantitative measure of the location of the level z_v^* of undisturbed downstream flow was estimated by measuring the displacements of tracer particles from images such as those in figure 30. Figure 31 shows a plot of z_v^* against *Bu* for a range of *Ro* values. The plot illustrates that for weakly stratified cases, increases in *Bu* result in sharp decreases of z_v^*, but as *Bu* increases the isolated wake vortices extend to a constant level approximately 0.1 times the fluid depth above the obstacle top.

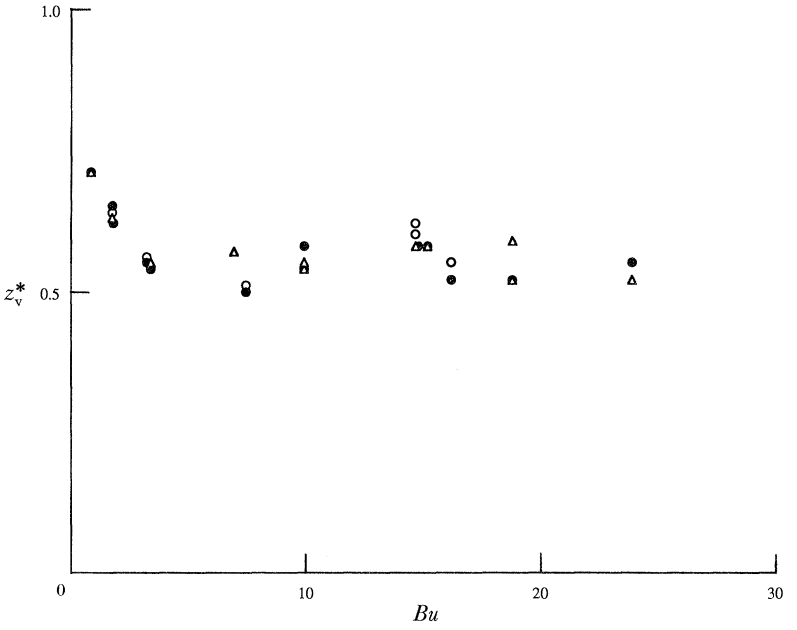

FIGURE 31. Plot of z_v^* against *Bu* for *Ro* ranges shown. ○, 0.040–0.060; ●, 0.061–0.080; △, 0.081–0.10. Other parameters as figure 30.

5.1.3.2. *Régime diagrams.* Figure 32*a* and *b* summarize the fully developed flow regimes for the truncated cylinder, with figure 32*a* being shown in the same form as for the earlier figure 19*a* and *b*. The data show that the critical Rossby number for the formation of isolated wake vortices does not vary significantly with the Burger number between values of the latter between 3 and 15. For higher values of the Burger number, the critical Rossby number is seen to increase with increasing Burger number, while for very low values of *Bu* (less than about 3), the critical Rossby numbers increase with decreasing *Bu*. (The latter tendency was also observed for the full cylinder cases, where it was ascribed to the increasing effects of stratification on the cylinder shear layer structure as *Bu* increases from zero.) Figure 32*b* shows

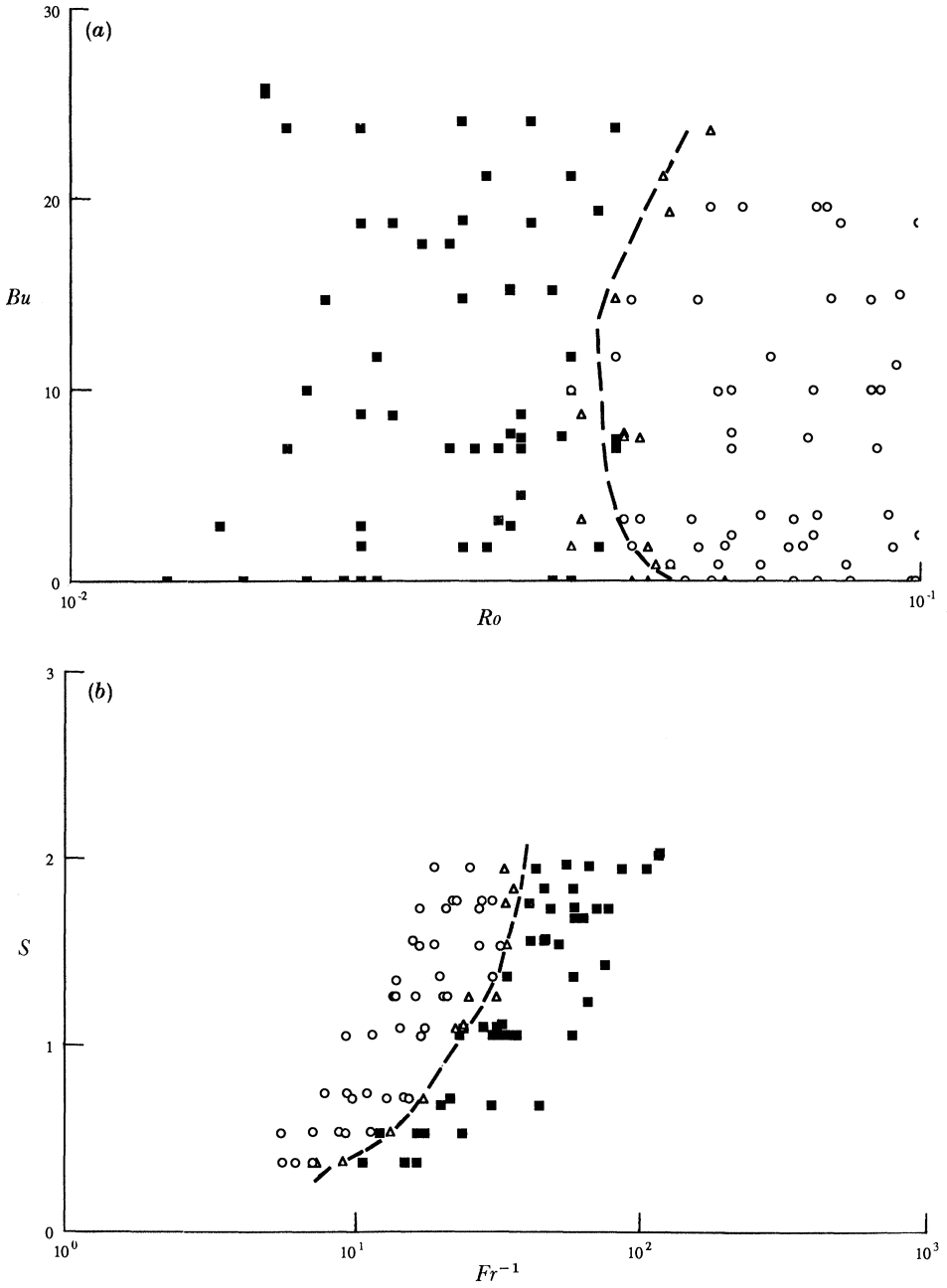

FIGURE 32. Régime diagrams (*a*) *Bu* against *Ro*, and (*b*) *S* against Fr^{-1}, for parameter values of figure 30. Flow types as for figure 18.

that the critical inverse Froude number for the formation of isolated vortices varies strongly with $S(=N/2\Omega)$, with the critical value increasing with increasing S.

The régime diagram data for the truncated cylinder may be compared with those for the two full-depth cylinders, as shown by figure 33*a* and *b*. Here, only the transitional flow data have been plotted for all three cylinders, to identify more clearly the border between attached eddy pair and wake vortex flows. Figure 33*a* confirms that at low values of *Bu* the increase in the critical value of *Ro* with decreasing *Bu* is a common feature of all the cylinders, and shows that

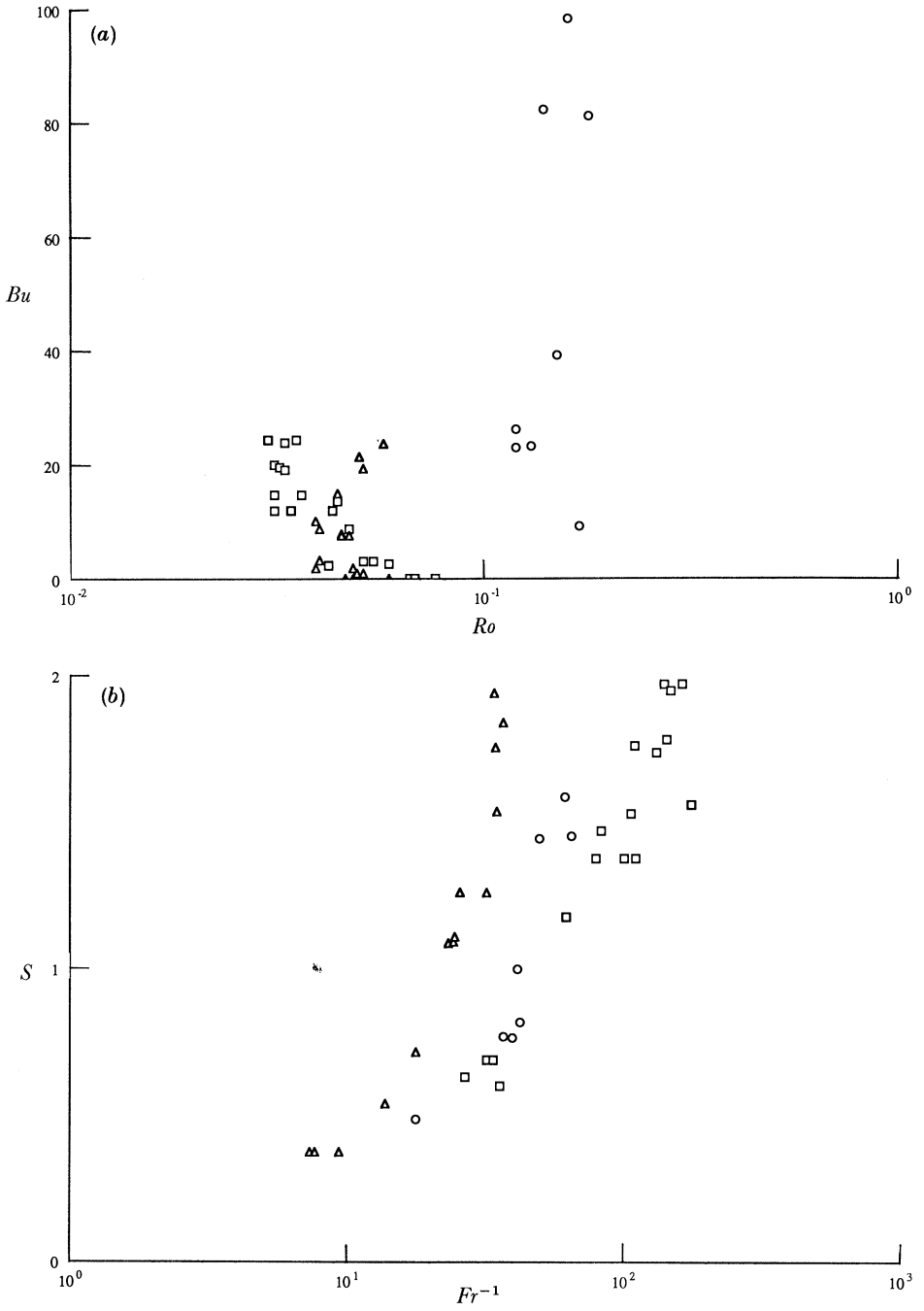

FIGURE 33. Transition data plotted as in figure 32, in composite form with $\{h/D:h/H\}$ values = (*a*) {2.50:1.0}, (*b*) {1.00:0.40}, and (*c*) {6.25:1.00}.

the data for the full cylinder having $h/D = 2.5$ and the truncated cylinder behave very similarly for values of Bu less than about 15. Since these cylinders have the same diameter, the above results indicate that the differences between these cylinders and the cylinder having $h/D = 6.25$ are due to aspect ratio effects, and that effects of flow over the truncated cylinder are not dynamically important with respect to the critical value of Ro required for vortex wake formation.

At higher values of Bu, the transitional régime boundary for the truncated cylinder takes a different form from those of the full cylinders, implying that either h/H differences or the associated effects of weakening vertical coherence of the flow above and downstream of the truncated cylinder at higher Bu, are of importance. These effects are seen well in figure 33*b* where the same data are re-plotted in terms of the inverse Froude number and the parameter S. In this case, the inclusion of the factor h in differences between values of Fr for full and truncated cylinders, results in the clear separation of the truncated cylinder boundary from those of the full depth cylinders throughout the range of S. The increase in separation at higher values of S illustrates again the effects seen at high values of Bu in figure 33*a*.

5.1.3.3. *Eddy formation periods.* Values of the times t_s for the formation of isolated vortices downstream of the truncated cylinders are shown in figure 34, together with corresponding data from the full cylinder experiments (see §4.2.2 above). (Preliminary plots with the truncated cylinder data showed no significant dependence of t_s upon Bu, so figure 34 includes all Bu values in undiscriminated form.) It has already been established that t_s scales primarily with D/U_0 for the full cylinder case, and figure 34 shows that this conclusion is also valid for the truncated cylinders. Specifically, figure 34*a* shows (i) the same linear relationship between t_s and $1/U_0$ for truncated and full cylinders having the same diameter, and (ii) a separation of data points according to obstacle diameter. Furthermore, figure 34*b*, in which $(t_s)^*_\Omega$ is plotted against Ro, shows a collapse of the data points for all cylinders to the same $1/Ro$ relationship. The data from both figures confirm the same d/U_0 scaling for t_s as for the starting eddy retention times and the vortex formation times in §§4.1.3, 4.2.2 and 5.1.2.

5.1.3.4. *Vertical attenuation.* In figures 30 and 31 attention was focused upon the influence of density stratification on the vertical coherence of the downstream eddies. In this section, the structure of the Taylor column above the truncated cylinder is considered, and measurements are presented on the influence of the background stratification upon the vertical extent of the column.

The strength of the Taylor column at a given height z^* above the top of the cylinder was quantified in terms of the horizontal free stream components of velocity $u^*(z^*_h)$ at a level z_h above the top of the obstacle at mid-obstacle location (see figure 30). It is known from previous studies that incident streamlines are deflected vertically and horizontally within the Taylor column, with the degree of curvature of the streamlines being determined by the values of z^*_h, Ro, Bu, and E (see Hide & Ibbetson 1966; Davies 1972; Boyer *et al.* 1984*a*). Thus the following one-dimensional velocity measurements do not represent completely the horizontal flow structure at a given level. However, previous investigations (Davies 1972; Davies & Rahm 1982; Spence 1986) have illustrated that such measurements characterize well the strength of the obstacle-induced disturbance at a particular level above the obstacle.

Photographs such as figure 30 were used to make measurements of the lengths of suspended particle traces for given exposure times, at distances greater than one quarter of the obstacle diameter from the leading edge. The velocity profiles were found to vary by only a few percent at locations between a quarter of an obstacle diameter from the leading edge and within the remaining portion of the region disturbed by the obstacle.

Comparisons were made between the profiles by fitting the data empirically to curves of the form

$$\ln(u^*(z^*_h)) = B_1 \ln(z^*_h) + \ln(I), \tag{12}$$

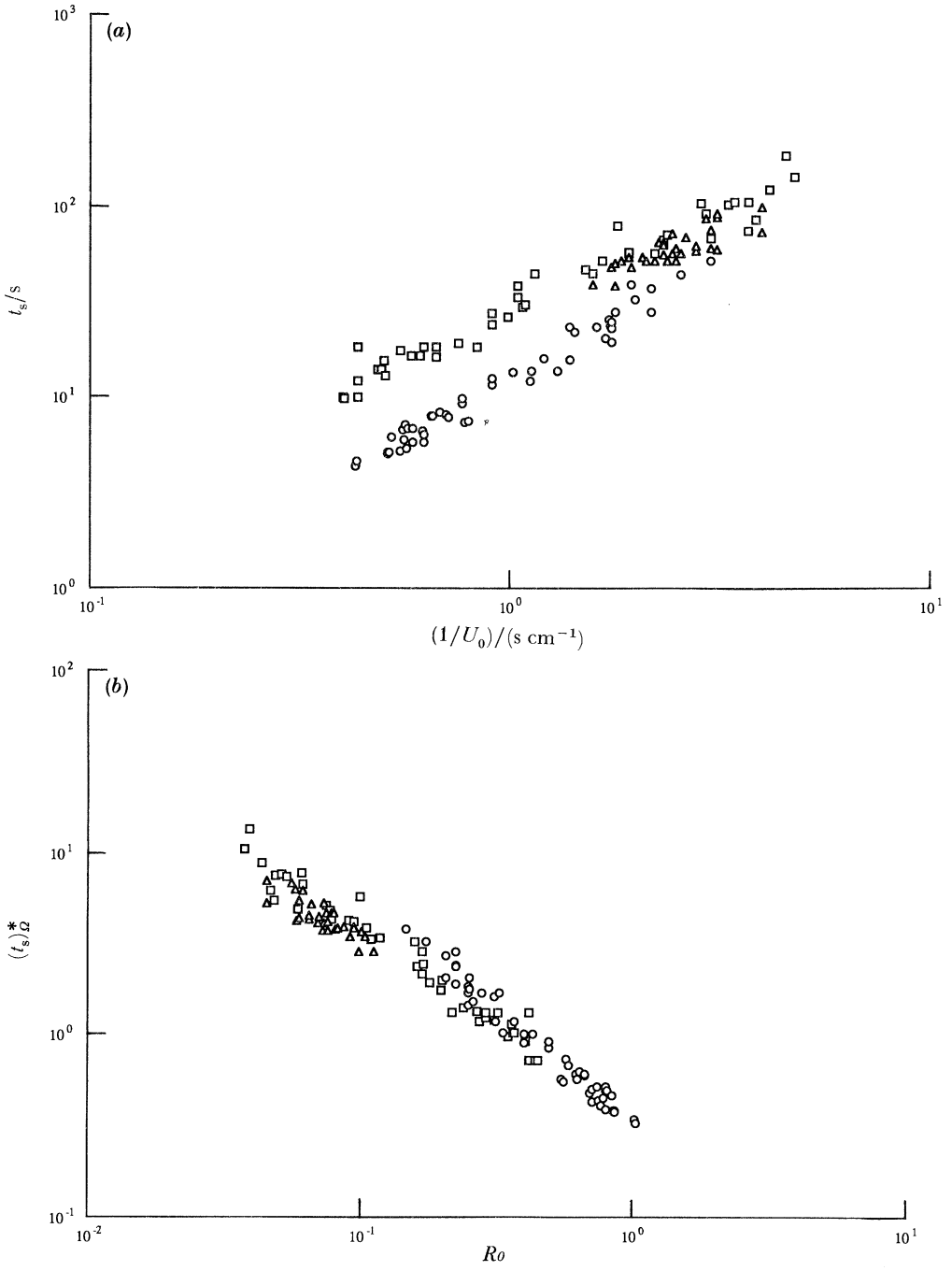

FIGURE 34. Composite plots of (*a*) t_s against $1/U_0$, and (*b*) $(t_s)^*_\Omega$ against Ro. Other parameters and symbols as in figure 33.

where $u^*(z^*_h) = u(z_h)/U_0$ is the dimensionless horizontal velocity component and $z^*_h = z/(H-h)$ is the dimensionless vertical distance measured from the top of the obstacle ($z = h$). For each photographic negative, a minimum of 10 measured data points were processed, and for each *Ro*–*Bu* pair three negatives were used. For all values of *Ro* and *Bu*, measurements were made at the same scaled elapsed time of $t^*_A = tD/U_0 = 14.5 \pm 1.2$ and at consecutive intervals separated by two advective timescales.

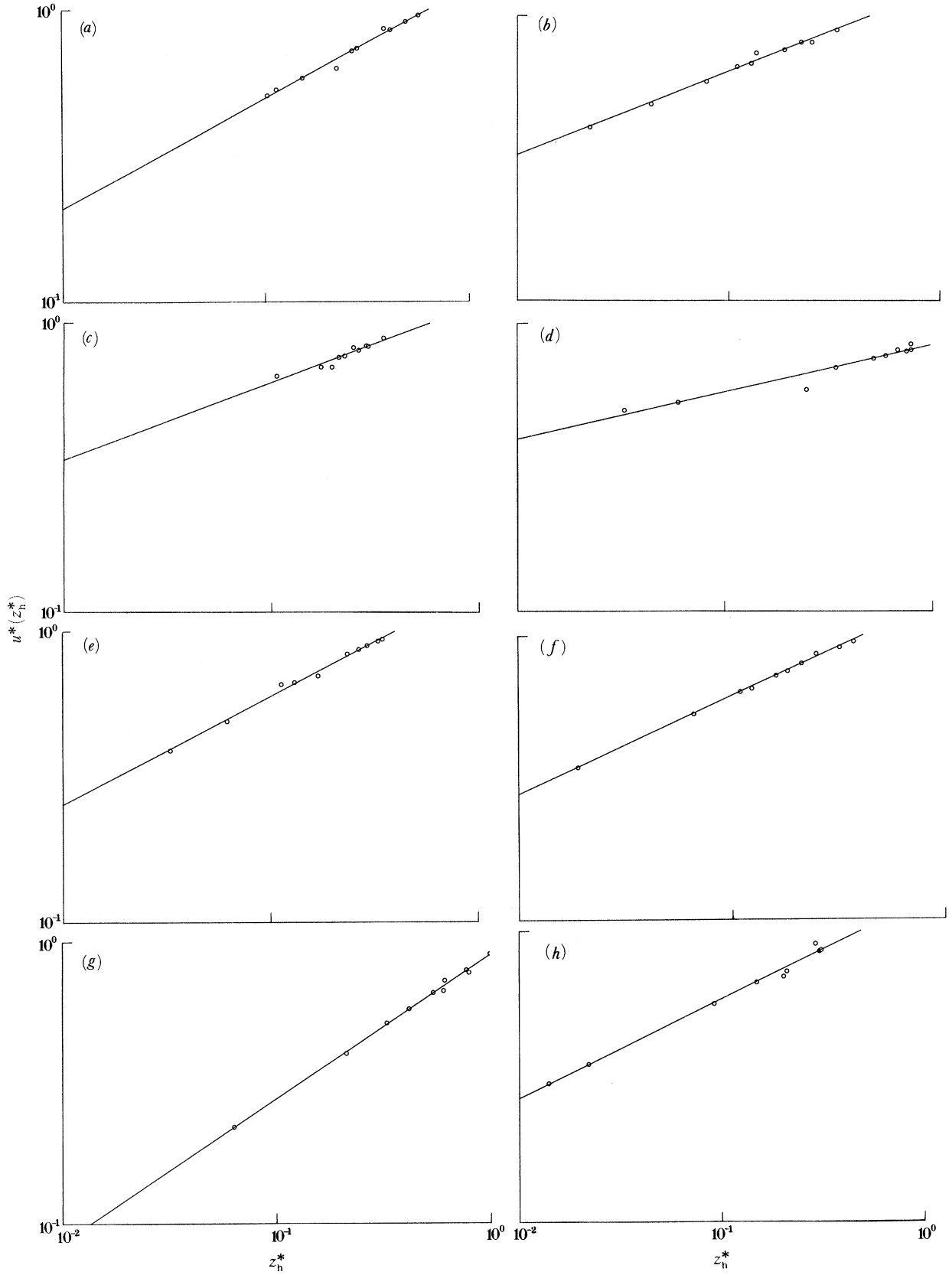

FIGURE 35. Logarithmic plots of $u^*(z_h^*)$ against z_h^* for $e = 9.4 \times 10^{-5}$, $h/H = 0.4$, $H/D = 1.0$, and $\{Bu:Ro\} =$ (*a*) {3.20:0.051}, (*b*) {7.40:0.047}, (*c*) {14.70:0.046}, (*d*) {1.80:0.093}, (*e*) {10.00:0.019}, (*f*) {21.20:0.031}, (*g*) {0.08:0.034}, (*h*) {23.70:0.044}.

The validity of the above empirical relationship was confirmed by plotting $\ln(u^*(z_h^*))$ against $\ln(z_h^*)$, and the gradients (B_1) and intercepts (I) were determined for different $Ro:Bu$ combinations from the resulting best straight line fits to the data. Typical examples of the logarithmic plots are shown in figure 35, from where it can be seen that the data are well represented by the above empirical expression.

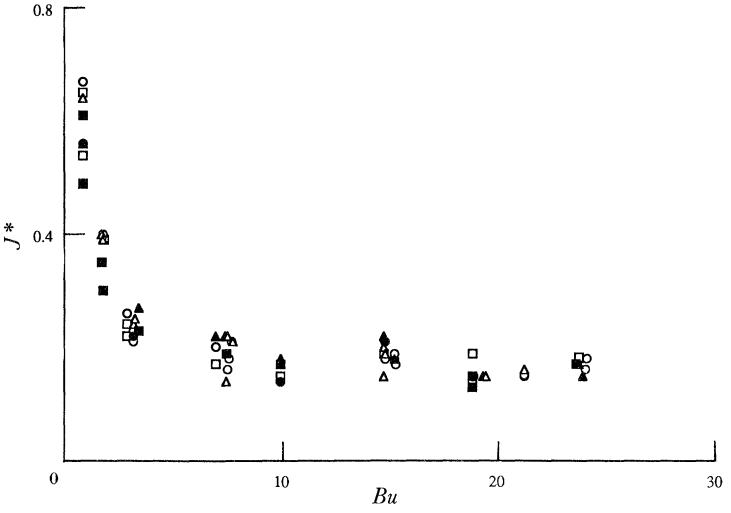

FIGURE 36. Plot of J^* against Bu for Ro ranges shown. Other parameters as figure 35. □, 0.01–0.025; ○, 0.026–0.040; △, 0.041–0.055; ■, 0.056–0.070; ●, 0.071–0.085; ▲, 0.086–0.10.

Figure 36 summarizes the measurements of the vertical attenuation in the strength of the disturbance, in terms of the dimensionless distance J^* ($=J/(H-h)$) and the Burger number, for all Ro values considered. Here, the quantity J^* (Ro, Bu) is the distance above the top of the obstacle to where $u^*(z_h^*)$ reaches the value 0.7. Such a quantity, which may be calculated easily from the decay constants B_1 and I serves as an arbitrary reference measure of the vertical extent of the flow disturbance generated by the obstacle. Figure 36 shows that J^* (related closely to the length of the Taylor column (Davies 1972, 1978; Baines & Davies 1980; Davies & Boyer 1984) and the Hide coherence length (Hide 1971)) decreases sharply with increasing Burger number. In addition, it can be seen from figure 36 that the attenuation in J^* with increasing Burger number is not affected by the value of the Rossby number of the flow. Both findings confirm (i) the strong influence of even very weak stratification upon the steering effect of the obstacle, and (ii) the reduction of the vertical extent of this steering to a region confined to typically 0.2 obstacle heights for $Bu \geqslant 5$. Such results confirm in all respects the only other measurements (Davies 1972) of the effects of stratification on the lengths of Taylor columns above spherical obstacles.

6. Shear layer structure

6.1. *Flow visualization*

For both the large-diameter full-depth cylinder and the truncated cylinder, some qualitative observations were made of the vertical shear layers circumscribing the obstacle. The thymol blue technique was used to visualize the flow, with dye release wires being inserted into grooves

in the cylinder wall. The wires were orientated parallel with the obstacle's vertical axis, and photographs were taken of the dye emitted from these wires. Figure 37 *a* and *b*, plate 18, shows the flow patterns around the two cylinders for $Bu = 0$. Note the strong vertical motions within the shear layers in both cases; on the front portion of the cylinder, dye is swept horizontally in the downstream direction, but on the side of the cylinder facing the observer, the dye converges with dye from the side of the cylinder out of view. Figure 37 *b* shows that dye is swept downward at the rear of the truncated cylinder and upward on the front portion.

6.2. *Theoretical shear layer structure*

There are, in reality, a number of different problems in the literature of the type described here. For example, Boyer (1970) conducted experiments in an apparatus for which the full-depth cylinder was fixed to a stationary upper and lower planes, with the fluid flowing past at speed U_0. (It is convenient to denote this particular experimental configuration be denoted as Type I.) In the present arrangement, by contrast, classified here as Type II, the cylinder was fixed to the lower boundary (a moving belt), and towed through the fluid beneath a stationary, rigid upper lid, as described in §3. Still other cases are those for which the lower surface and cylinder are at rest, with the fluid and the upper surface moving past at speed U_0 (Type III), or the cylinder alone is moved with speed U_0 through an initially quiescent fluid contained between stationary, rigid upper and lower planes (Type IV). Originally, Taylor (1923) conducted experiments of the latter type.

Now, the Navier–Stokes equations in a rotating frame may be easily shown to be invariant under a galilean transformation, so long as there are no pressure boundary conditions. Therefore, flow Types II and III are essentially identical. Type IV is altogether different, but, since no experimental shear layer data are available for this case, no further discussion of it is presented here.

For the purposes of this paper, Types I, II, and III only are considered. Note that the velocity discontinuity that occurs at the junction between the upper boundary and the cylinder for Type III has significant implications for the details of the Stewartson layer structure, as we shall see below. Hence, flow visualization of those shear layers in I (by Boyer 1970) and in III (here) yield very different results.

The radial volumetric flux in a horizontal-surface Ekman layer is given by

$$\tfrac{1}{2}(\nu/\Omega)^{\frac{1}{2}}(u_r^{(b)} + u_\theta^{(b)} - u_r - u_\theta), \tag{13}$$

where the superscript (b) denotes a velocity component of the solid boundary, and the unsubscripted components are those in the fluid at the Ekman layer edge. Throughout this section, we use cylindrical polar coordinates (r, θ, z), in the radial, azimuthal, and vertical directions; u_r, u_θ, w are the velocity components in those respective directions, with the oncoming flow toward the $\theta = 0$ direction. Formula (13) (see Greenspan 1964, p. 64) is valid on a surface with normal directed either along the rotation vector $\boldsymbol{\Omega}$ or opposite to it.

In any of the four cases, the geostrophic flow past the cylinder is the same, namely,

$$p = -2\rho\Omega U_0 \sin\theta (r - a^2/r), \tag{14}$$

where (r, θ, z) are the usual circular polar coordinates. At the cylinder, the geostrophic velocity vector is tangential to the cylinder, and $u_\theta = -2U_0 \sin\theta$.

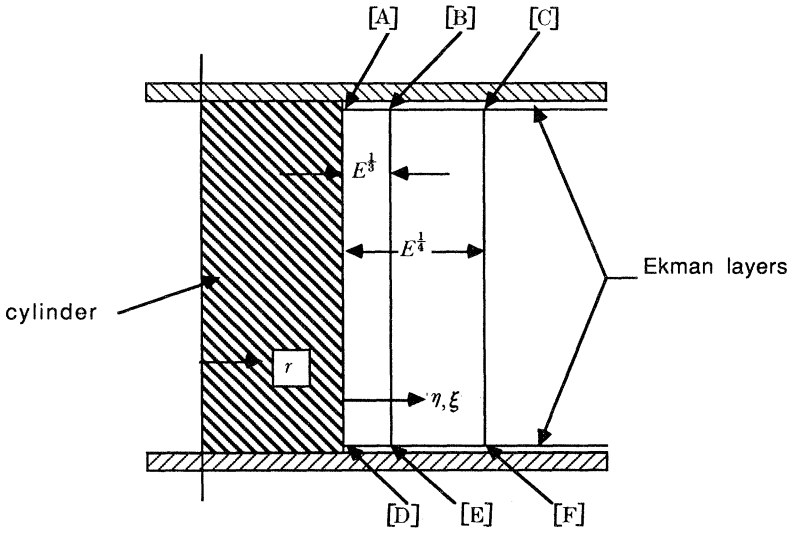

FIGURE 38. Schematic representation of Ekman and vertical shear layer structures for full cylinder cases. See text for [A], [B]...[F].

Consider first the lower boundary–cylinder juncture. We must now turn to the Stewartson layers themselves; a cross-sectional schematic of the shear layer structure is shown as figure 38. The outermost ($E^{\frac{1}{4}}$) layer has an azimuthal velocity profile given by

$$u_\theta = -2U_0 \sin\theta(1-\exp(-p(r-a))), \tag{15}$$

with p defined by $(2/H)^{\frac{1}{2}}/E^{\frac{1}{4}}$. There are corresponding radial and vertical velocity components also. Since the horizontal surface is at rest (in either I or III), the radial Ekman flux on the lower boundary at the cylinder [F] is given by $(\nu/\Omega)^{\frac{1}{2}}U_0 \sin\theta$. Clearly, there is no net inflow into the vertical boundary layer, but there is indeed a differential flux. However, since u_θ, from (15), and u_r both vanish at the base of the $\frac{1}{4}$-layer, at [E] in figure 38, (13) indicates that there is no volume flow remaining at [E]. Hence, no fluid enters the $\frac{1}{3}$-layer along the bottom wall.

6.2.1. *Type I shear layers*

Consider the flow at the upper boundary–cylinder connection. This situation is a repeat of the lower boundary case. There is a radial Ekman inflow of magnitude $(\nu/\Omega)^{\frac{1}{2}}U_0 \sin\theta$ at [C] in the figure, but no fluid remaining in the Ekman layer at [B]. Thus the $\frac{1}{3}$-layer structure is trivial. (The reader may find details of the kind of shear layer analysis used here in Moore & Saffman (1969) or Foster (1972), for example.)

The vertical shear layer velocity component in the outer $\frac{1}{4}$-layer is found to be

$$w = -2^{\frac{3}{2}}U_0(\tfrac{1}{2}-z/H)\,E^{\frac{1}{4}}\sin\theta\,\mathrm{e}^{-p(r-a)}. \tag{16}$$

Now, since $v = O(1)$, but both u_r and w are $O(E^{\frac{1}{4}})$, the streamlines in this layer are very nearly horizontal. The vertical velocity shown here indicates that in $z > \frac{1}{2}H$, for example, $w > 0$ on the 'left' side of the cylinder, i.e. that half of the cylinder to the left of the oncoming flow; there, θ lies between 0 and π. On the right side of the cylinder, the situation is reversed, with w negative above $\frac{1}{2}H$ and positive below. Hence, the streamlines are lines sloping up or down above or below the mid-plane of the cylinder, depending upon which side is in question.

6.2.2. *Types II and III shear layers*

We turn now to what is a far more complex flow, namely the one for which not only the fluid layer, but also the upper rigid lid slip past the cylinder at speed U_0; this is actually the Type III case, identical with a galilean transformation to Type II. Again, refer to figure 38. We have already noted that the radial Ekman flux at [F], on the lower surface, is given by $U_0(\nu/\Omega)^{\frac{1}{2}}\sin\theta$, and that there is no fluid still in the lower Ekman layer at [D], just as in §6.2.1. However, because the upper boundary is also in motion, equation (13) indicates that the flux of fluid at [C] is

$$\tfrac{1}{2}U_0(\nu/\Omega)^{\frac{1}{2}}(\cos\theta-\sin\theta) \quad \text{at} \quad [\text{C}]. \tag{17}$$

Though both u_r and u_θ vanish at [B], the motion of the plate still produces a flux at [B],

$$\tfrac{1}{2}U_0(\nu/\Omega)^{\frac{1}{2}}(\cos\theta+\sin\theta) \quad \text{at} \quad [\text{B}]. \tag{18}$$

For reasons discussed elsewhere (Moore & Saffman 1969) and not repeated here, all of the fluid in the Ekman layer at [B] must remain in the layer throughout the width of the $\frac{1}{3}$-layer, erupting as a point source at [A], as a result of the collision of the Ekman layer with the cylinder wall.

It might be objected that this picture is unnecessarily complicated, that the fluid in the Ekman layer at [B] merely turns between [A] and [B] to flow round the cylinder in the Ekman layer, flowing back outward on the other side of the cylinder; there seems no need for such a singularity since the net source strength is zero, i.e. the integral of the flux at [B] given in (18) above is zero. That is a more plausible flow at first glance, but is not possible. The reason is that the flux is $O(E^{\frac{1}{2}})$ at [B]. In order for the Ekman layer between [A] and [B] to carry such a flux, the azimuthal velocities in the Ekman layer must be very large, namely, $O(E^{-\frac{1}{3}})$, since $u\times(E^{\frac{1}{3}})\times(E^{\frac{1}{2}}) = O(E^{\frac{1}{2}})$. Such enormous velocities are very unlikely, and, in fact, they violate Moore & Saffman's (1969) 'Kutta Condition' for rotating flows: No fluid velocities in the shear layers may be larger than the fluid velocities at the shear layer edge. The singularity-solution requires velocities of $O(E^{\frac{1}{6}})$ only, by comparison.

Actually, the solution in the $\frac{1}{3}$-layer develops as an asymptotic series in powers of $E^{\frac{1}{12}}$; the first terms are

$$u_\theta = 0+E^{\frac{1}{12}}(-2^{\frac{3}{2}}U_0\sin\theta\eta)+E^{\frac{1}{6}}u_\theta^{(2)}+\ldots. \tag{19}$$

The 'η' in this expression is the scaled coordinate in the $\frac{1}{3}$-layer, $(r-a)/(\nu H/\Omega)^{\frac{1}{3}}$. It is important to mention here that the vertical velocity of $O(E^{\frac{1}{12}})$, corresponding to the second term in the series (19) for u_θ, is identically zero here, so that the largest vertical velocities in this interior layer are $O(E^{\frac{1}{6}})$. It is the $u_\theta^{(2)}$ term that is responsible for redistributing the volumetric flow, and $w^{(2)}$, in particular, is singular in the corner [A]. Equation (18) shows that the singularity is a source for θ between $\frac{3}{4}\pi$ and $\frac{7}{4}\pi$, and a sink for θ values between $-\frac{1}{4}\pi$ and $\frac{3}{4}\pi$.

6.2.3. *Types II, III: truncated cylinder*

We note finally the differences between the shear layer structure described immediately above, and that for a cylinder that does not meet the upper wall. The remarks about the $(u_\theta^{(2)}, w^{(2)})$ solution for the Type III flow are still correct. However, because the $\frac{1}{3}$-layer straddles the truncated cylinder side, and is therefore partly a boundary layer and partly a free shear layer, the first non-zero term in the series (19) above is no longer as written there. (See Foster (1972) for a complete analysis of the truncated cylinder problem.) In particular, specifically

in contrast to the flow around the full cylinder mentioned above, the $O(E^{\frac{1}{12}})$ w component, denoted by analogy with the other terms in (19) by $w^{(1)}$, is not identically zero for the cut-off cylinder. In fact, the $w^{(1)}$ term is very complex, with a weak, but important singularity at the 270° corner inside the shear layer, where the Ekman layer on the top surface of the cylinder erupts. Thus the vertical (w) and azimuthal (u) velocity components nearest the solid cylinder are both $O(E^{\frac{1}{12}})$.

6.3. *Comparison of theory and experiment*

The shear layer dye study of Boyer (1970) showed a V-shaped dye pattern precisely as one would expect based on the discussion at the end of §6.2.1. The relative sizes of u and w, with Boyer's Ekman number, E, of 4.3×10^{-4}, give an included angle for the dye wedge of about 12°. A measurement from Boyer's published figure gives 10°, so there seems to be good agreement with the theory.

In the dye studies done here, corresponding to the theoretical discussion in §6.2.2, it is predicted that the vertical velocities are $O(E^{\frac{1}{6}})$, with upflow for θ between $-\frac{1}{4}\pi$ and $\frac{3}{4}\pi$, and downflow on the other half-domain. Now, by series (19), u is slightly larger, $O(E^{\frac{1}{12}})$, hence streamlines will be expected again to be nearly horizontal (except for θ near 0 and π, where u vanishes, and so the flow should be upward or downward, respectively). The details are, however, quite complex since the $(u_\theta^{(2)}, w^{(2)})$ solution is itself non-trivial. We should expect, therefore, a general flatness of the streamlines, with no simple vertical structure apparent, aside from the fact that one expects the dye streaks to be generally downward (upward) on the front (rear) three-quarters of the right-side (left-side) flow, upward (downward) on the back (front).

The comparison of these results with the dye studies in the series of experiments described in §6.1 is clearly very poor, even qualitatively. One of the reasons for this may be that in the experiments the gap between the top of the circular cylinder and the upper boundary was wider than the Ekman width $(\nu/\Omega)^{\frac{1}{2}}$. It seems likely, therefore, that the layer structure is not that described in §6.2.2, but rather that for flow past a truncated cylinder, noted in §6.2.3. In fact, the similarity of the dye studies (figure 37) for the full-height cylinder and the truncated cylinder is the best evidence that such an explanation is valid.

The $E^{\frac{1}{6}}$ shear layer velocities, so important in the discussions for the full cylinder, are still present, because of the need to redistribute volume flow; and, at the Ekman numbers of these experiments, are only a factor of 0.4 smaller than the $E^{\frac{1}{12}}$ term. Thus we would expect to see $O(1)$ slopes for streamlines in a $z\theta$-plane on the cylinder sides, due to the $E^{\frac{1}{12}}$ term. However, near $\theta = 0, \pi$, where both $u_\theta^{(1)}, w^{(1)}$ vanish, the strong vertical motions associated with the source–sink behaviour of $w^{(2)}$ come to the fore–downward motion near the front of the cylinder, and upward motion at the back. This overall picture seems to agree well with the photographs. It is impossible to make a more quantitative comparison without having available detailed numerical computations of the $E^{\frac{1}{12}}$ and $E^{\frac{1}{6}}$ solutions, computations which are presently not available.

This work was supported financially by (i) the U.K. Natural Environment Research Council, through the award of a postgraduate studentship to R.G.D., (ii) the U.K. Science and Engineering Research Council research grant GR/E/53125, (iii) NATO Scientific Affairs Division research grant RG 85/005, and the U.S. National Science Foundation research grant MSM 8900046. The authors acknowledge this support with gratitude, and thank Mr E.

Moser, Mr E. Kuperus and Mr E. Blair for their invaluable technical help. Discussions held by one of us (P.A.D.) with Professor D. L. Boyer, M. G. Chabert d'Hieres, Dr D. J. Tritton and the late Professor L. O. Merkine have been particularly beneficial.

References

Baines, P. G. & Davies, P. A. 1980 Topographic effects in rotating and stratified fluids. In *Orographic effects in planetary flows* (ed. P. W. White & R. Hide), GARP Publications Ser. **23**, 233–299. Geneva: World Meteorological Organisation.

Baker, D. J. 1966 A technique for the precise measurement of small fluid velocities. *J. Fluid Mech.* **26**, 573–575.

Batchelor, G. K. 1970 *An introduction to fluid dynamics.* Cambridge University Press.

Bearman, P. W. & Graham, J. M. R. 1980 Vortex shedding from bluff bodies in oscillatory flow: a report on Euromech 119. *J. Fluid Mech.* **99**, 225–245.

Berger, E. & Wille, R. 1972 Periodic flow phenomena. *A. Rev. Fluid Mech.* **4**, 313–340.

Bouard, R. & Coutanceau, M. 1980 The early stage of development of the wake behind an impulsively started cylinder for $40 < Re < 10^4$. *J. Fluid Mech.* **101**, 583–607.

Boyer, D. L. 1970 Flow past a right circular cylinder in a rotating frame. *J. basic Engng* **92**, 430–436.

Boyer, D. L. & Davies, P. A. 1982 Flow past a circular cylinder on a β-plane. *Phil. Trans. R. Soc. Lond.* A **306**, 533–556.

Boyer, D. L. & Kmetz, M. L. 1983 Vortex shedding in rotating flows. *Geophys. Astrophys. Fluid Dyn.* **26**, 51–84.

Boyer, D. L., Davies, P. A. & Holland, W. R. 1984*a* Rotating flow past discs and cylindrical depressions. *J. Fluid Mech.* **141**, 67–95.

Boyer, D. L., Kmetz, M. L., Smathers, L., Chabert d'Hieres, G. & Didelle, H. 1984*b* Rotating open channel flow past right circular cylinders. *Geophys. Astrophys. Fluid Dyn.* **30**, 271–304.

Boyer, D. L., Davies, P. A., Holland, W. R., Biolley, F. & Honji, H. 1987 Stratified rotating flow over and around isolated three-dimensional topography. *Phil. Trans. R. Soc. Lond.* A **322**, 213–241.

Brevdo, L. & Merkine, L. 1985 Boundary layer separation of a two-layer rotating flow on an f plane. *Proc. R. Soc. Lond.* A **400**, 75–95.

Chabert d'Hieres, G., Davies, P. A. & Didelle, H. 1989 A laboratory study of the lift forces on a moving solid obstacle in a rotating fluid. *Dyn. Atmos. Oceans* **13**, 47–75.

Chabert d'Hieres, G., Davies, P. A. & Didelle, H. 1990 Experimental studies of lift and drag upon cylindrical obstacles in homogeneous, rotating fluids. *Dyn. Atmos. Oceans.* (In the press.)

Collins, W. M. & Dennis, S. C. R. 1973 Flow past an impulsively started circular cylinder. *J. Fluid Mech.* **60**, 105–127.

Coutanceau, M. & Bouard, R. 1977*a* Experimental determination of the main features of the viscous flow in the wake of a circular cylinder in uniform translation. Part 1. Steady flow. *J. Fluid Mech.* **79**, 231–256.

Coutanceau, M. & Bouard, R. 1977*b* Experimental determination of the main features of the viscous flow in the wake of a circular cylinder in uniform translation. Part 2. Unsteady flow. *J. Fluid Mech.* **79**, 257–272.

Davies, P. A. 1972 Experiments on Taylor columns in rotating stratified fluids. *J. Fluid Mech.* **54**, 691–717.

Davies, P. A. 1978 Topographic effects in rotating stratified fluids: laboratory experiments. In *Rotating fluids in geophysics* (ed. P. H. Roberts & A. M. Soward), pp. 249–266. London: Academic Press.

Davies, P. A. & Rahm, L. 1982 The interaction between topography and a non-linearly stratified rotating fluid. *Phys. Fluids* **25**, 1931–1934.

Davies, P. A. & Boyer, D. L. 1984 Quasi-geostrophic flow past isolated obstacles. *Riv. Meteorologia Aeronautica* **44**, 23–31.

Davies, P. A. & Mofor, L. A. 1990 Observations of flow separation by an isolated island. *J. Remote Sensing.* (In the press.)

Davis, R. G. 1989 Flow past a circular cylinder in a rotating stratified fluid. Ph.D. dissertation, University of Dundee, U.K.

Foster, M. R. 1972 The flow caused by the differential rotation of a right circular cylindrical depression in one of two rapidly-rotating parallel planes. *J. Fluid Mech.* **53**, 647–667.

Foster, M. R. 1989 Rotating and stratified flow past a steep-sided obstacle. Incipient separation. *J. Fluid Mech.* **206**, 47–73.

Gerrard, J. H. 1978 The wakes of cylindrical bluff bodies at low Reynolds number. *Phil. Trans. R. Soc. Lond.* A **288**, 351–382.

Greenspan, H. P. 1968 *The theory of rotating fluids.* Cambridge University Press.

Heikes, K. E. & Maxworthy, T. 1982 Observations of inertial waves in a homogeneous rotating fluid. *J. Fluid Mech.* **125**, 319–344.

Hide, R. 1971 On geostrophic motion of a non-homogeneous fluid. *J. Fluid Mech.* **49**, 745–750.

Hide, R. & Ibbetson, A. 1966 An experimental study of Taylor columns. *Icarus* **5**, 279–290.

Hogg, N. G. 1973 On the stratified Taylor column. *J. Fluid Mech.* **58**, 517–537.
Honji, H. & Taneda, S. 1969 Unsteady flow past a circular cylinder. *J. phys. Soc., Japan* **27**, 1668–1677.
Honji, H., Taneda, S. & Tatsuno, A. 1980 Some practical details of the electrolytic precipitation method of flow visualization. *Res. Inst. appl. Mech., Kyushu Univ.* **28**, 83–89.
Imaichi, K. & Ohmi, K. 1983 Numerical processing of flow-visualization pictures measurement of two dimensional vortex flow. *J. Fluid Mech.* **129**, 283–311.
James, I. N. 1980 Forces due to geostrophic flow over shallow topography. *Geophys. Astrophys. Fluid Dyn.* **14**, 225–250.
Kmetz, M. L. 1982 Vortex shedding in rotating flows. M.S. dissertation, University of Wyoming, U.S.A.
Mair, W. A. & Maull, D. J. 1971 Bluff bodies and vortex shedding – a report on Euromech 17. *J. Fluid Mech.* **45**, 209–224.
Mason, P. J. 1975 Forces on bodies moving transversely through a rotating fluid. *J. Fluid Mech.* **71**, 577–599.
Matsuura, T. & Yamagata, T. 1983 A numerical study of a viscous flow past a right circular cylinder on a beta-plane. *Geophys. Astrophys. Fluid Dyn.* **37**, 129–164.
Maxworthy, T. 1970 The flow created by a sphere moving along the axis of a rotating, slightly-viscous fluid. *J. Fluid Mech.* **40**, 453–479.
Merkine, L. O. 1980 Flow separation on a β-plane. *J. Fluid Mech.* **99**, 399–409.
Merkine, L. O. 1985 A linear analysis of rotating stratified flow past a cylinder on an f-plane. *J. Fluid Mech.* **157**, 501–518.
Merkine, L. O. & Kalnay-Rivas, E. 1976 Rotating stratified flow over finite isolated topography. *J. atmos. Sci.* **33**, 908–922.
Merkine, L. O. & Solan, A. 1979 The separation of the flow past a cylinder in a rotating frame. *J. Fluid Mech.* **92**, 381–392.
Moore, D. W. & Saffman, P. G. 1969 The structure of free vertical shear layers in a rotating fluid and the motion produced by a slowly rising body. *Phil. Trans. R. Soc. Lond.* A **264**, 597–634.
Morkovin, M. V. 1964 Flow around circular cylinder – a kaleidoscope of challenging fluid phenomena. In *Symposium on fully separated flows* (ed. A. G. Hansen), pp. 102–118. New York: ASME.
Nishioka, M. & Sato, H. 1974 Measurements of velocity distributions in the wake of a circular cylinder at low Reynolds number 5. *J. Fluid Mech.* **65**, 97–112.
Oster, G. 1965 Density gradients. *Scient. Am.* **213**, 70–76.
Page, M. A. 1985 On the low-Rossby number flow of a rotating fluid past a circular cylinder. *J. Fluid Mech.* **156**, 205–221.
Pattiaratchi, C., James, A. & Collins, M. 1986 Island wakes and headland eddies: a comparison between remotely sensed data and laboratory experiments. *J. geophys. Res.* **92**, 783–794.
Prandtl, L. & Tietjens, O. G. 1934 *Applied hydro- and aerodynamics*. New York: McGraw-Hill.
Roshko, A. 1954 On the development of turbulent wakes from vortex streets. N.A.C.A. Rep. 1191.
Serotsky, P. & Titman, C. W. 1975 Length of a viscous-limited Taylor column. *Phys. Fluids* **18**, 748–749.
Son, J. S. & Hanratty, T. J. 1969 Numerical solution for the flow around a cylinder at Reynolds numbers of 40, 200 and 500. *J. Fluid Mech.* **35**, 369–386.
Spence, G. S. M. 1986 Studies of baroclinic flows in rotating fluids. Ph.D. dissertation, University of Dundee, U.K.
Taneda, S. 1956 Experimental investigation of the wakes behind cylinders and plates at low Reynolds numbers. *J. phys. Soc. Japan* **11**, 302–307.
Taylor, G. I. 1923 Experiments on the motion of solid bodies in rotating fluids. *Proc. R. Soc. Lond.* A **104**, 213–218.
Tritton, D. J. 1988 *Physical fluid dynamics*, 2nd edn. Oxford University Press.
Verron, J. & Le Provost, C. 1985 A numerical study of quasi-geostrophic flow over isolated topography. *J. Fluid Mech.* **154**, 231–252.
Walker, J. D. A. & Stewartson, K. 1972 The flow past a cylinder in a rotating frame. *Z. angew. Math. Phys.* **23**, 745–752.
Walker, J. D. A. & Stewartson, K. 1974 Separation and the Taylor column problem for a hemisphere. *J. Fluid Mech.* **66**, 767–780.
West, G. S. & Apelt, C. J. 1982 The effects of tunnel blockage and aspect ratio on the mean flow past a circular cylinder with Reynolds numbers between 10^4 and 10^5. *J. Fluid Mech.* **115**, 361–377.
Wolanski, E., Imberger, J. & Heron, M. L. 1984 Island wakes in shallow coastal waters. *J. geophys. Res.* **86** (C6), 10553–10569.

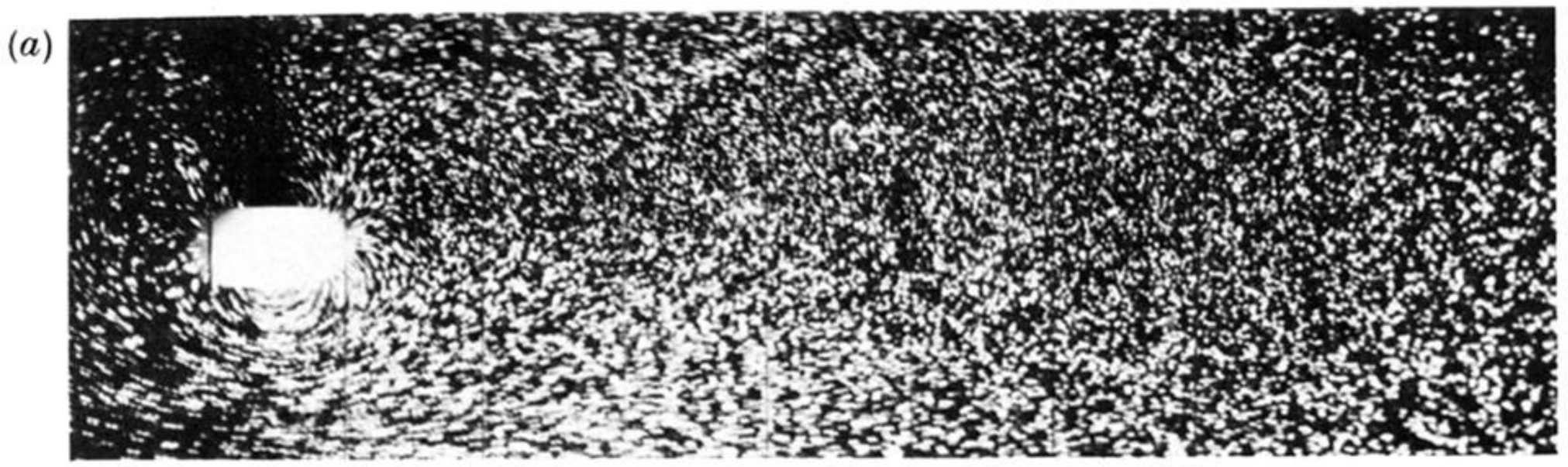

FIGURE 2. Time sequence of plan photographs in decoupled frame for $Bu = 23.8$, $Ro = 0.029$, $E = 9.4 \times 10^{-5}$, $h/H = 1.0$, $H/D = 2.5$ and t_A^* is (*a*) 0.88, (*b*) 6.21, (*c*) 15.92, (*d*) 22.48, and (*e*) 25.60. Sense of background rotation counter-clockwise.

(a)

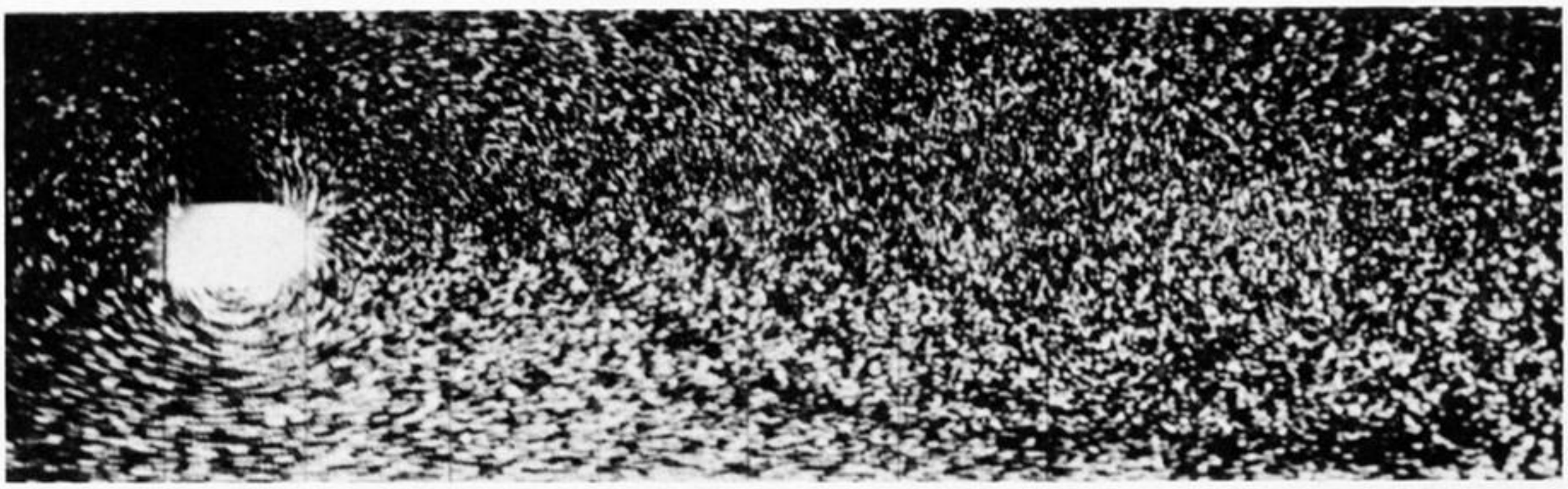

(b)

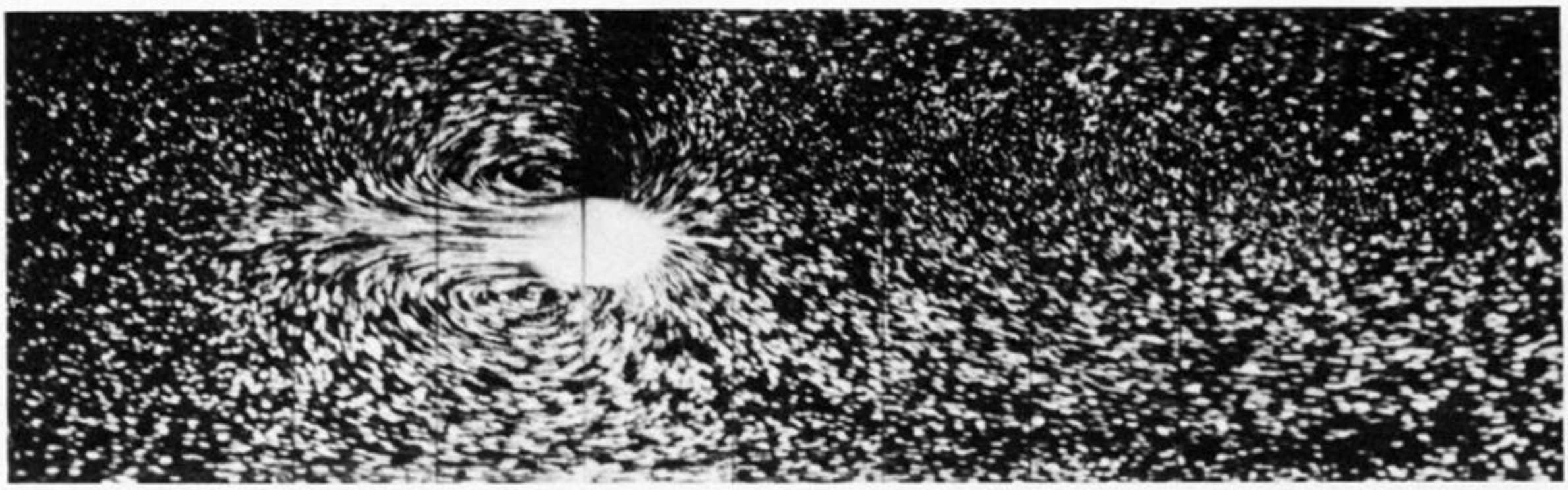

(c)

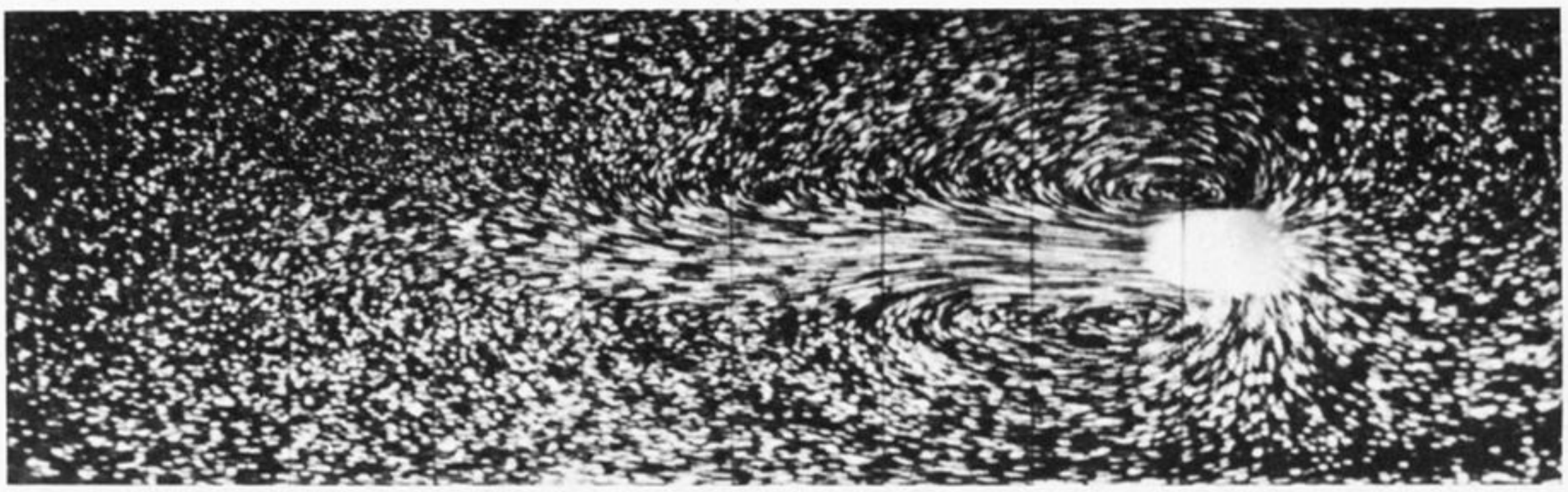

(d)

(e)

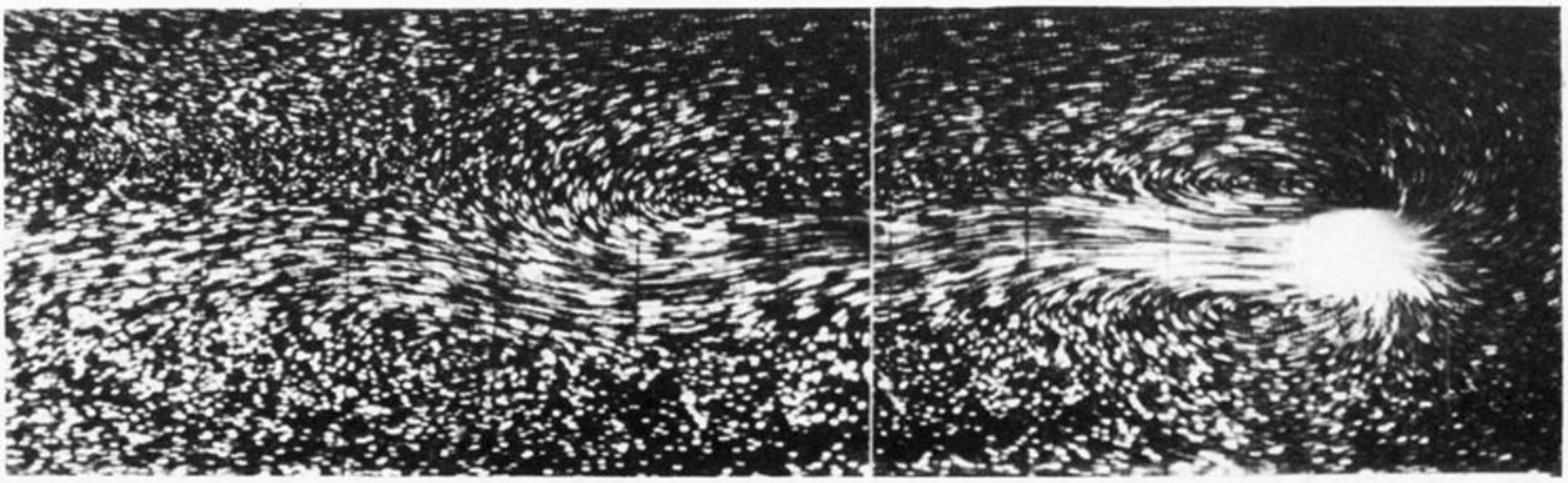

FIGURE 3. Same legend as figure 2, except $Ro = 0.033$ and t_A^* is (*a*) 0.78, (*b*) 8.52, (*c*) 14.04, (*d*) 21.30, and (*e*) 24.42.

(*a*)

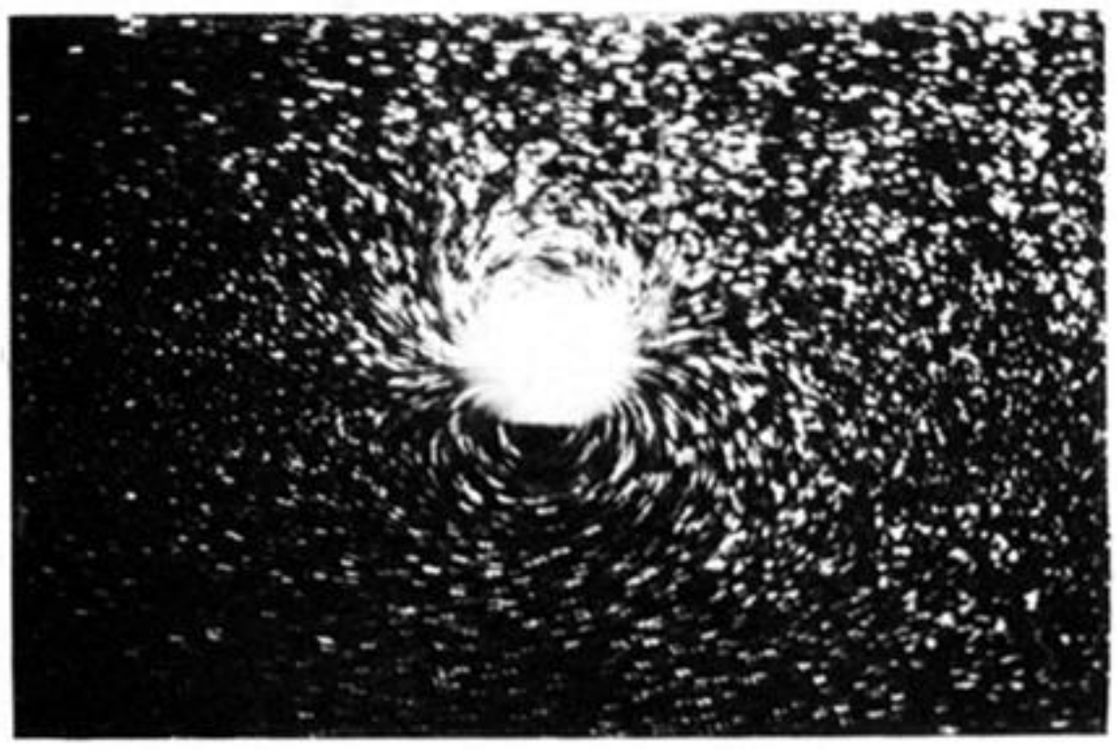

(*b*)

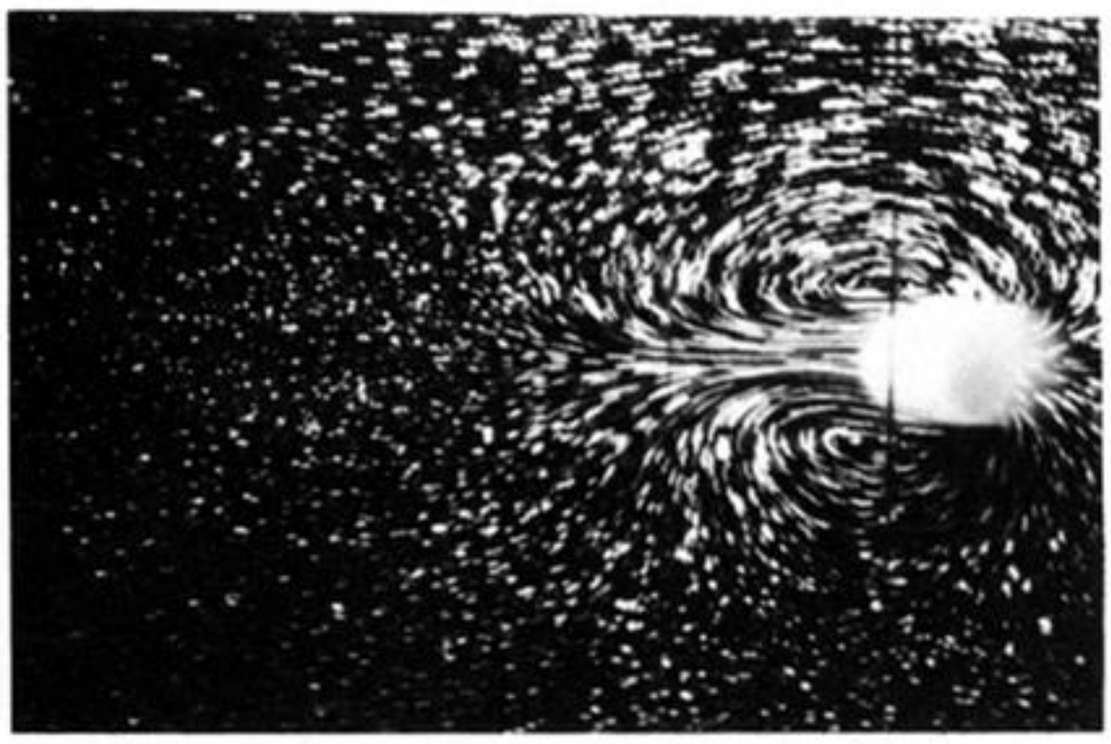

(*c*)

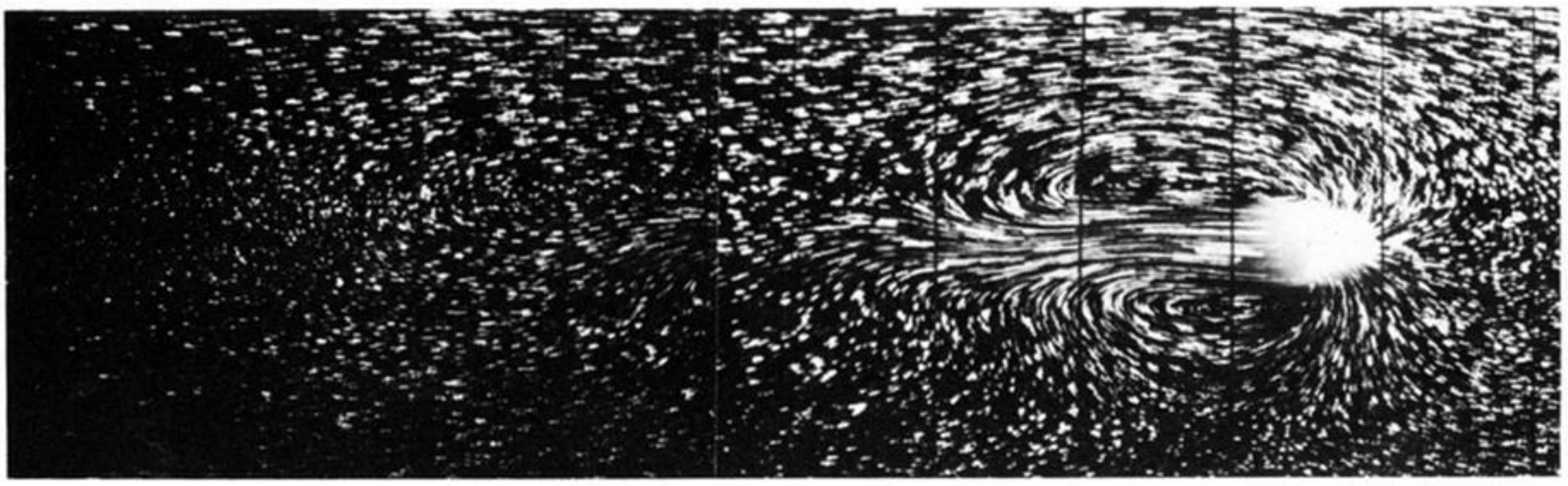

(*d*)

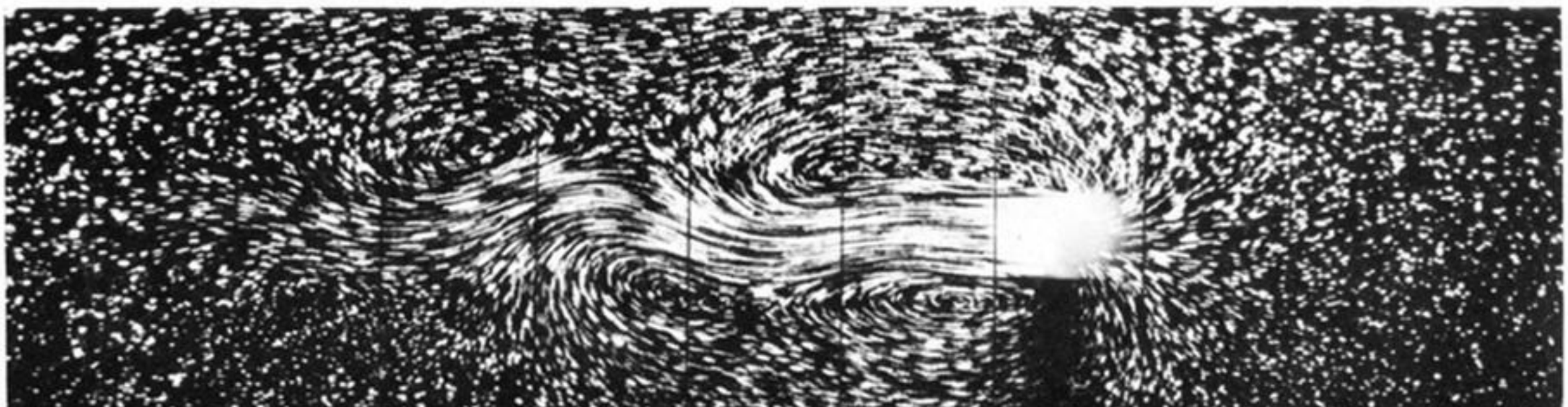

(*e*)

FIGURE 4. Same legend as figure 2, except $Ro = 0.044$ and t_A^* is (*a*) 0.84, (*b*) 5.24, (*c*) 12.84, (*d*) 19.08, and (*e*) 24.52.

(a)

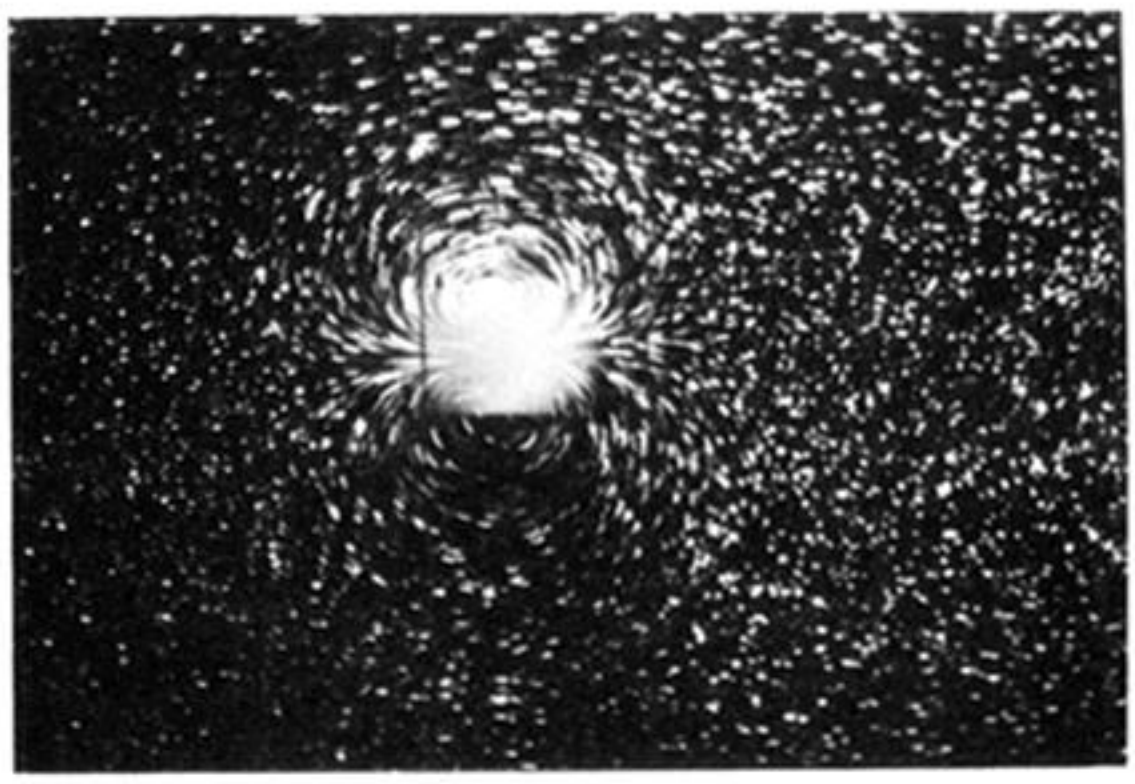

(b)

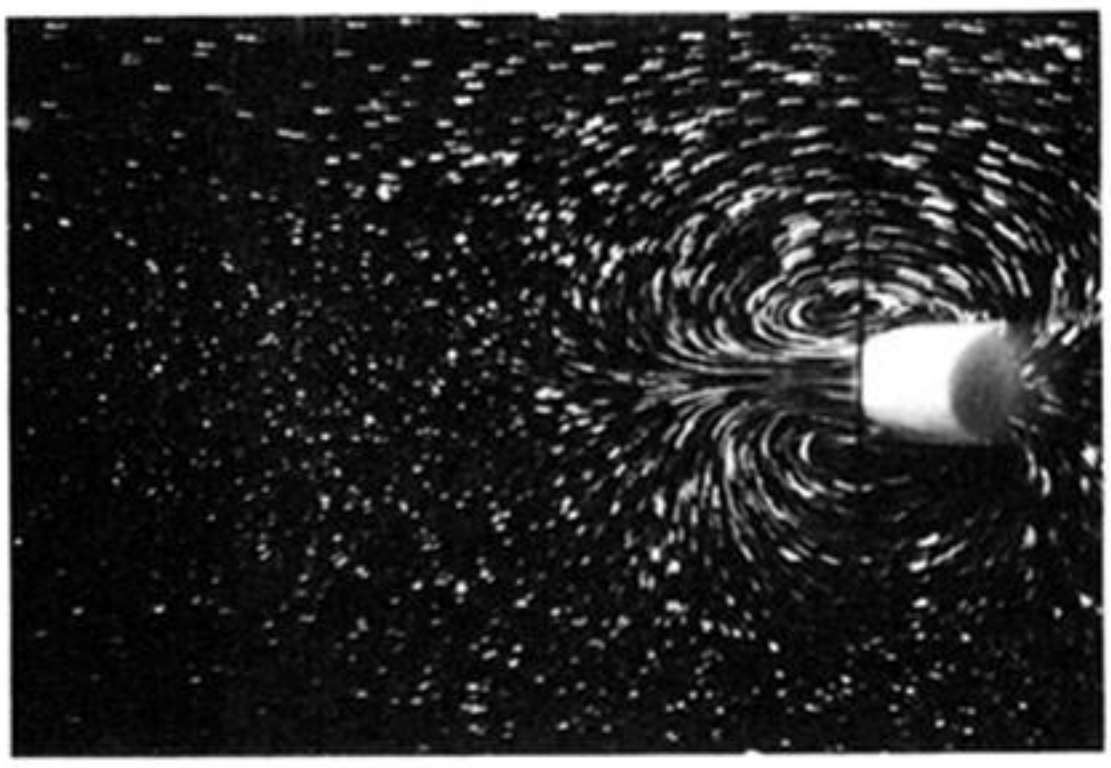

(c)

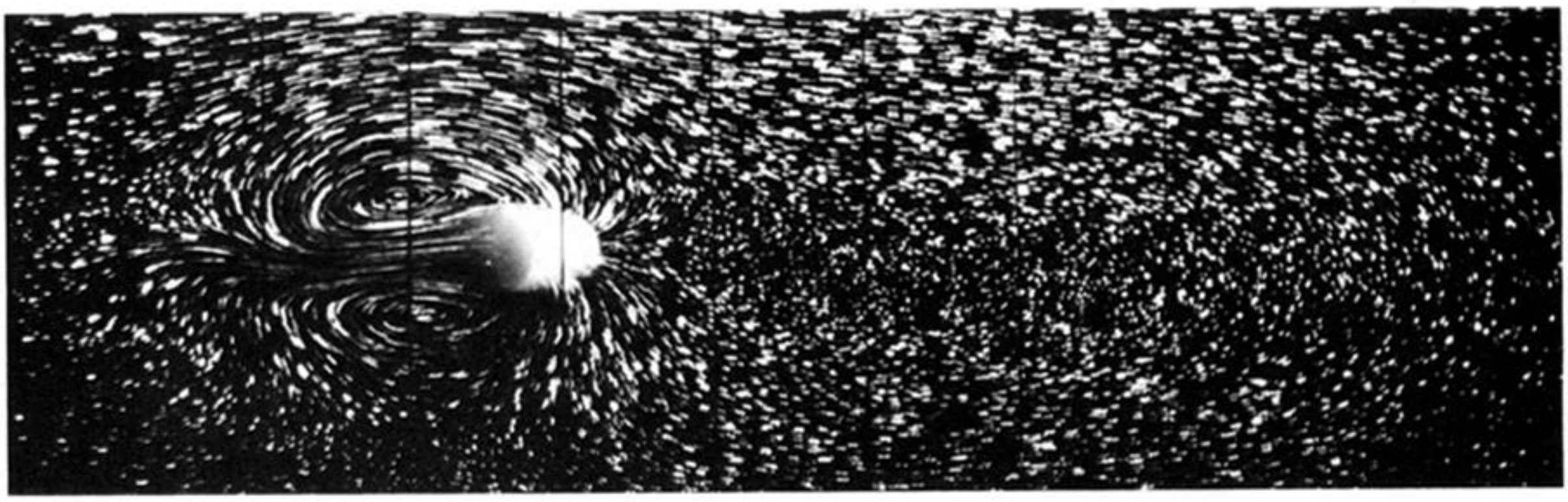

(d)

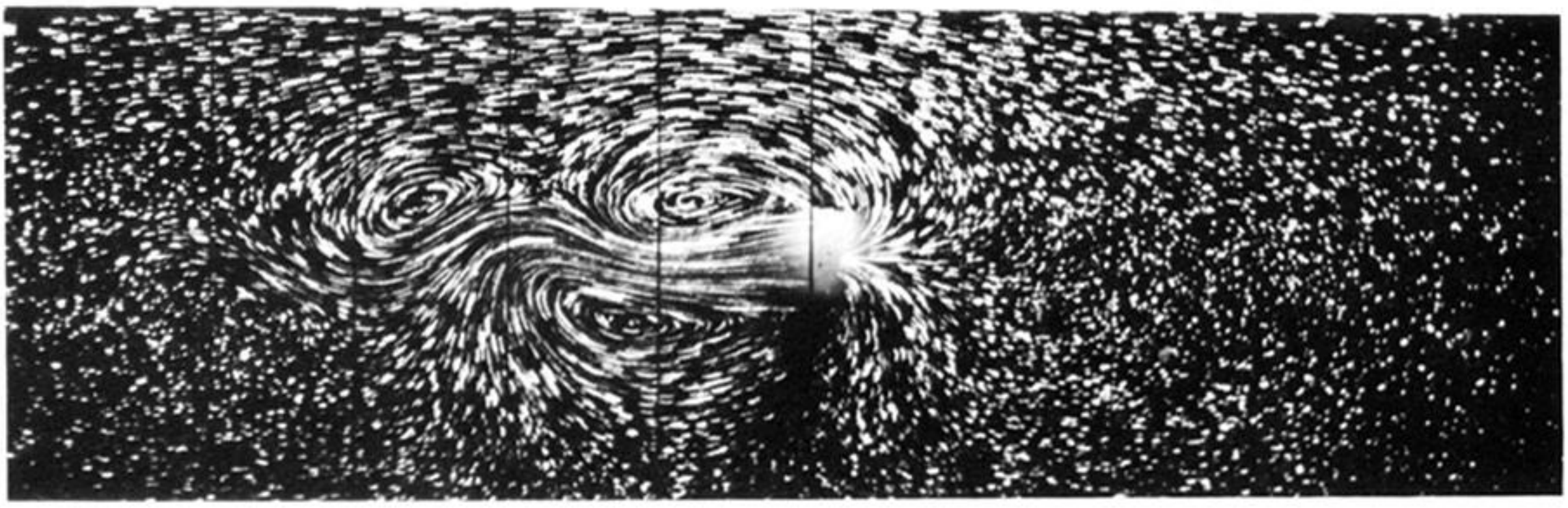

(e)

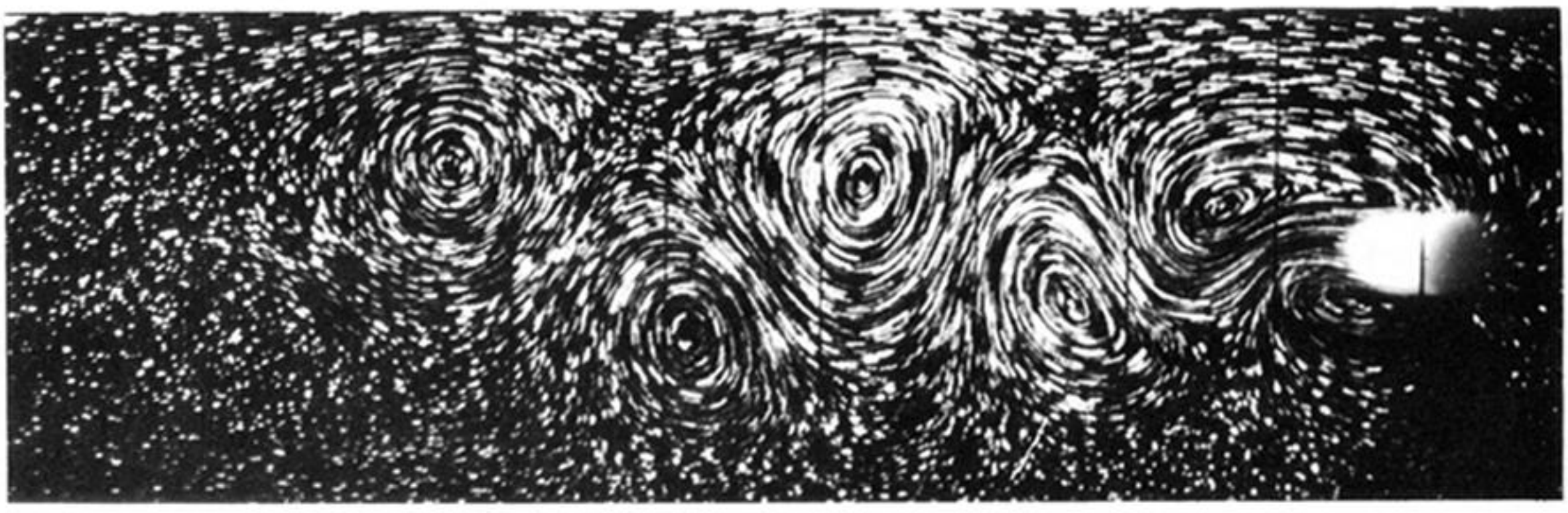

FIGURE 5. Same legend as figure 2, except $Bu = 23.9$, $Ro = 0.095$, and t_A^* is (*a*) 0.87, (*b*) 5.55, (*c*) 11.44, (*d*) 16.12, and (*e*) 24.18.

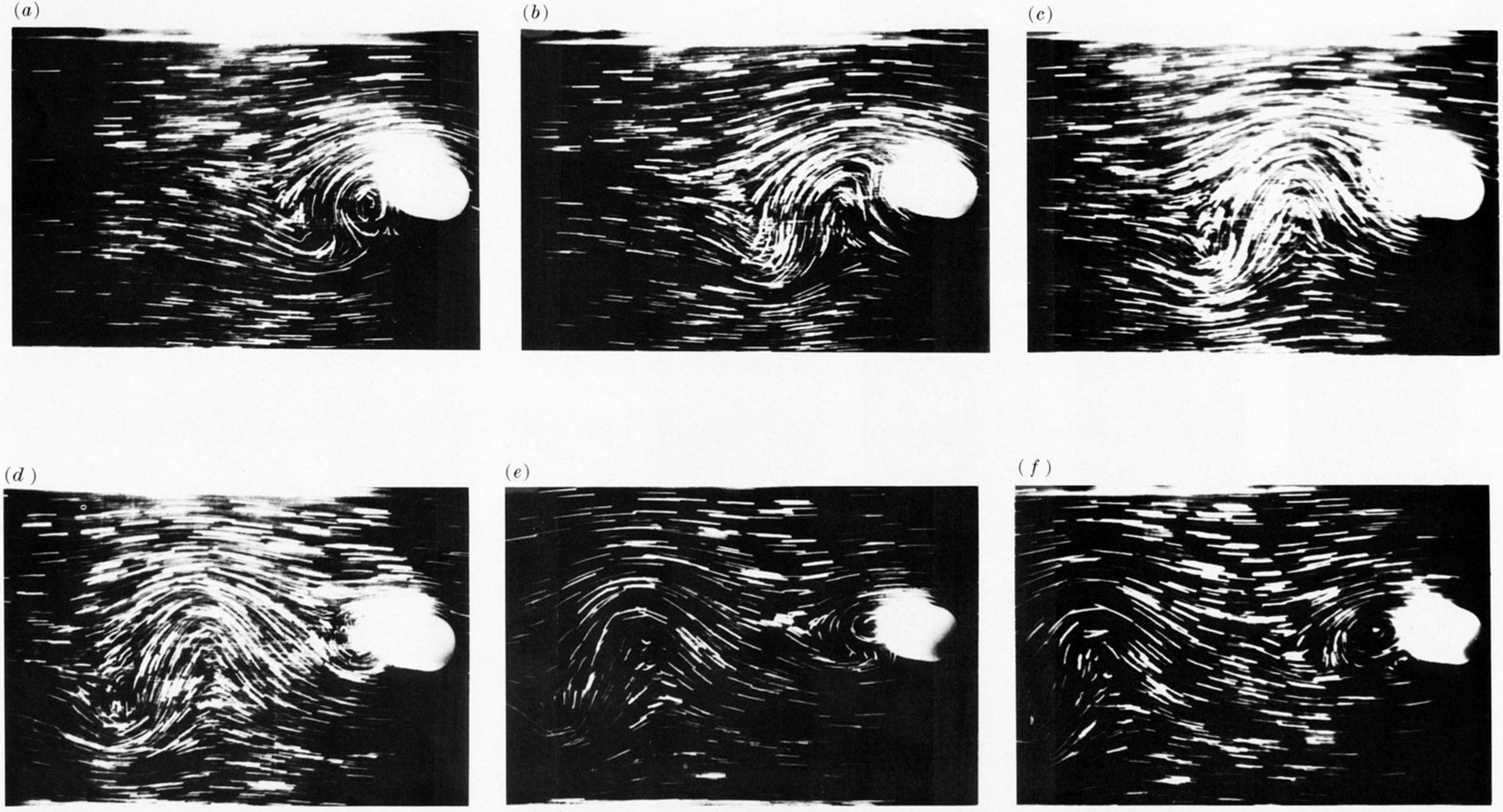

FIGURE 6. Same legend as figure 2, except coupled frame, $Bu = 11.6$, $Ro = 0.41$, and t_A^* is (*a*) 6.10, (*b*) 7.30, (*c*) 8.40, (*d*) 9.60, (*e*) 10.70, and (*f*) 11.90.

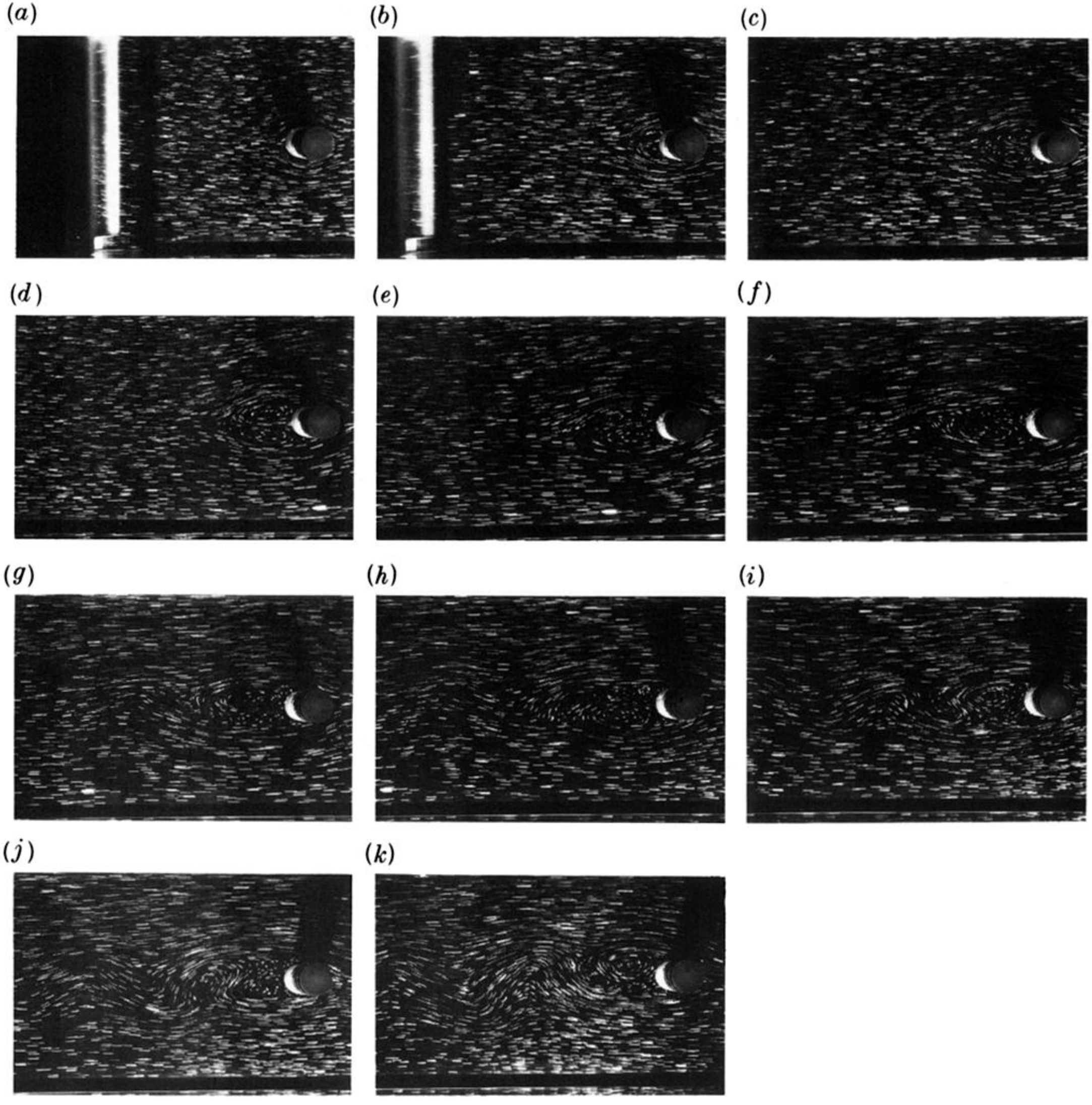

FIGURE 7. Same legend as figure 2, except coupled frame, $Bu = 25.80$, $Ro = 0.065$, and t_A^* is (*a*) 0.13, (*b*) 2.75, (*c*) 5.40, (*d*) 8.00, (*e*) 10.60, (*f*) 13.30, (*g*) 15.90, (*h*) 18.50, (*i*) 21.10, (*j*) 23.80, and (*k*) 26.40.

(i) (*a*) (*b*) (*c*)

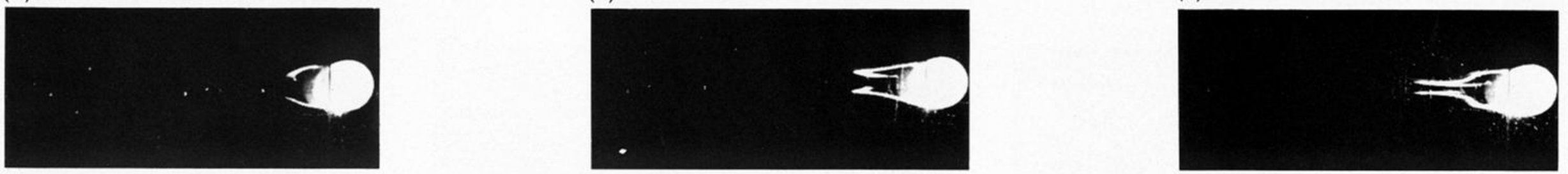

(*d*) (*e*) (*f*)

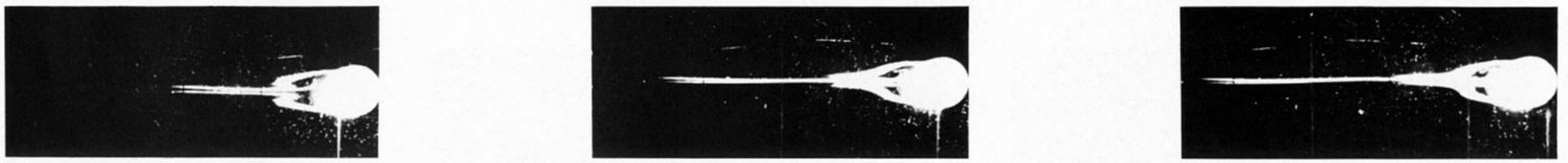

(ii) (*a*) (*b*) (*c*)

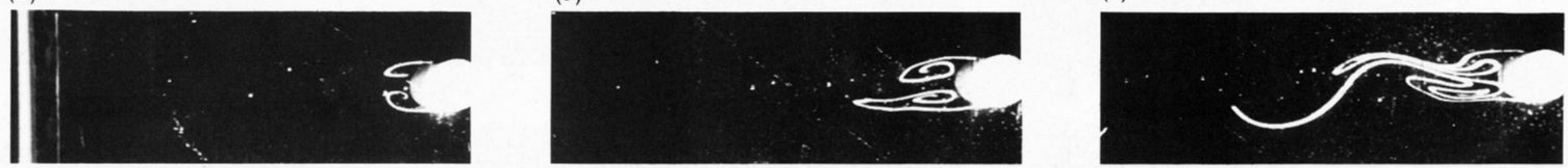

(*d*) (*e*) (*f*)

FIGURE 8. Same legend as for figure 2, except coupled frame, $Bu = 10.56$, and (i) $Ro = 0.033$, t_A^* is (*a*) 7.04, (*b*) 10.34, (*c*) 12.16, (*d*) 15.38, (*e*) 19.47, (*f*) 23.21; and (ii) $Ro = 0.071$, t_A^* is 4.17, (*b*) 8.47, (*c*) 12.30, (*d*) 15.85, (*e*) 19.61, and (*f*) 23.92.

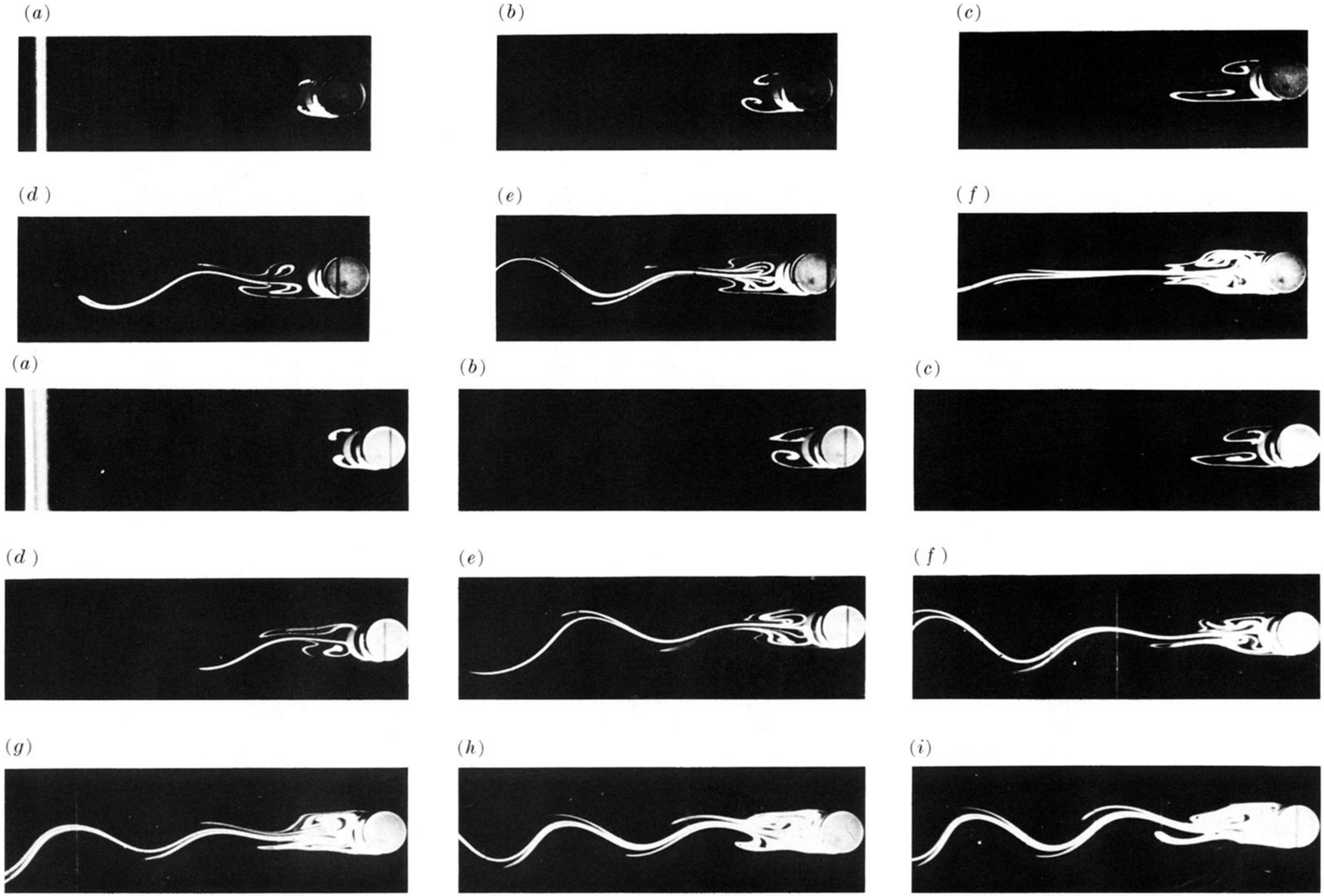

FIGURE 9. Same legend as figure 2, except coupled frame, $Bu = 1.80$, and (i) $Ro = 0.063$, t_A^* is (*a*) 2.28, (*b*) 5.16, (*c*) 9.00, (*d*) 12.60, (*e*) 19.20, (*f*) 30.00; and (ii) $Ro = 0.064$, t_A^* is (*a*) 2.86, (*b*) 4.75, (*c*) 7.12, (*d*) 10.34, (*e*) 15.33, (*f*) 18.37, (*g*) 21.41, (*h*) 24.46, (*i*) 25.79.

(a)

(i)

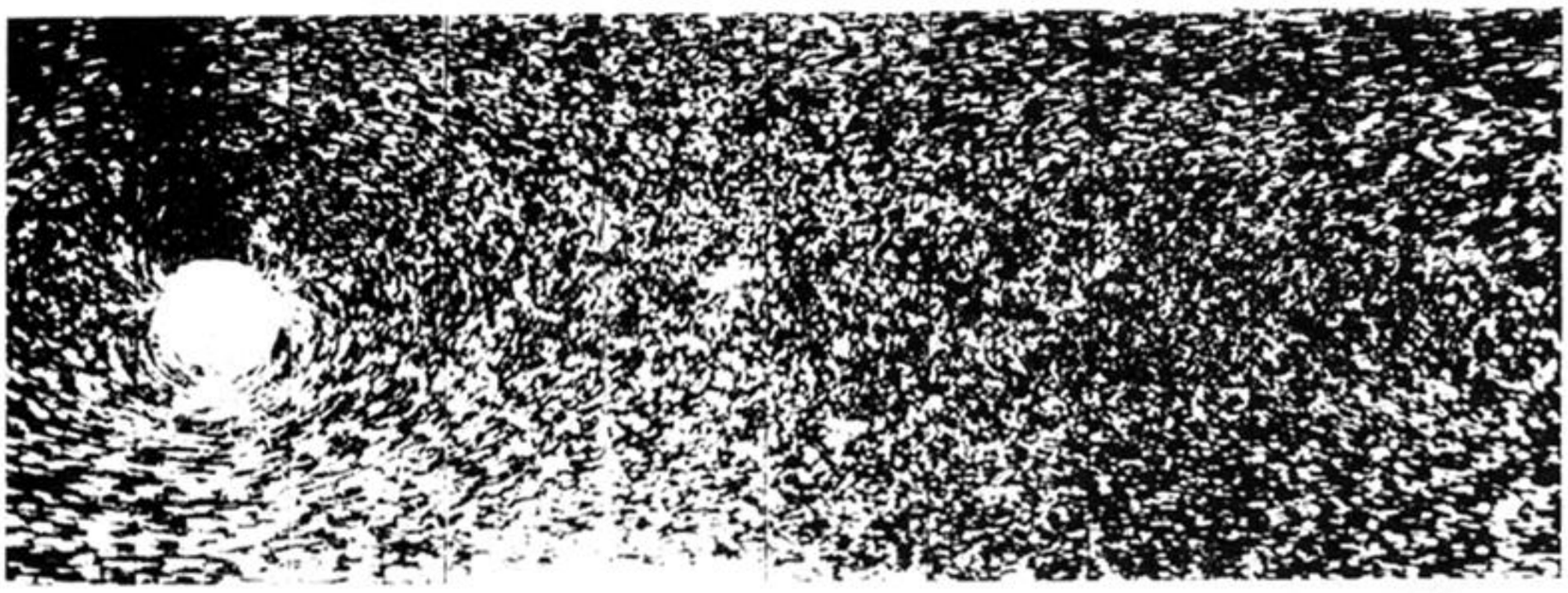

(ii)

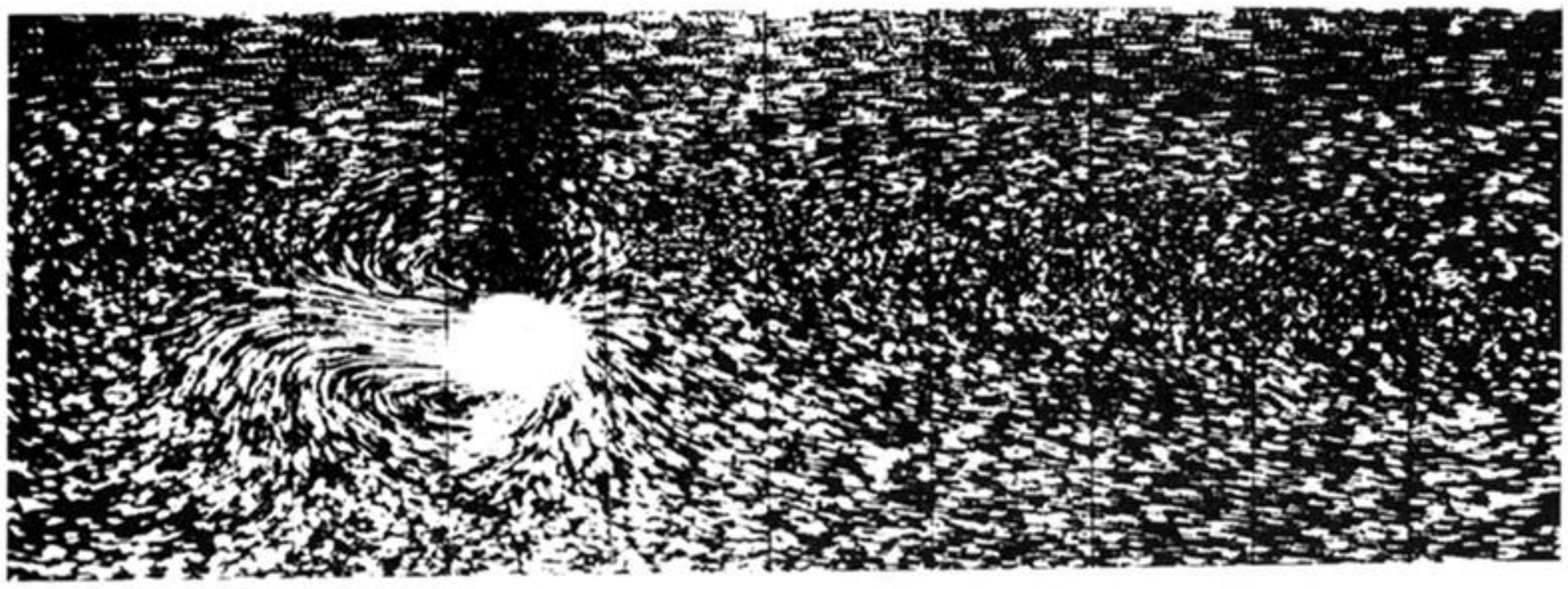

(iii)

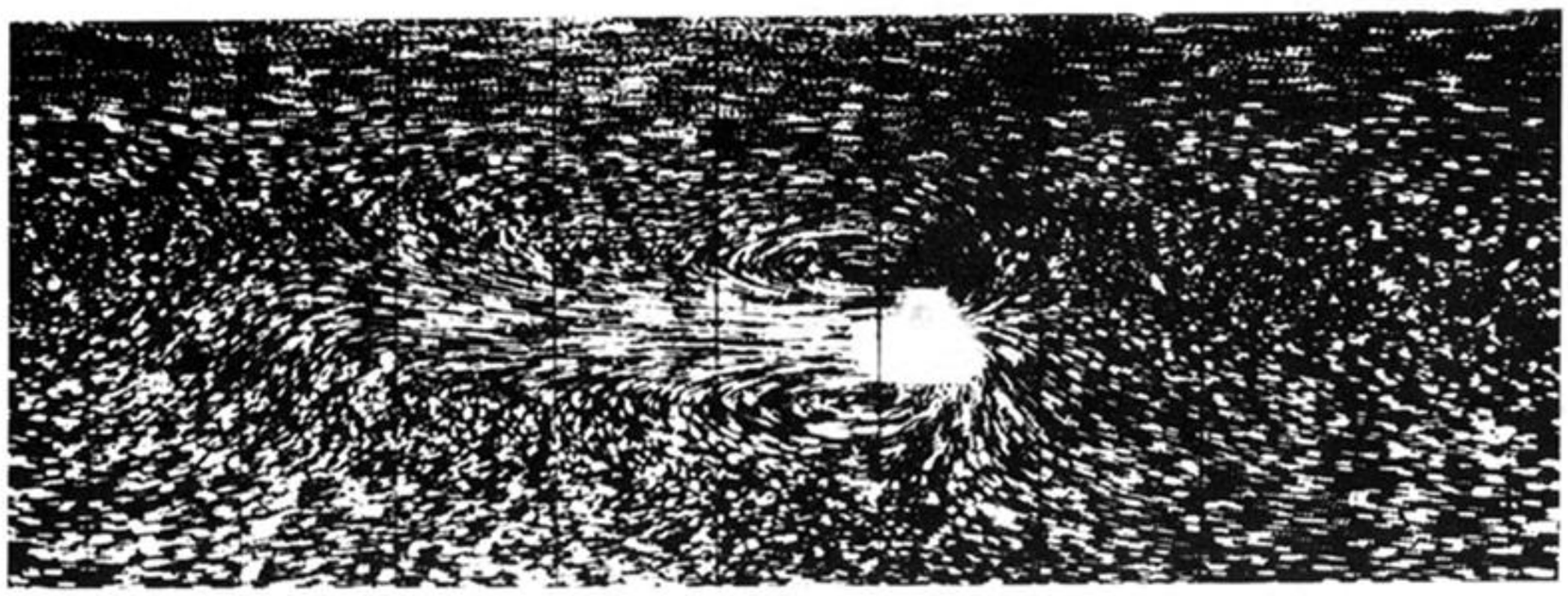

(iv)

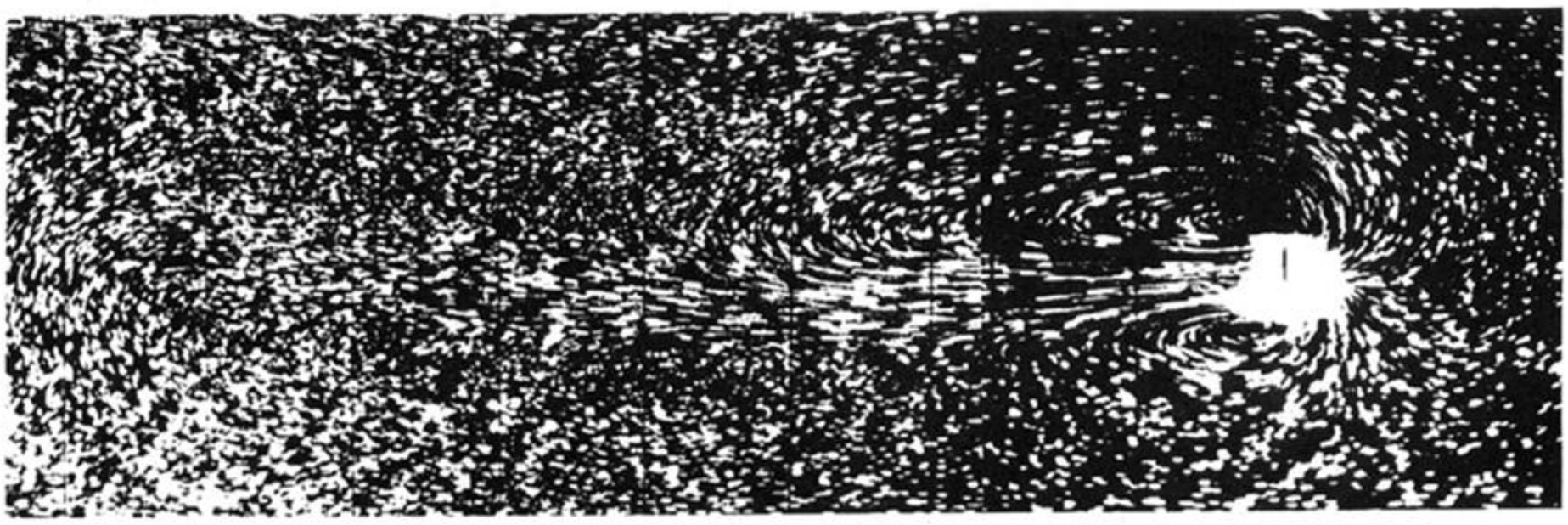

(v)

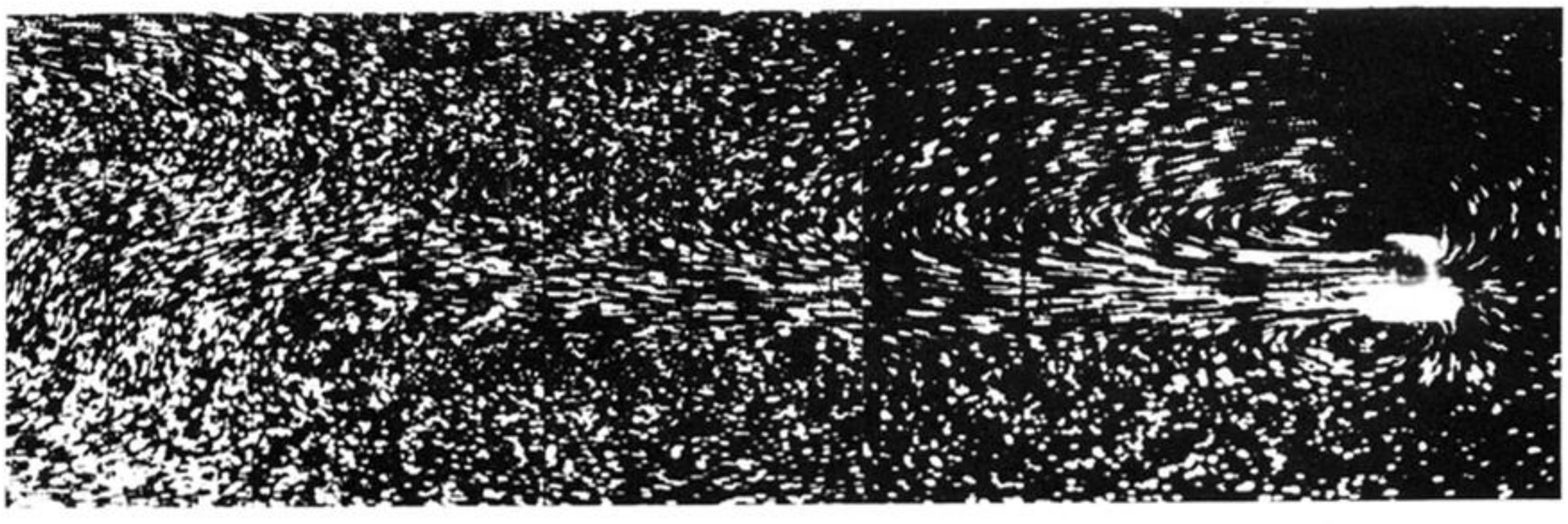

FIGURE 25. Plan photograph time sequences in decoupled frame, for $z^* = 0.2$, $E = 9.4 \times 10^{-5}$, $h/H = 0.40$, $h/D = 1.0$, and $\{Bu:Ro\} =$ (*a*) {18.75:0.024}, (*b*) {19.30:0.051}, (*c*) {18.80:0.081}. Values of $t_A^* =$ (*a*) 0.78; 5.10; 11.20; 22.10; 25.70, (*b*) 0.80; 6.30; 12.90; 23.10; 26.90, (*c*) 0.81; 5.40; 11.30; 22.10; 25.30.

(*b*)

(i)

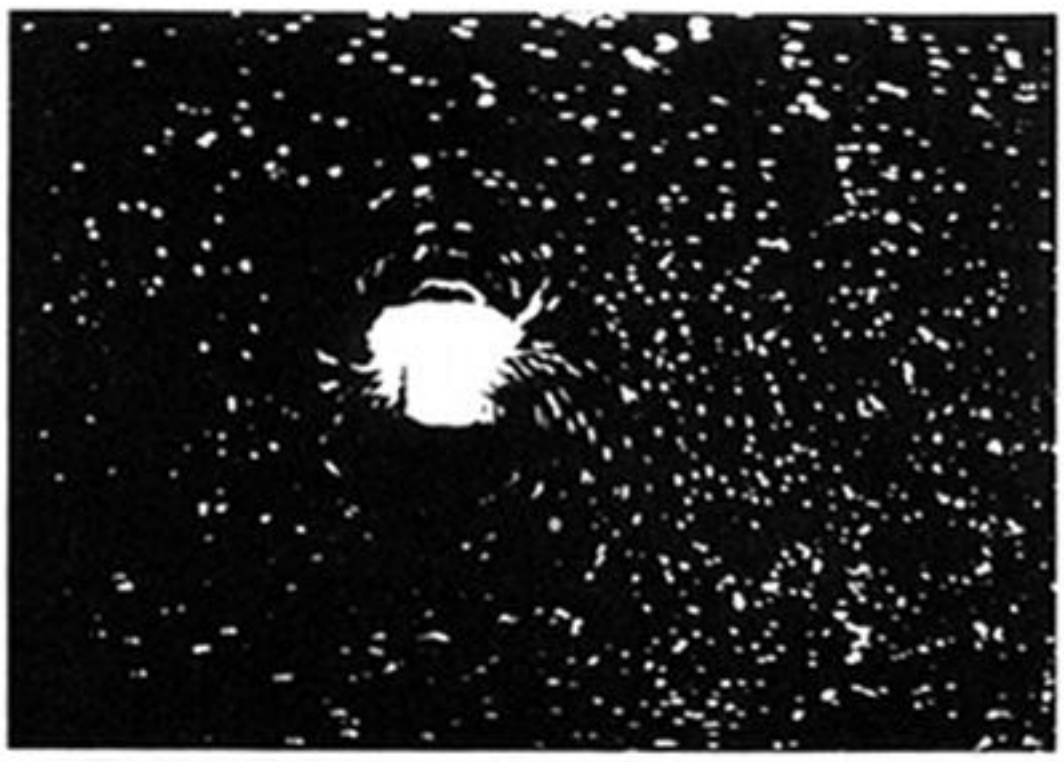

(ii)

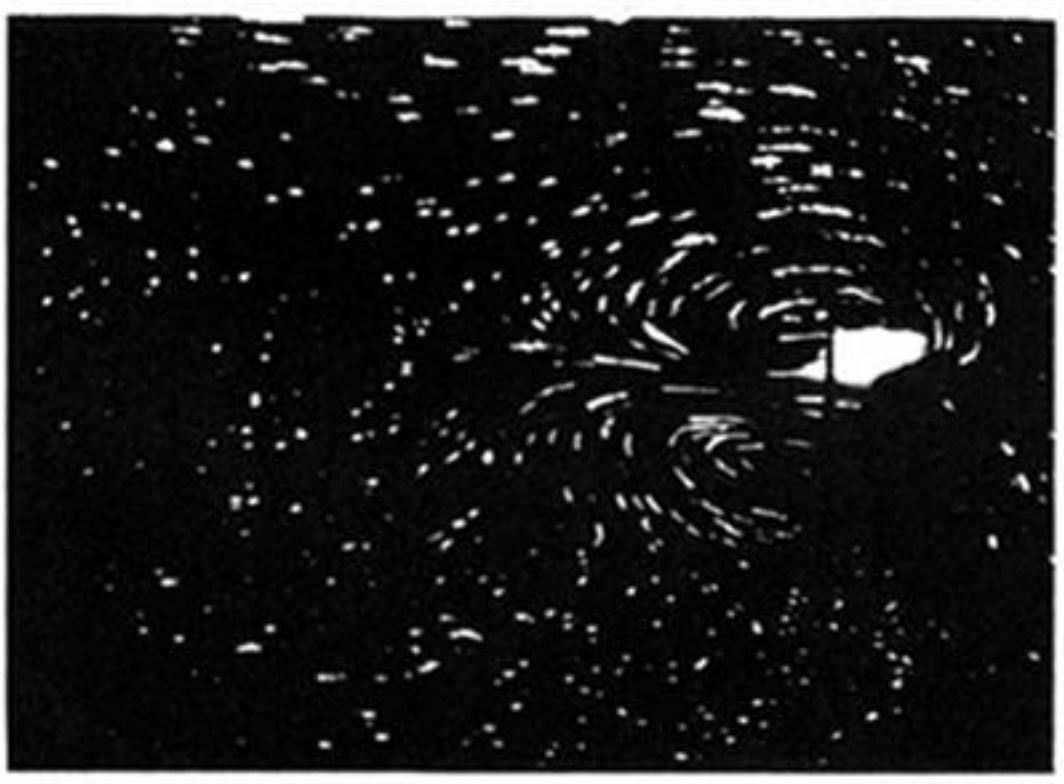

(iii)

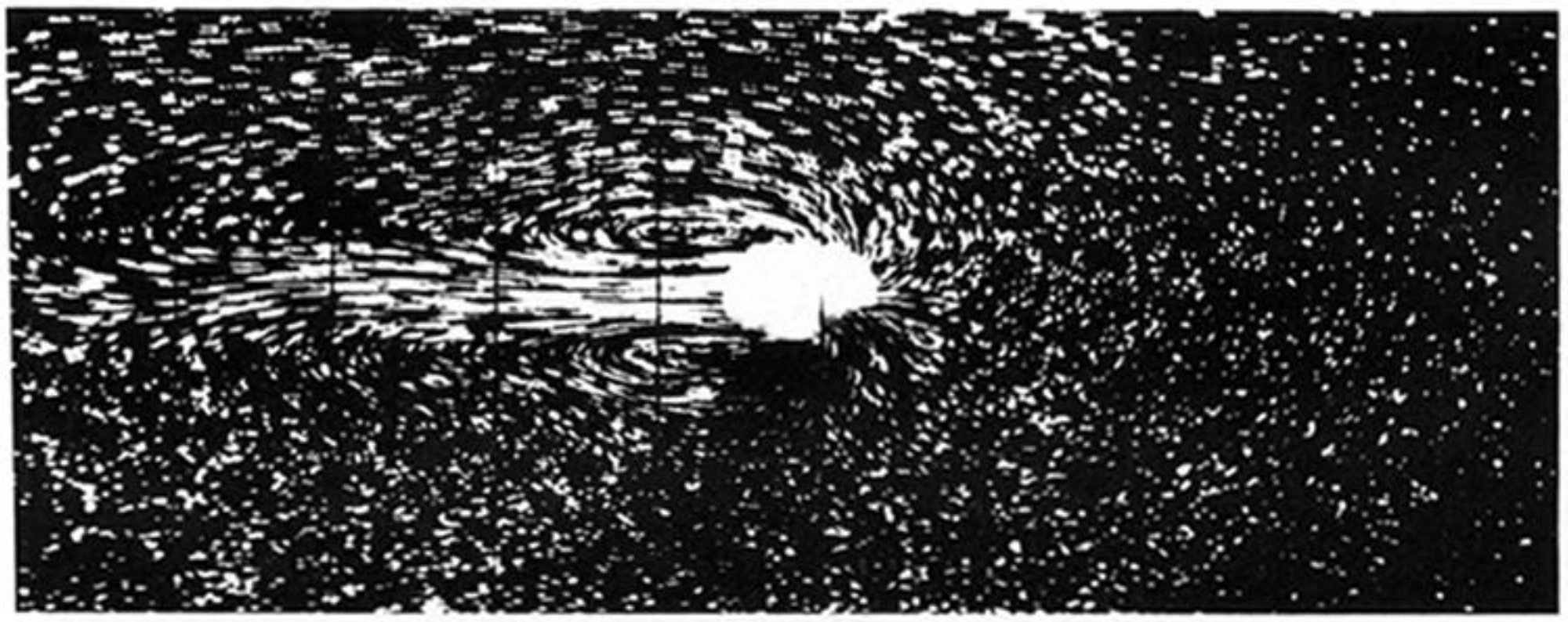

(iv)

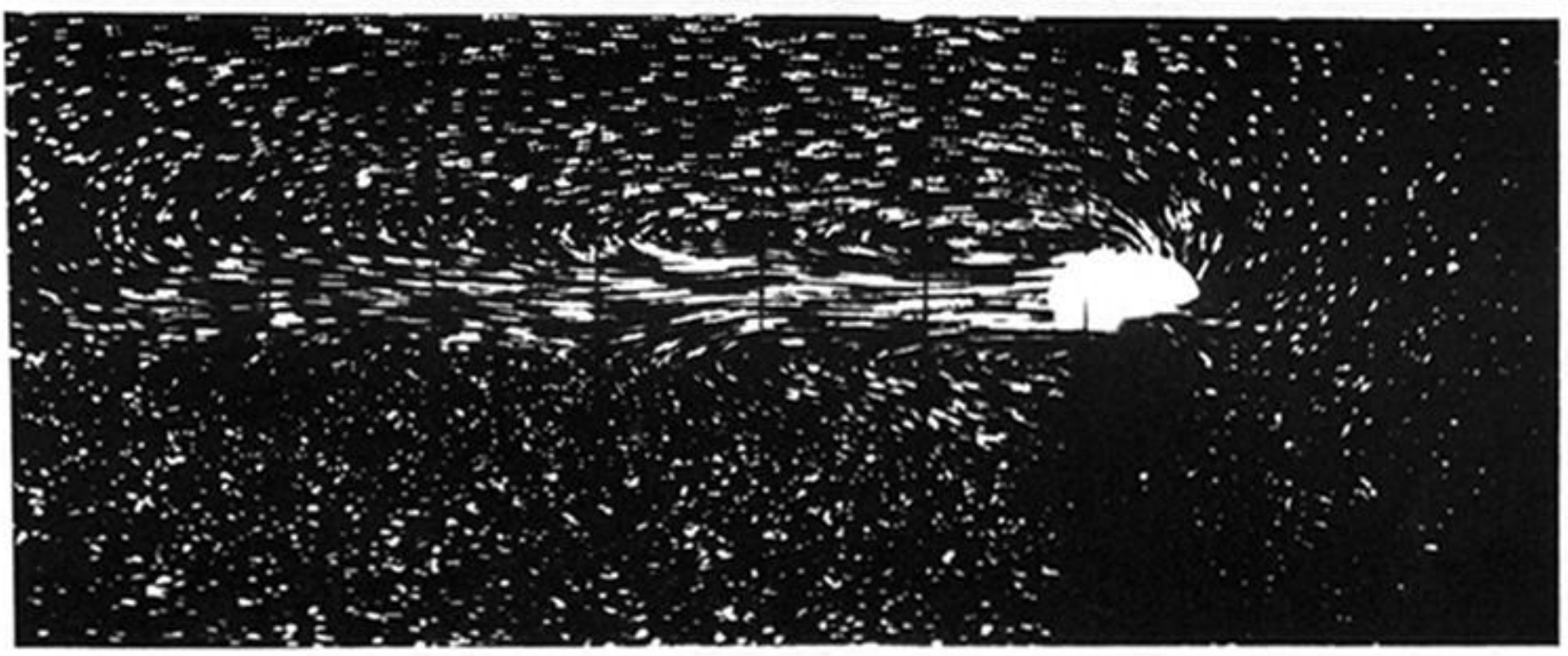

(v)

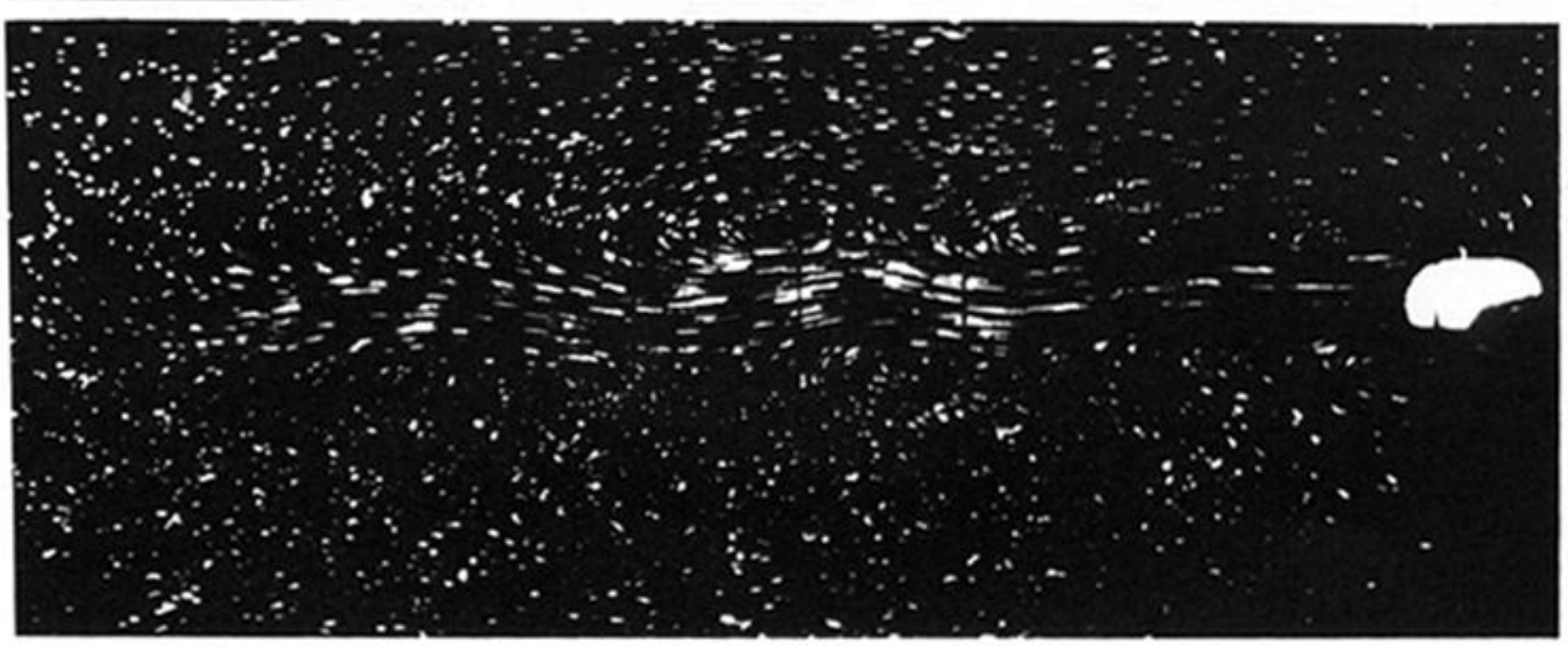

FIGURE 25*b*. For description see plate 9.

(c)

(i)

(ii)

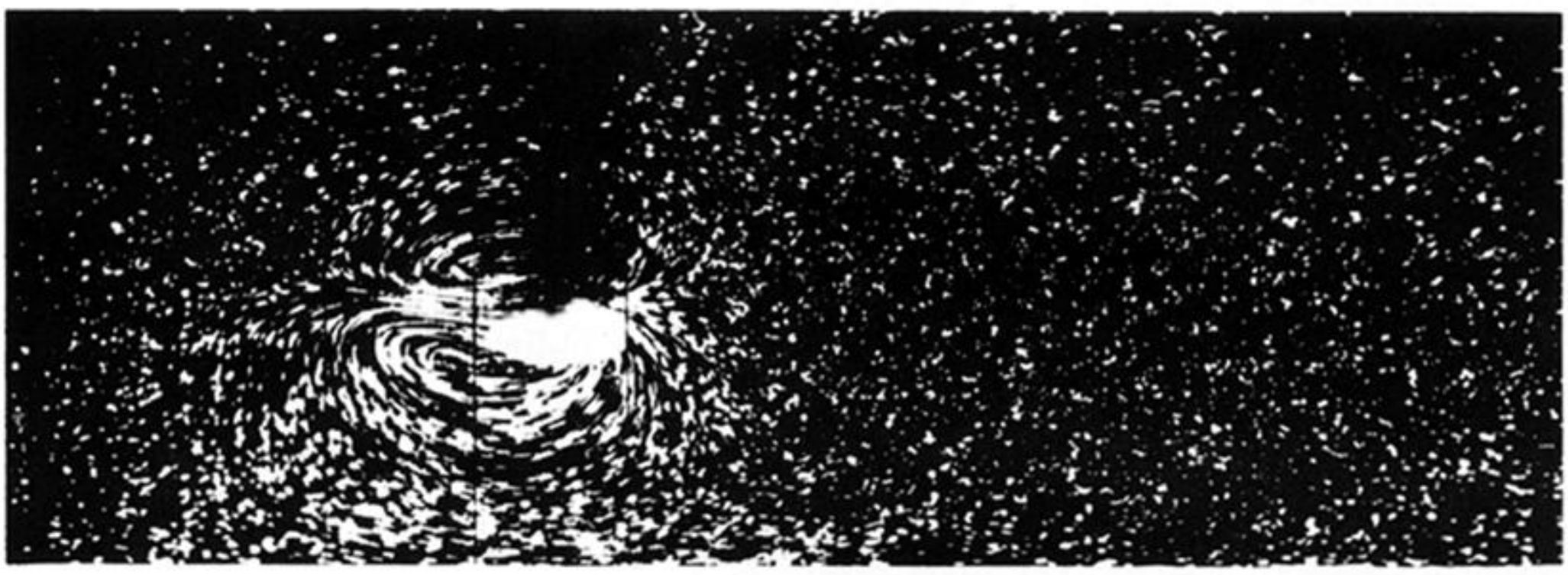

(iii)

(iv)

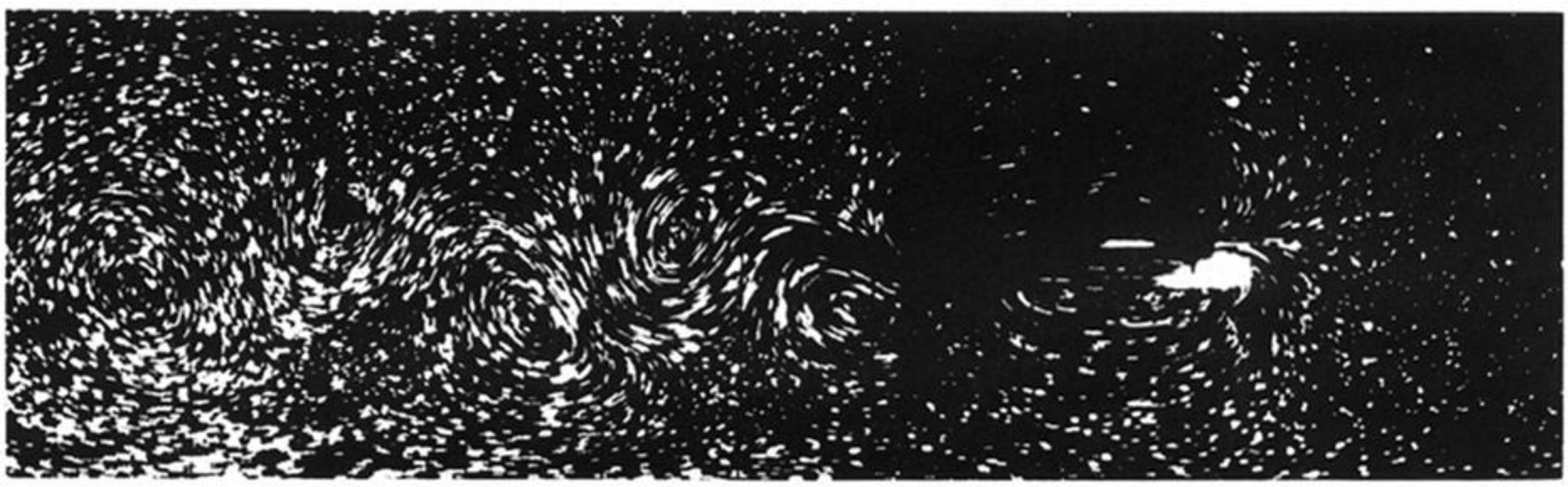

(v)

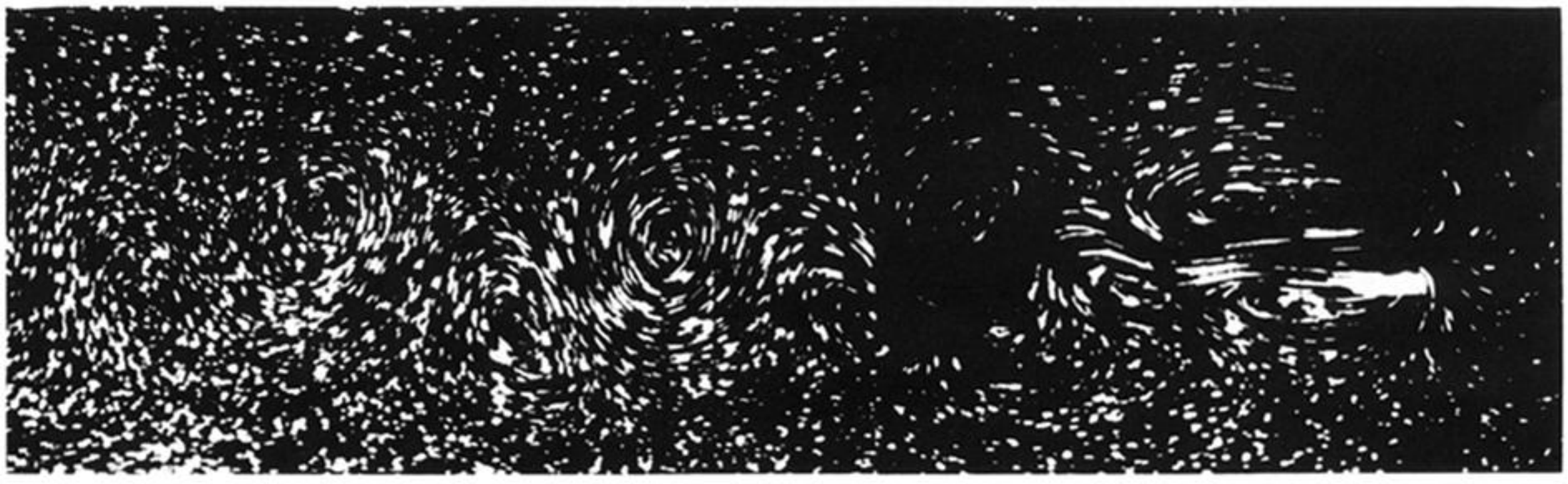

FIGURE 25*c*. For description see plate 9.

(*a*)

(i)

(ii)

(iii)

(iv)

(v)

(vi)

FIGURE 26. Plan photograph time sequences, in coupled frame, for $Bu = 17.6$, $Ro = 0.027$ and z^* is (*a*) 0.43, (*b*) 0.55. Values of t_A^* is (*a*) 0.63; 3.80; 6.90; 10.00; 13.10; 16.80, and (*b*) 0.67; 4.00; 7.30; 14.20; 17.53. Other parameters as for figure 25.

(*b*)

(i)

(ii)

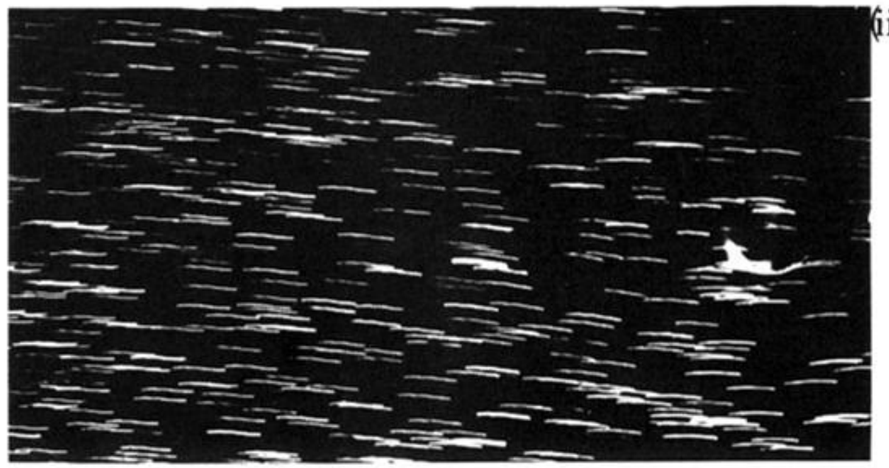

(iii)

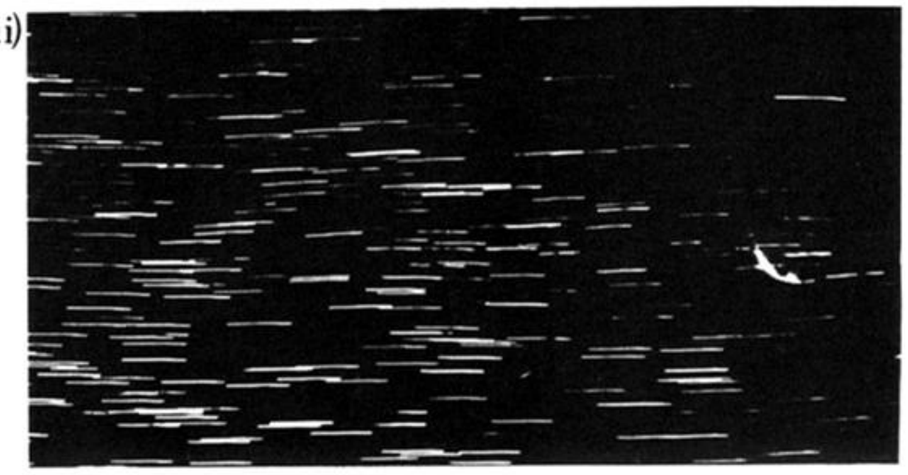

(iv)

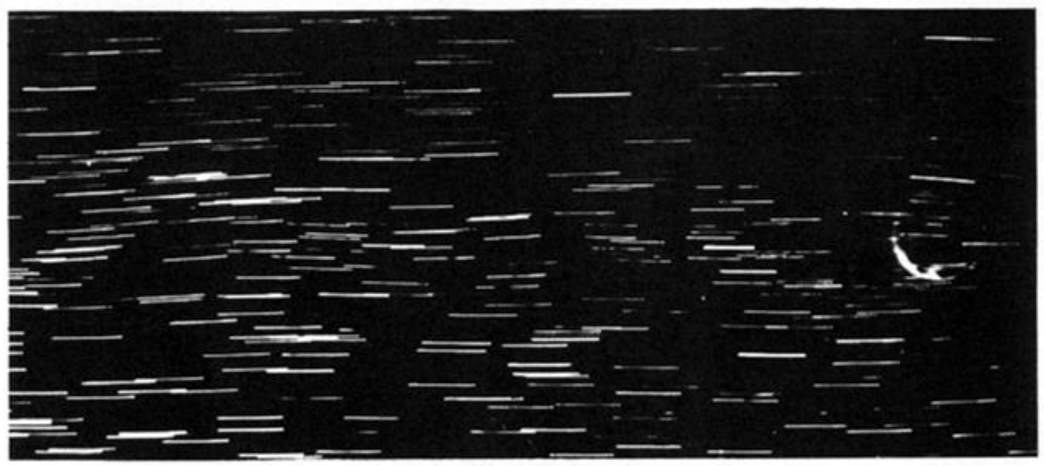

(v)

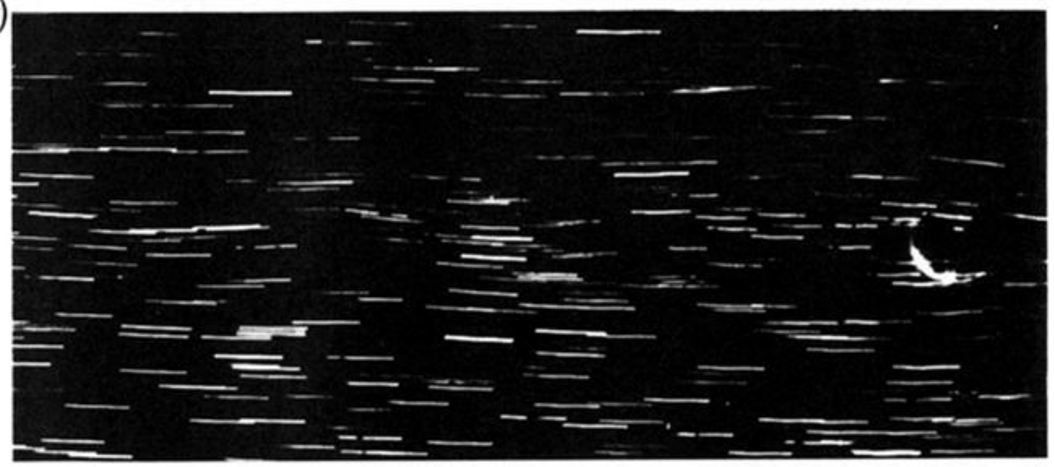

(vi)

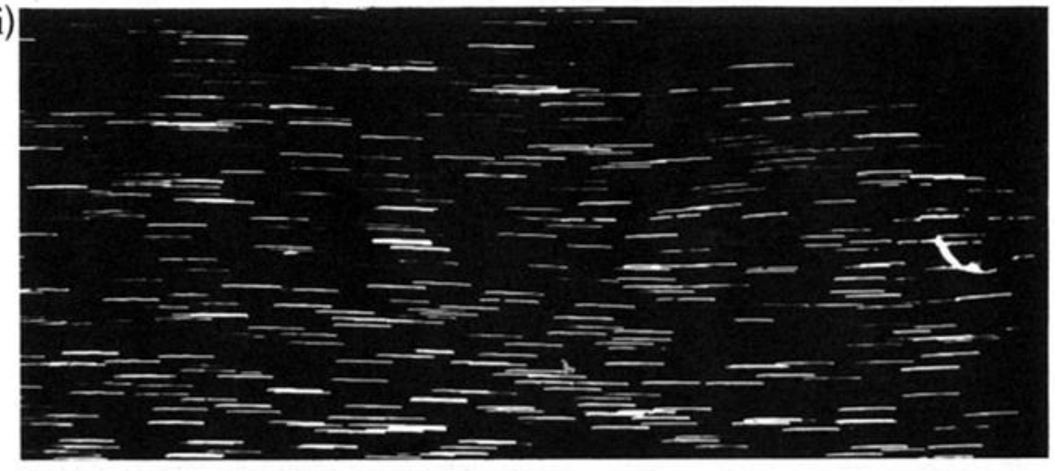

FIGURE 26*b*. For description see opposite.

(*a*)

(i)

(ii)

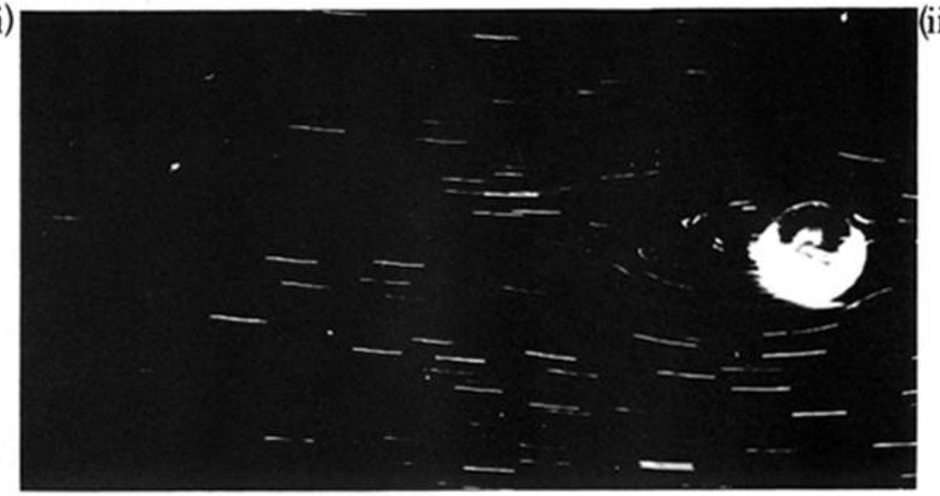

(iii)

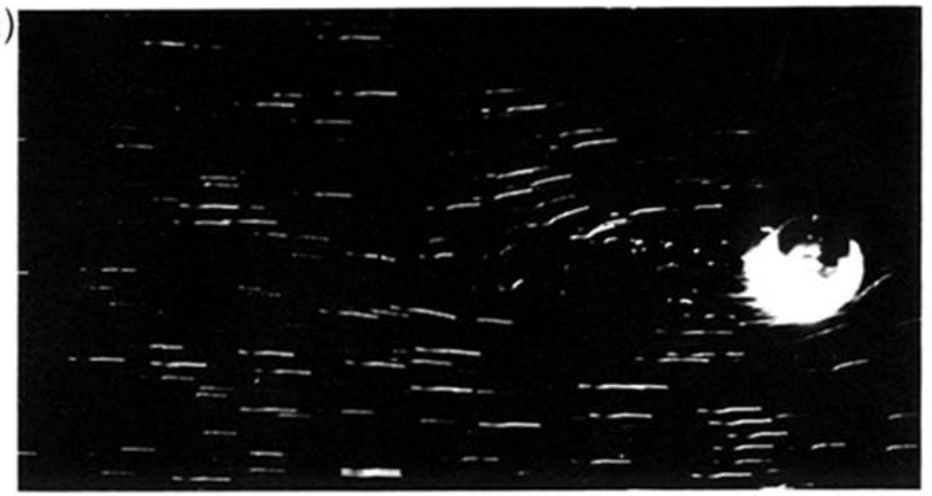

(iv)

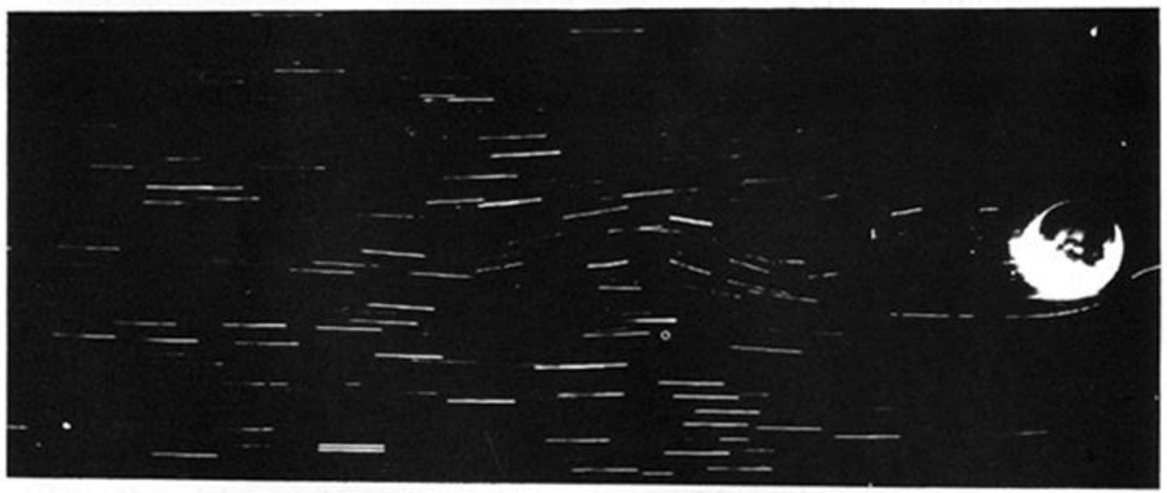

(v)

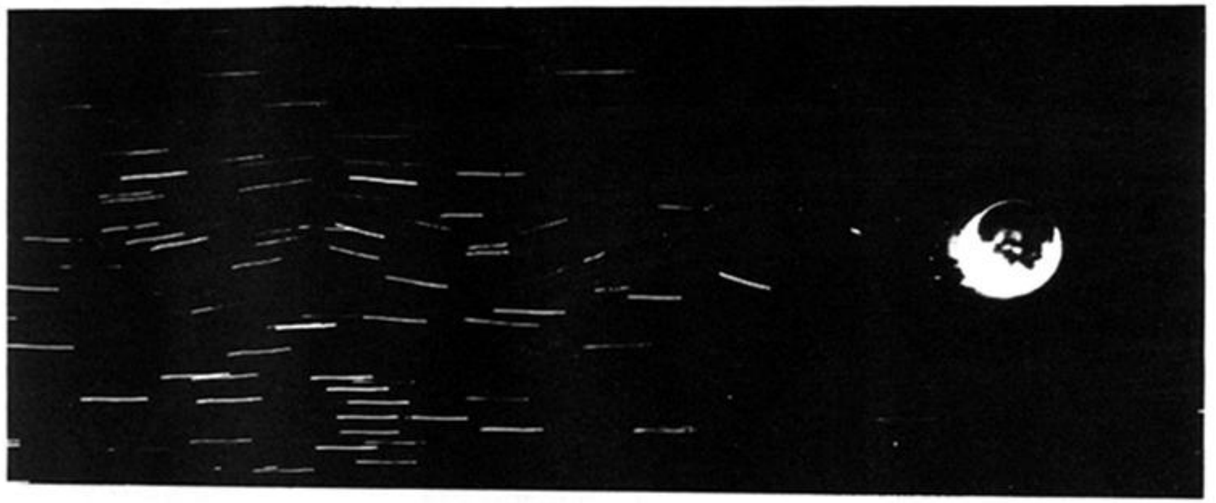

(vi)

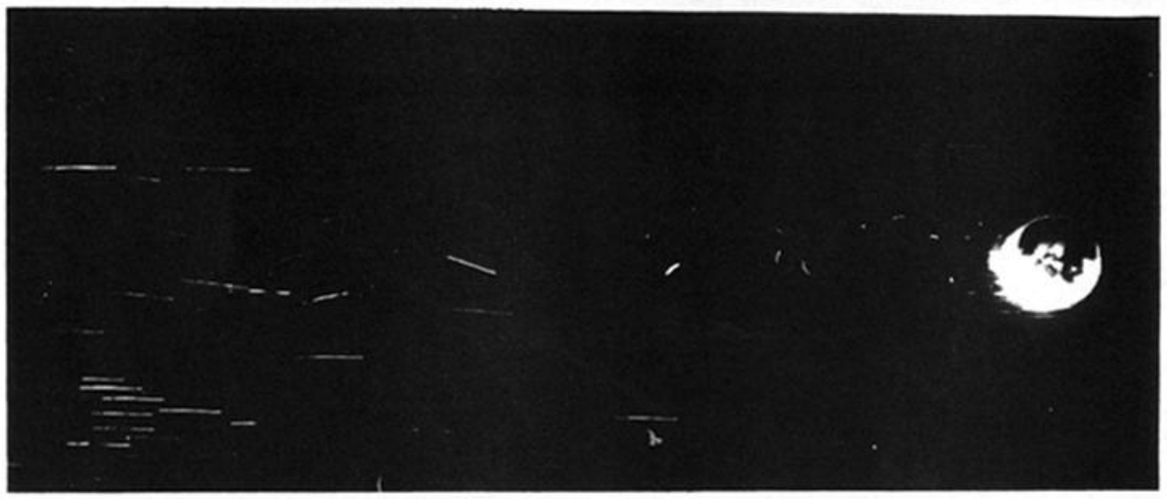

FIGURE 27. Legend as figure 26, except $t_A^* =$ (*a*) 0.80; 4.80; 8.80; 12.80; 16.60; 19.90, and (*b*) 0.88; 5.30; 9.60; 14.00; 18.60; 22.80.

(*b*)

(i)

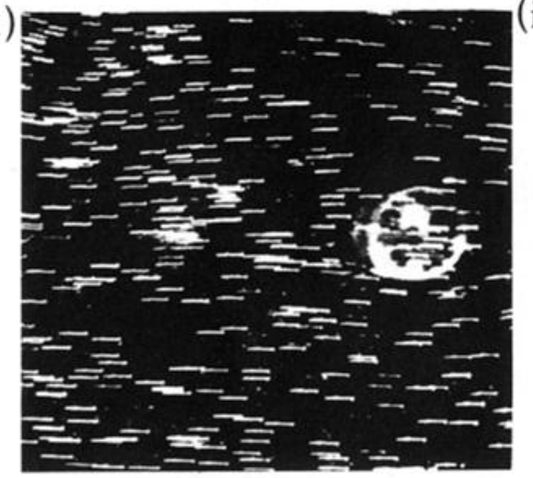

(ii)

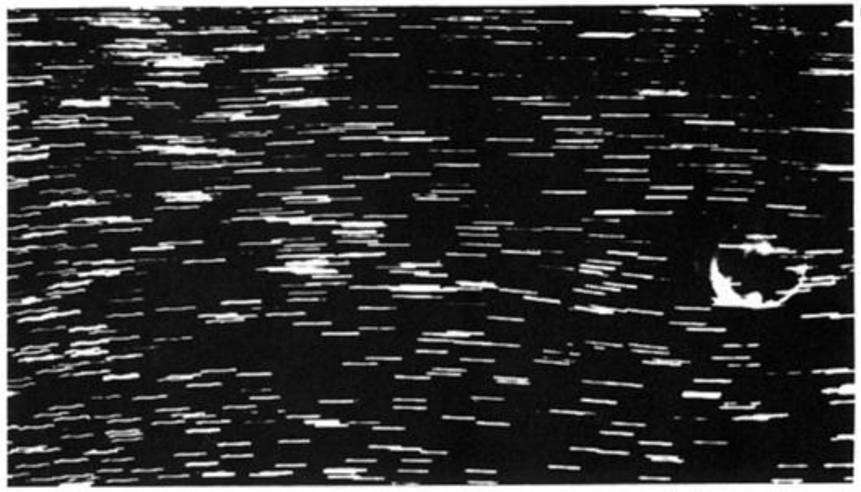

(iii)

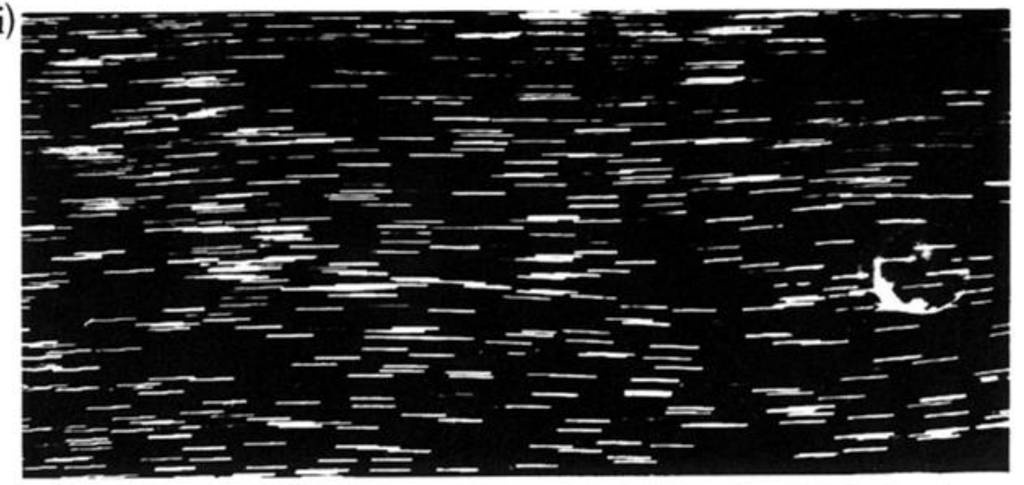

(iv)

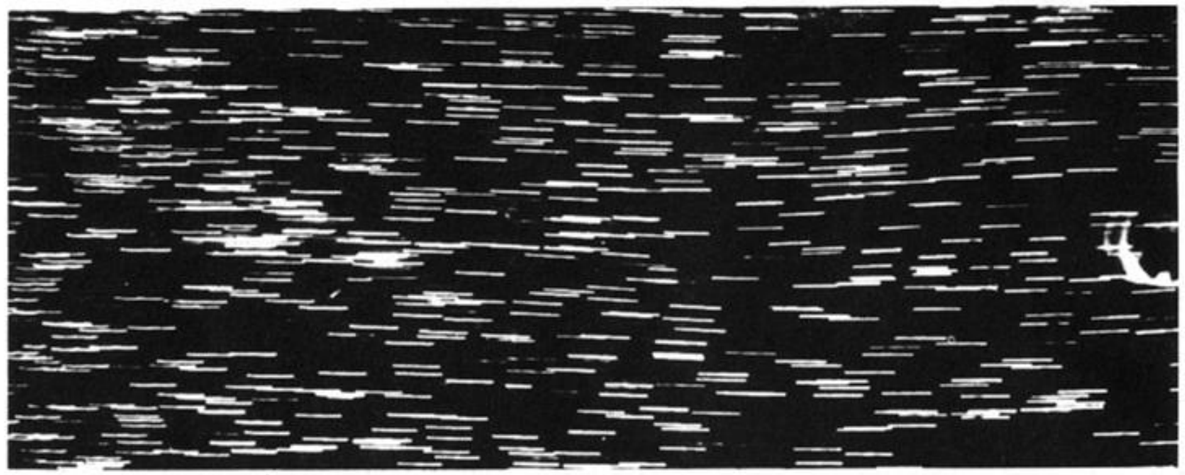

(v)

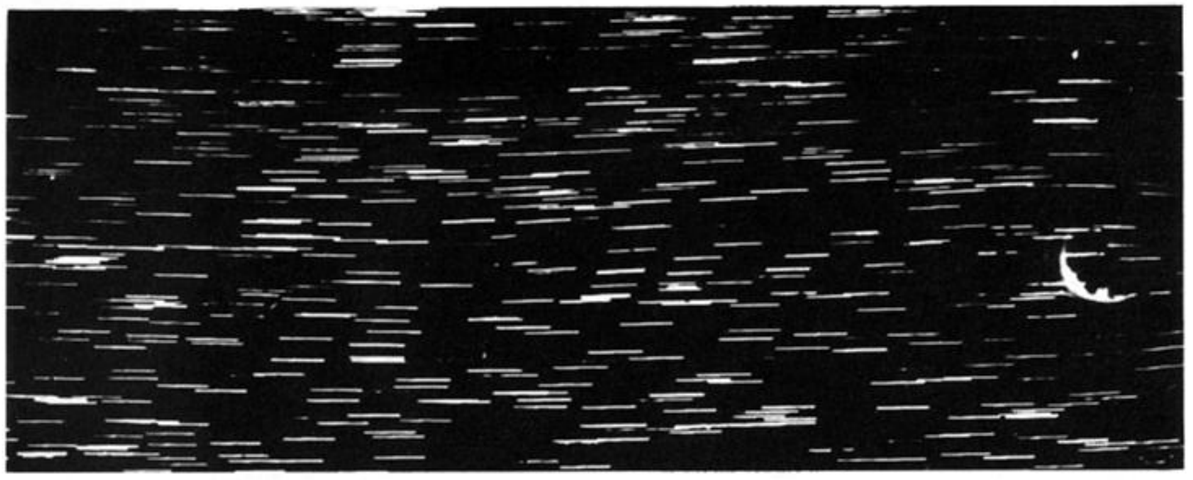

(vi)

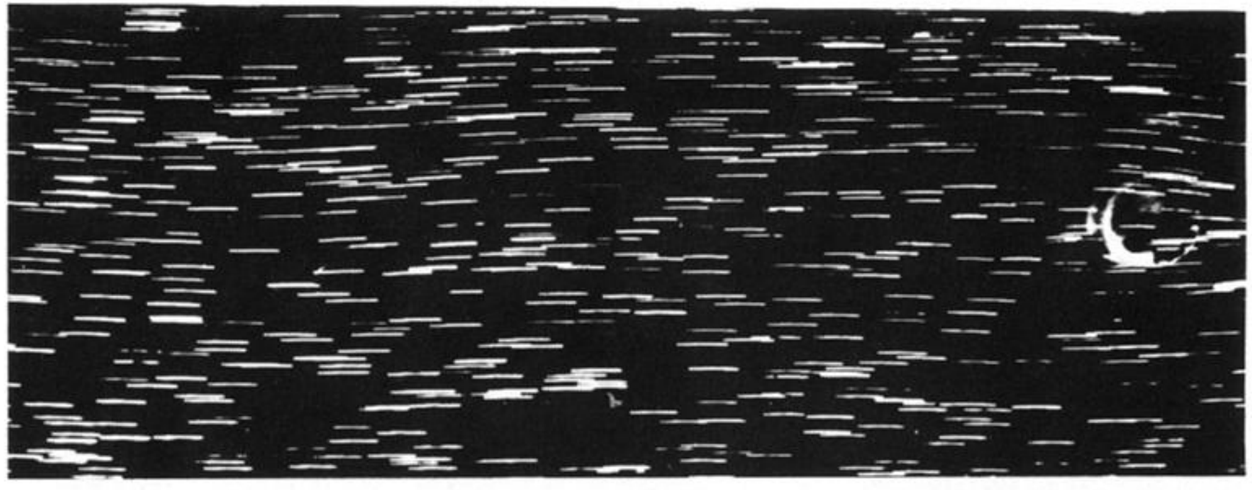

FIGURE 27*b*. For description see opposite.

(*a*)

(*b*)

(*c*)

FIGURE 29. Legend as figure 25, except $Bu = 6.90$, $Ro = 0.10$ and $\{t_A^*: z^*\}$ = (*a*) {18.60:0.45}, (*b*) {21.50:0.45}, and (*c*) {24.50:0.60}.

(*a*)

(*b*)

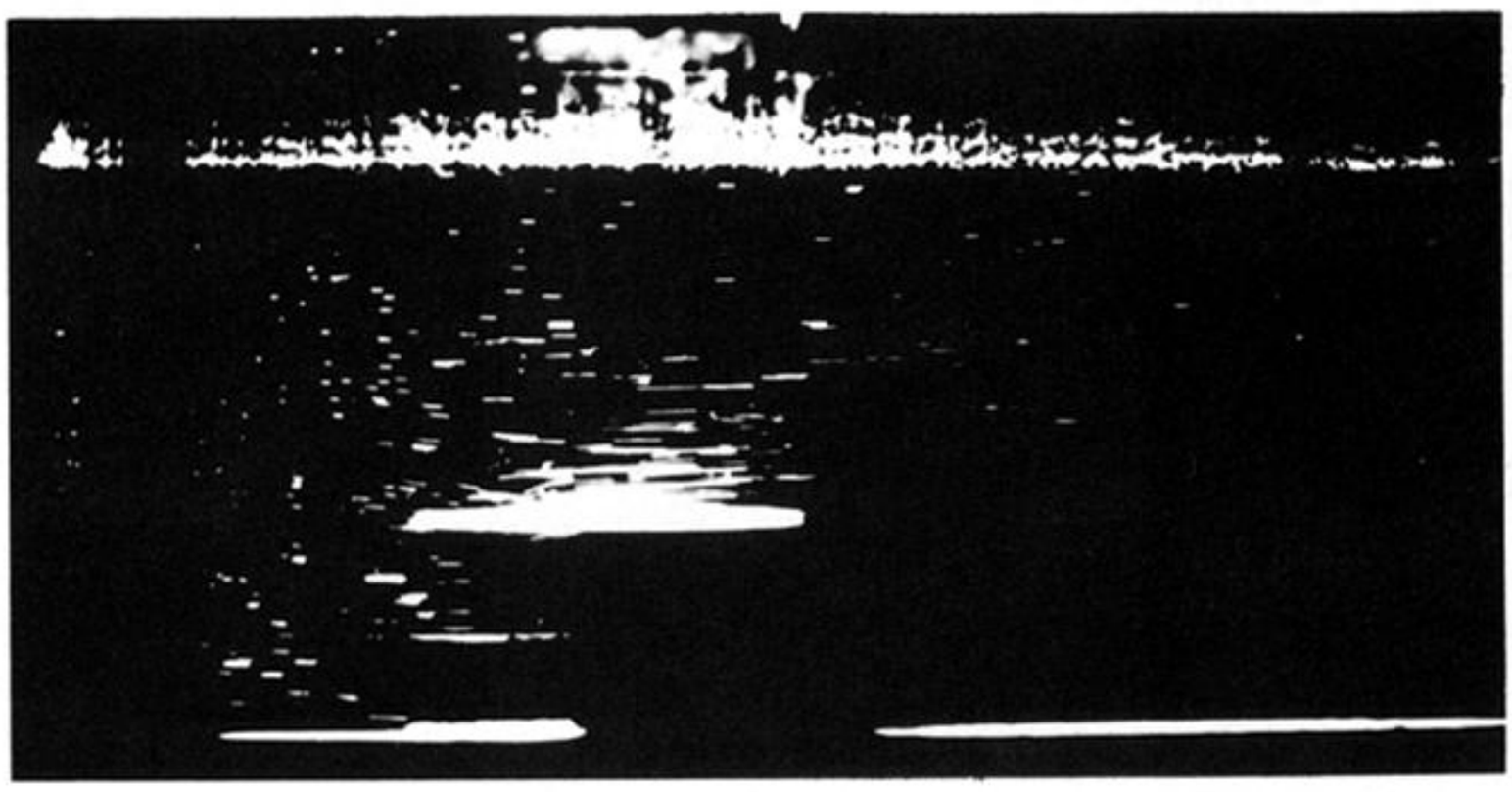

(*c*)

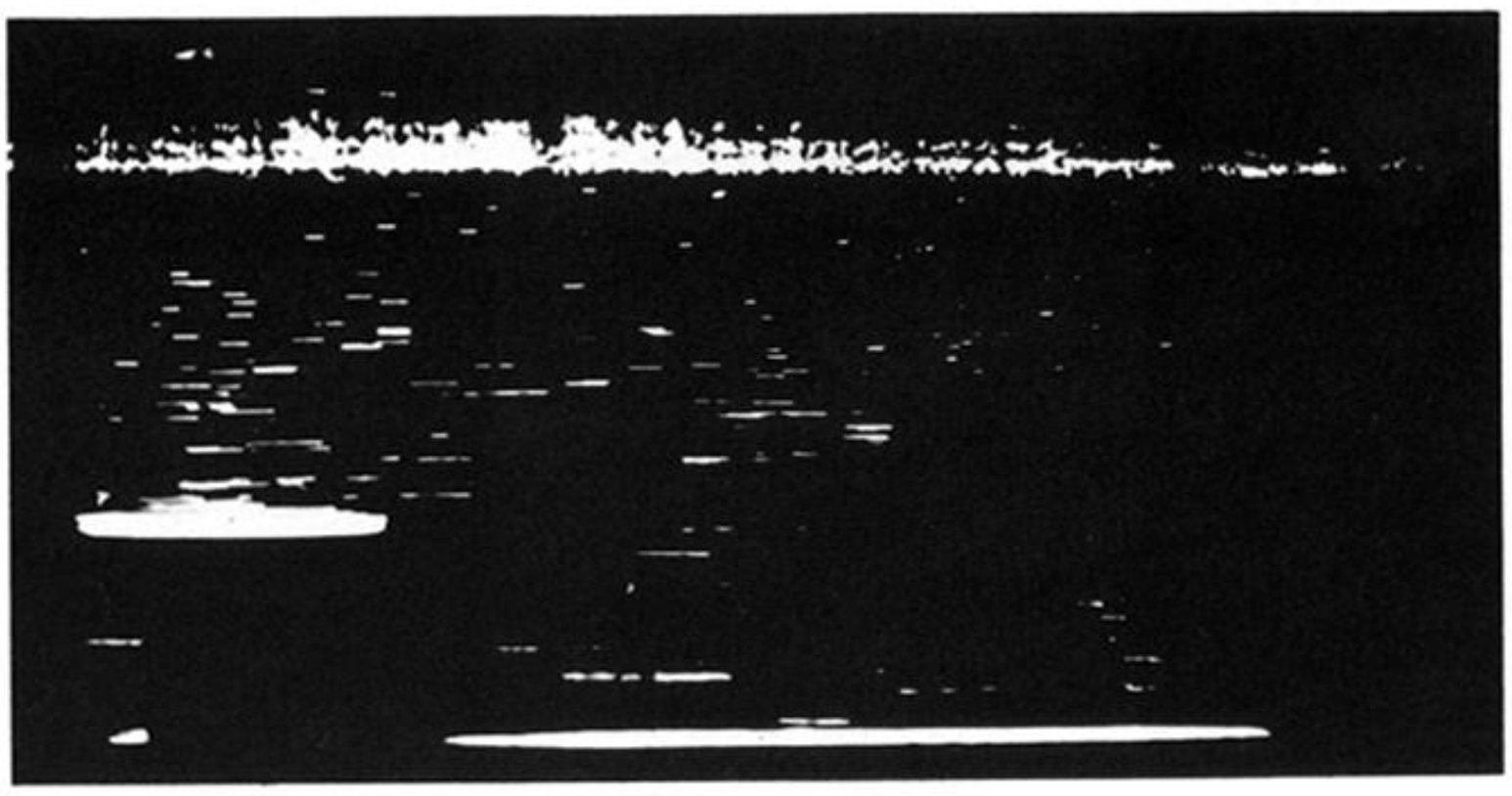

(*d*)

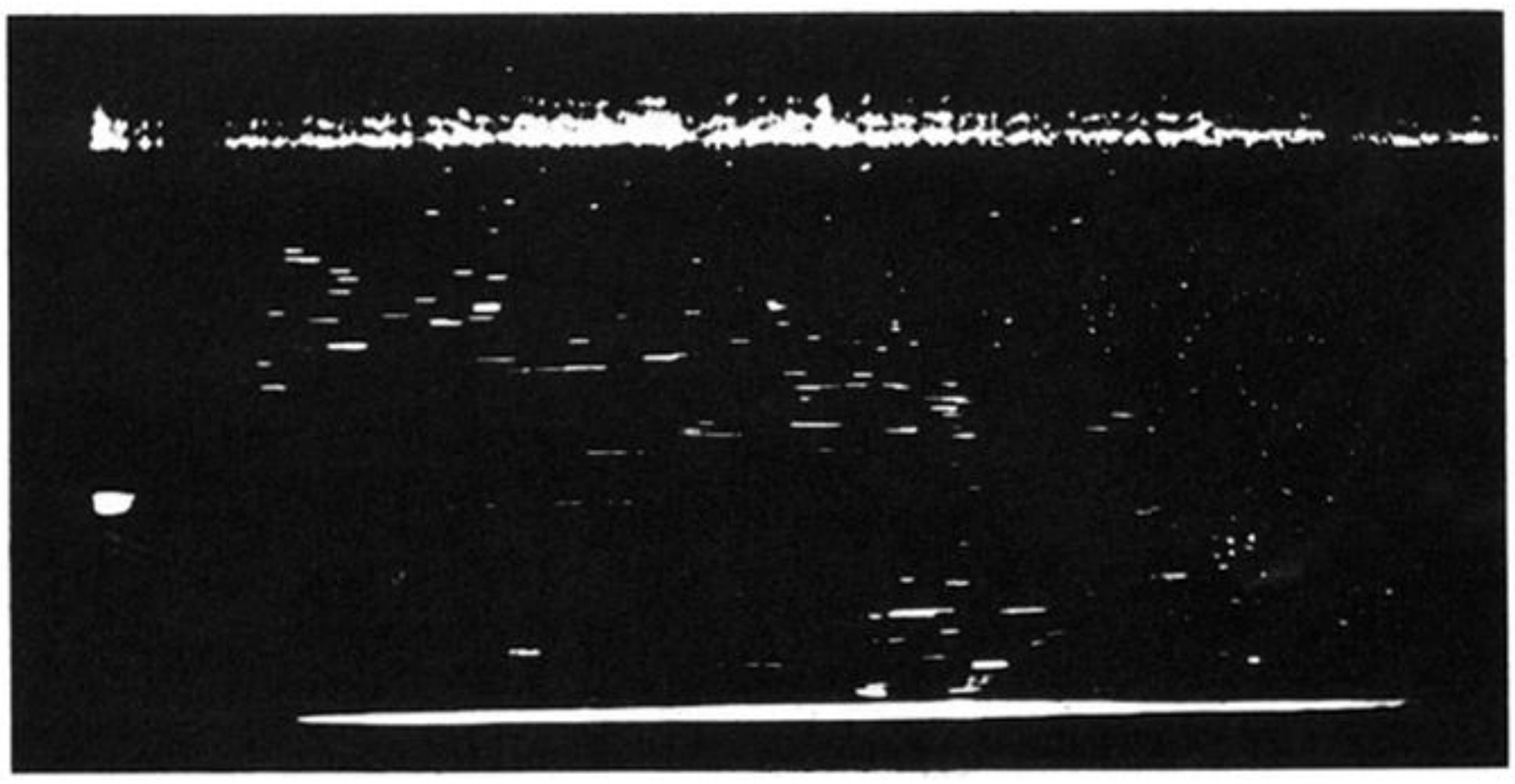

(*e*)

FIGURE 30. Elevation photograph time sequences for $Bu = 33.40$, $Ro = 0.076$, $h/H = 0.40$, $h/D = 1.00$, $E = 9.4 \times 10^{-5}$ and $t_A^* =$ (*a*) 13.20, (*b*) 14.10, (*c*) 14.90, (*d*) 15.80, and (*e*) = 16.60.

(*a*)

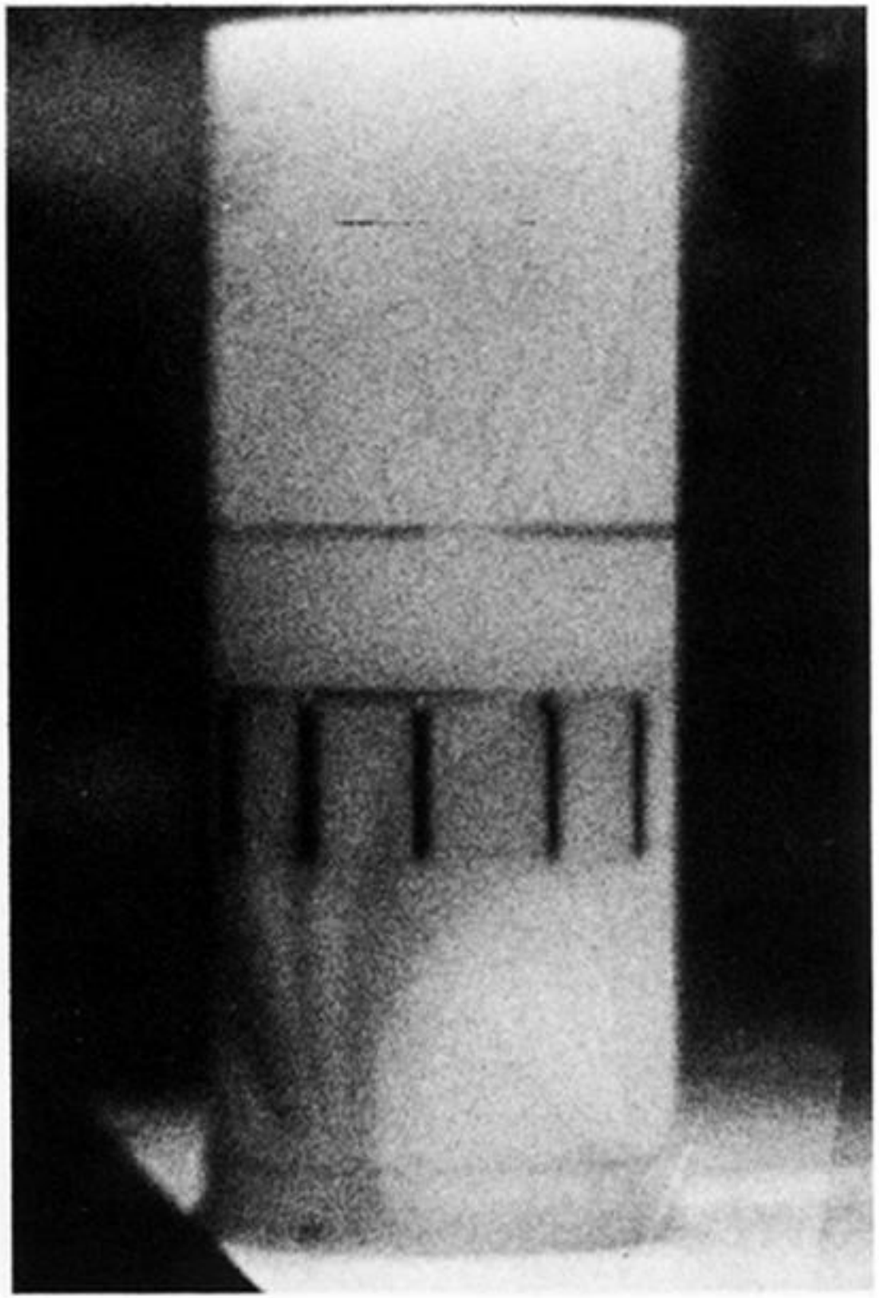

(*b*)

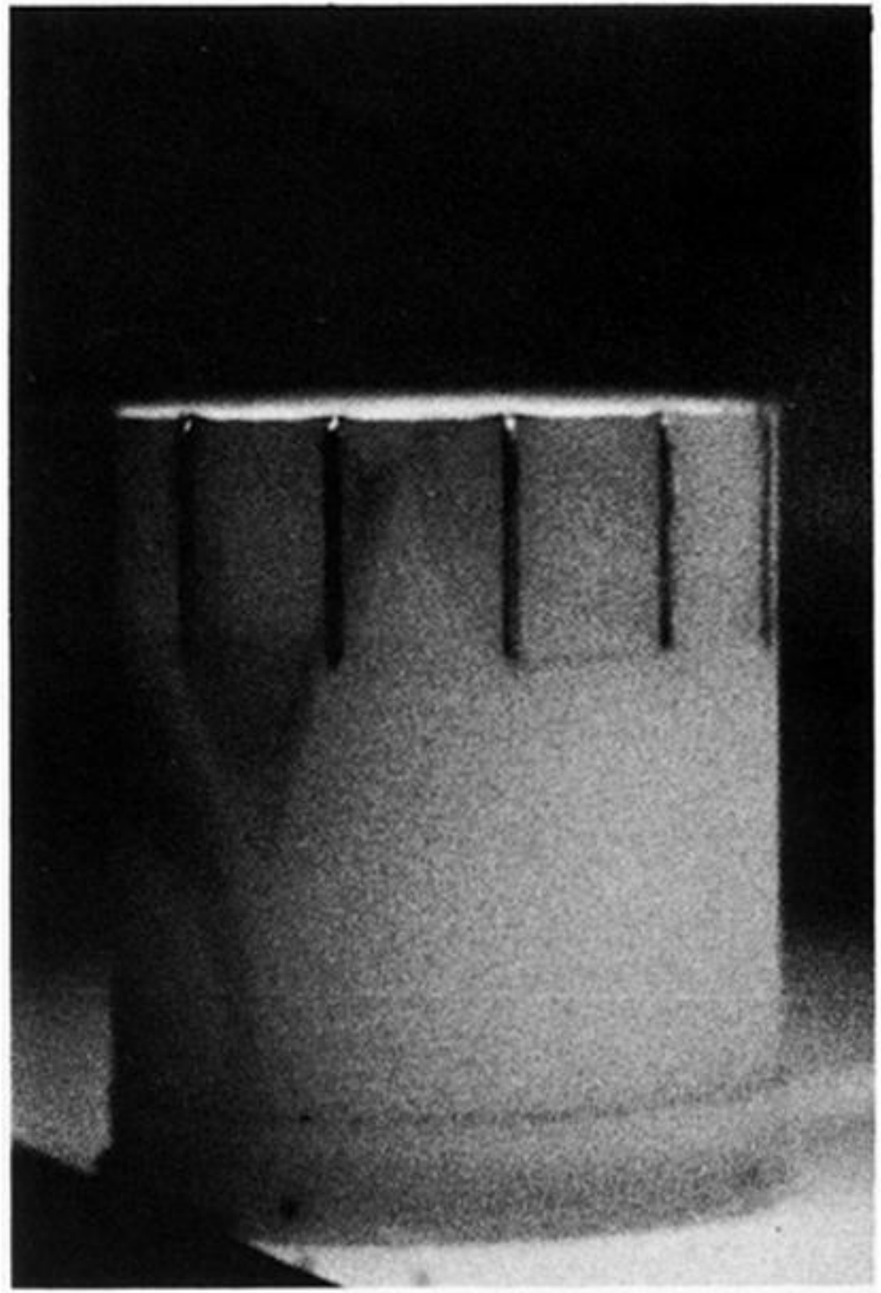

FIGURE 37. Oblique elevation dyeline photographs of shear layer patterns for $Bu = 0$, $Ro = 0.038$, $E = 9.4 \times 10^{-5}$ and $\{h/H : h/D ; t_A^*\} =$ (*a*) $\{1.00 : 2.50 : 6.10\}$, and (*b*) $\{0.40 : 1.00 : 10.20\}$. Motion of obstacle from left to right.